Università di Pisa
Facoltà di Scienze Matematiche, Fisiche e Naturali

Corso di Dottorato in Matematica

Tesi di dottorato

The Galilean satellites' dynamics and the estimation of the Jovian system's dissipation from JUICE data

Candidato:
Giacomo Lari

Relatore:
Prof. Andrea Milani

ANNO ACCADEMICO 2017-2018

To my parents

Cthulhu Macula in the southern hemisphere of Pluto.

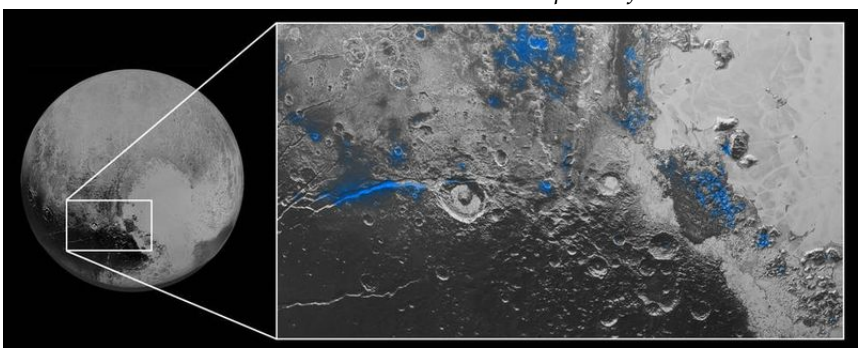

The most merciful thing in the world, I think, is the inability of the human mind to correlate all its contents. We live on a placid island of ignorance in the midst of black seas of infinity, and it was not meant that we should voyage far. The sciences, each straining in its own direction, have hitherto harmed us little; but some day the piecing together of dissociated knowledge will open up such terrifying vistas of reality, and of our frightful position therein, that we shall either go mad from the revelation or flee from the deadly light into the peace and safety of a new dark age.

H.P. Lovecraft, *The Call of Cthulhu*

ACKNOWLEDGEMENTS

I wish to acknowledge my advisor Andrea Milani for having me introduced to a topic that I found stimulating and fascinating. His suggestions and remarks have been an important guide for this thesis. I am very honoured to have been a student of Andrea, and his teachings will remain with me throughout my life.

I would like to thank the Celestial Mechanics Group of Pisa for their support and their friendship. Their work and their help have been very important for the developing of this thesis. In particular, the Daniele's efforts in the Juno mission have been an essential starting point for the orbit determination experiments performed in the second part of the thesis.

I would like to express my sincere gratitude to Valery Lainey and all the IMCCE for the period I spent Observatoire de Paris; I consider it a great educational experience for my research activity.

Amongst all the people that I met and collaborated with during my Ph.D, I cannot forget to thank Melaine. His method and ease with which he faces mathematical and physical problems are and will be a source of inspiration for my research. Nevertheless, his friendship has been a great support during these years.

Thank you to my colleagues and friends Francesco and Marco for all the time we spent together; without them my long days in the office would have been still longer.

I would like to thank Mattia de' Michieli Vitturi and the INGV for the opportunity to work on a field completely different from the celestial mechanics, but equivalently fascinating. This experience gave me new confidences on my research work.

During a period longer than three years, it is not possible not to consider the support of people outside the academic life. My family, my friends, my interests, thanks to all of them I reached this achievement. I will not make a list of people or experiences, but I cannot avoid mentioning my girlfriend Giulia. She has been my rock during the university and now during my Ph.D; her support has been the most valuable.

Finally, I wish to acknowledge two persons that probably will never read these few rows at the end of this page. They are two teachers of the secondary schools I attended in La Spezia when I was younger: Prof. Montanari of the Scuola Media Mazzini and Prof. Flandoli of the Liceo Scientifico Pacinotti; I consider their lessons essential for my mathematical formation. As the Ph.D is just the last part of a journey begun long time ago.

CONTENTS

INTRODUCTION

In 1610, the Italian astronomer Galileo Galilei observed with his telescope three small bodies near Jupiter. Initially, he thought they were stars, because of their brightness. But unlike the stars, they moved fast with respect to the planet's position. The following nights he discovered the presence of a fourth light on the same line of the others.

> *Il giorno sette gennaio, dunque, dell'anno meilleseicentodieci, a un'ora di notte, mentre col cannocchiale osservavo gli astri mi si presentò Giove; poichè mi ero preparato uno strumento eccellente, vidi (e ciò prima non mi era accaduto per la debolezza dell'altro strumento) che intorno gli stavano tre stelle piccole ma luminose; e quantunque le credessi del numero delle fisse, mi destarono una certa meraviglia, poiché apparivano disposte esattamente secondo una linea retta e parallela all'eclittica, e più splendenti delle altre di grandezza uguale a loro.*
>
> Galilei, Sidereus Nuncius (1610)

In [12], Galilei announced the discovery of four satellites of Jupiter, which in his honour would have been named Galilean (actually Galilei named them Medicean stars, in honour of Cosimo II de Medici of Florence). This was an extraordinary fact for the time, as it showed that there were bodies that did not orbit around the Earth, in the long dispute between geocentric and heliocentric theories.

Instead, the single names of the satellites are due to a German astronomer, Simon Marius, that claimed to be the first to have observed the moons. Their names were taken from the Greek mythology, in particular from some lovers of the god Jupiter: Io, Europa, Ganymede and Callisto (in order from the planet).

For the whole 17th century the Galilean satellites were observed with the new telescopes at the time, allowing to produce first ephemerides tables of the moons and to study their eclipses with Jupiter. In particular, the last ones were very important for first computations of the longitude on Earth and of the speed of light. In 1798, Laplace proved in [26] that the three inner moons were locked in a mean motion resonance with ratio $4 : 2 : 1$, today known as Laplace resonance.

> *[...] on aura donc, en n'ayant égard qu'aux quantités moyennes,* $n_1 - 3n_2 + 2n_3 = 0$*; c'est-à-dire, que le moyen mouvement du premier satellite, moins trois fois celui du second, plus deux fois celui du troisième, est exactement et constamment égal à zéro.*
>
> Laplace, Traité de Mécanique Céleste, Livre II (1798)

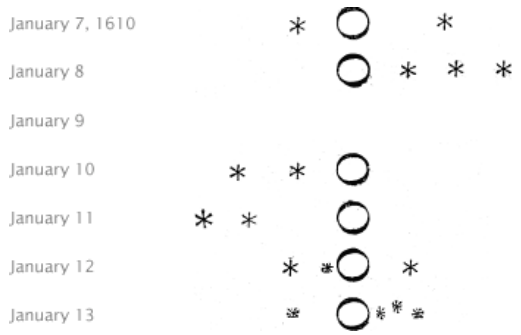

Drawings of Galileo Galilei, taken from the Sidereus Nuncius. They represent Jupiter and the Galilean satellites as seen by the astronomer in six different nights. In his book, he reported the positions of the moons from the day of their discovery, January 7, to March 2, and only from January 13 Callisto was observed.

This commensurability means that the orbital period of Ganymede around Jupiter is (almost) two times the one of Europa and (almost) four times the one of Io. Mean motion resonances are not uncommon for asteroids and satellites, but most of the times they involve two bodies only. The Galilean satellites were the first known case in the Solar System of a three-body resonance, although recently it was discovered a similar resonance between the satellites of Pluto, as reported in [43].

From that year, a wide number of scientists have studied the system composed by Jupiter and the Galilean satellites. One of the first important contribution for the understanding of their dynamics, is due to de Sitter. In [6], the author developed a new analytical model of the satellites' motion, investigating the existence of periodic orbits. This special case is called de Sitter resonance, which is not exactly the same configuration of the current Laplace resonance.

In 1979, Peale, an American scientist, and its collaborators predicted the presence of volcanoes on the surface of Io, computing for the first time the large energy dissipation due to the tides that Jupiter raises on the little moon. For the same reason, an year later, in [4] it was supposed the existence of an ocean under the icy crust of Europa. Peale managed to publish his results in [38], some days before the images of the Voyager space mission that confirmed his theory: the camera captured the ejected gas plumes that rose over Io's surface. The paper was published in Science of March 2, while the photo reported in this section was taken on March 8.

From this discovery, it was clear that there was a force that could make the resonance evolve. Apart from being the source of the Io's volcanism, the huge tidal friction dissipates the orbital energy of the moon, modifying its semi-major axis. Moreover, because of the resonant interaction, also the orbits of Europa and Ganymede change.

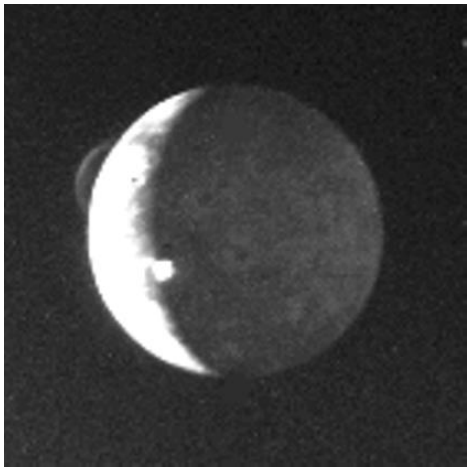

Picture taken by Voyager 1 in 1979. The plume captured by the spacecraft's camera was the first evidence of Io's volcanic activity.

From 1995 to 2003, Galileo space mission performed some very close flybys of the satellites. For the first time it was possible to obtain tracking data for a better understanding of the moons' structure. Unfortunately, the main antenna mounted on the spacecraft had a problem in the opening, then it was necessary to use the low-gain antenna, losing quality in the tracking.

Meanwhile, for all the 20th century, the Galilean satellites were observed from telescopes all over the world, providing data useful to comprehend their motion.

The generation of new ephemerides with improved accuracy is a challenge for the main teams that provide this kind of tables. In particular, it means to handle a big amount of data, almost from the end of the 19th century to the present day. The kind and the precision of the observations can be very different: they pass from astrometry to spacecraft tracking data and from accuracies of hundreds of kilometers to few meters. Moreover, the forces acting on the system are several and, because of the large time span, they must be taken all into account.

Up to now, the several solutions of the Galilean satellites motion disagree about the amount of dissipation. We reported a table taken from [24] with the values of the variation in the satellites' mean motions due to the tidal dissipation, as calculated in various articles. The results differ both for the orders of magnitude and for the signs; this means that there is discrepancy both about the amount of the dissipative effects and the resultant effect. In fact, the sign of the mean motions' variation indicates if the satellites are accelerating or decelerating, or equivalently, if they are moving toward Jupiter or outward.

In particular, the values of the dissipative parameters obtained by the IMCCE (Institut de Mécanique Céleste et de Calcul des Éphémérides) in [24] and by the JPL (Jet Propulsion Laboratory) in [16] differ for almost three orders of magni-

Author	Year	$\dot{n}_1/n_1$	$\dot{n}_2/n_2$	$\dot{n}_3/n_3$
De Sitter	1928	3.3	2.7	1.5
Lieske	1987	-0.074	-0.082	-0.098
Goldstein *et al.*	1995	4.54	5.6	2.8
Vaundhara *et al.*	1996	2.27	-0.67	1.06
Asknes *et al.*	2001	3.6	—	—
Lainey *et al.*	2009	0.14	-0.43	-1.57

Dissipative effects, presented as variation in mean motions over mean motions (units 10^{-10} rad/y), as obtained from different articles. Table taken from [24]; references in the paper.

tude. Therefore, while for the first the effect of the dissipation over 100 years is a shift along the orbits of tens or hundreds of kilometers, for the second it is just hundreds of meters. And more, also the tidal friction that disrupts the interior of Io would be strongly downsized. It is very surprising that at the current level of knowledge of celestial mechanics' sciences, it is possible this huge disagreement between two of the main teams of satellites' ephemerides. Actually, this could be due to the different choices of which data to include into the fit; considering Galileo mission's data, as done in [16], or not, as in [24], could have brought to completely different results.

The future JUICE space mission is a great opportunity to solve this dispute. JUICE is an ESA (European Space Agency) mission that will be inserted in the Jovian system at the beginning of 2030 and that will perform several flybys of the Galilean satellites. Moreover, in the last part of the mission, it will orbit around Ganymede for nine months, with a possible extension of the mission. The data that JUICE will collect during its tour will have an extraordinary precision, allowing to investigate several aspects of the system. Amongst them, the energy dissipation and the Laplace resonance should have a crucial role in the scientific program of the mission.

The Galilean satellites' dynamics is a very fascinating topic. It comprehends resonances and large dissipative effects and these two aspects are strongly correlated as we will see. Besides, they are a small copy of the Solar System: obtaining information about them, it could be possible to comprehend better the whole system. Moreover, the evolution of the resonance and the dissipative forces can give some clues of their origin and the history of other satellites systems (e.g. Saturn) and exoplanets.

The aim of this thesis is to study the dynamics of the Galilean satellites and to investigate the contribution of the JUICE space mission data to the improvement of Galilean satellites' ephemerides and to the knowledge of the dissipation in the system.

The thesis is structured as follows: in the first part, we will present a semi-analytical model of the Galilean satellites' dynamics. We will study the resonant and secular motion through a Hamiltonian containing the main perturbations of the system and depending on the slow angles only. We will show, by a comparison with numerical models, that the model describes well the actual motion of the moons and also the migration of their orbits due to the tidal dissipation.

In the second part, we will describe the JUICE mission and the orbit determination experiments we performed in order to estimate the energy dissipation. We will introduce ORBIT14, an orbit determination software developed by the Celestial Mechanics Group of Pisa, and we will illustrate the numerical models implemented for the bodies' propagation and for the prediction of the observations. For a realistic estimation, we will consider a great number of parameters and dynamical effects, although we will focus our analysis mainly on the tidal dissipation.

Part I

A SEMI-ANALYTICAL MODEL OF THE GALILEAN SATELLITES DYNAMICS

1 THE GALILEAN SATELLITES

The Jovian system has very particular and fascinating characteristics. Jupiter is distant almost 5.2 au (astronomical unit) from the Sun and it is the major planet of the Solar System. It is a gas giant, it means that it is composed mainly by gaseous matter, in particular hydrogen and helium. As witnessed by the numerous pictures and by the new photos of the Juno mission currently orbiting around the planet, Jupiter is completely covered by clouds and storms. Since we are mostly interested in the Galilean satellites, we give a brief description of these bodies, while we avoid presenting minor moons.

The Galilean satellites are the Jupiter's biggest moons: Io (1), Europa (2), Ganymede (3) and Callisto (4). In the next chapters we will focus on their dynamics, but first we want to present their main physical properties. More details can be found in [44].

- **Io**. It is the closest to Jupiter. Unlike the other Galilean satellites, it has a dry surface, with no evidence of water. Because of its proximity to the gas giant, the dissipative effects due to the tides have a huge impact on its structure. In fact, the tidal forces of Jupiter are the source of volcanism on the satellite. In 1979, Voyager spacecraft observed plumes arising from its volcanoes, but volcanism on Io comprehends also liquid lava flows and pyroclastic eruptions. Pictures and infrared observations showed how much strong the volcanic activity is, leading to an heat flux near to 2 $Watt/m^2$ (for the Earth is almost 0.1). Moreover, the escape and ionization of the atoms form a plasma torus in the space around Jupiter.

- **Europa**. It is the first of the icy moons and the smallest of the Galilean satellites. It has an icy crust that covers the surface, and below it is supposed to lie an ocean of water. Its existence would be due to the tidal dissipation, the same cause of Io's volcanism, that allowed to heat the water near the surface for millions of years. There are also some evidences of cryovolcanism. Along the surface the splits of the icy terrain are evident; they could be the result of the displacement of the tidal bulges.

- **Ganymede**. It is the largest satellite in the Solar System. Its grooved surface indicates a very active geological past, with some evidences of cryovolcan-

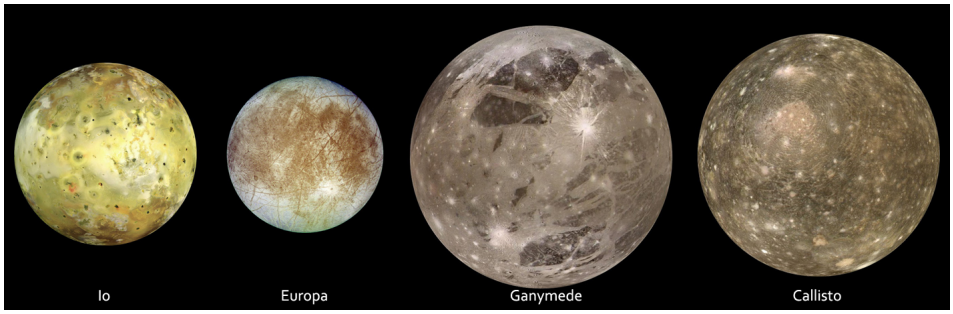

Figure 1.1.: *The four Galilean satellites: Io, Europa, Ganymede and Callisto.*

ism. Ganymede has an intrinsic magnetic field that generates a small magnetosphere inside the larger Jupiter's magnetosphere. It has also a tenuous atmosphere, mainly composed by oxygen and ozone. The presence of oxygen could be due to the sublimation of ice on the surface or to some gas bubbles trapped under the ice.

- **Callisto**. It is the furthest moon and the less active geologically. In fact, craters and asteroids crashes are clear on its surface; this leads to think that the surface has not changed for a very long time. Since Callisto is the furthest from Jupiter and is not in resonance, it is probable that it has not suffered tidal effects as much as the other moons.

Generally, satellites' dynamics is more complex than the one of the planets, mainly because some forces become significant when the distances are small (for example tides or oblateness). A study of the main effects acting on the Jovian

	Io	Europa	Ganymede	Callisto
Physical parameters				
Mass (10^{22} kg)	8.932	4.800	14.818	10.759
Mean radius (10^3 km)	1.821	1.561	2.631	2.410
g surface (m/s^2)	1.79	1.314	1.430	1.235
Density (10^3 kg/m^3)	3.528	3.014	1.942	1.834
Orbital parameters				
Period (days)	1.7691	3.5512	7.1546	16.6890
Mean motion (°/day)	203.49	101.37	50.32	21.57
Semi-major axis (10^5 km)	4.220	6.713	10.706	18.831
Eccentricity	0.0042	0.0095	0.0013	0.0074
Inclination (°)	0.04	0.46	0.21	0.20

Table 1.1.: Overview of some Galilean satellites' physical and mean orbital parameters in an equatorial reference system at J2000.

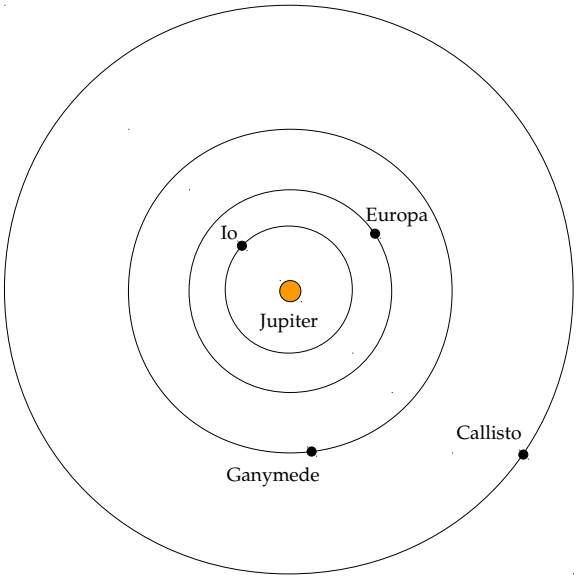

Figure 1.2.: *Scaled representation of Jupiter and the Galilean satellites' orbits.*

satellites is presented in [20]; the numerical model we will implement is mainly inspired by this paper and other following works of the same authors, such as [7], [21] and [24].

Moreover, as mentioned in the Introduction, the Galilean satellites are in a very particular motion condition: they are locked in a three-body resonance with ratio $4 : 2 : 1$. In particular, Io and Europa are in a $2 : 1$ mean motion resonance, the same of Europa and Ganymede.

One of the most fascinating aspects is that the dissipation and the resonance are strongly related one to each other. In fact, the tides could have driven the satellites in their current state, leading the inner satellites outward from Jupiter, reaching their present location. Moreover, as we will study in this part of the thesis, the resonance forces the moons' eccentricities to higher values (with respect to their free values), making the dissipation within the satellites stronger.

In order to have a clear description of the dynamics, we developed a semi-analytic model of the Galilean satellites, which we will present in Chapter 3.

2 SECULAR THEORY

In this chapter we introduce the general problem of the motion of $N+1$ point masses (m_i, $i = 0, N$) under their mutual gravitational attraction. In particular, since we are interested in the long period evolution of their orbits, we present the secular theory of the motion.

In celestial mechanics the approximation of point masses is justified by the theorem of Newton:

Theorem. *A spherically symmetric body affects external object gravitationally as though all of its mass were concentrated at a point at its center.*

In the case $N = 1$, we find the classic two-body problem. Let be $\mathbf{z}_0$ and $\mathbf{z}_1$ the barycentric positions of the two bodies, then the equations of motion are

$$\begin{cases} m_0 \ddot{\mathbf{z}}_0 = \dfrac{G m_0 m_1}{r^3} \mathbf{r}, \\ m_1 \ddot{\mathbf{z}}_1 = -\dfrac{G m_0 m_1}{r^3} \mathbf{r}, \end{cases} \tag{2.1}$$

where G is the gravitational constant (almost $6.674 \times 10^{-11}\ m^3 kg^{-1} s^2$) and $\mathbf{r} = \mathbf{z}_1 - \mathbf{z}_0$ (we use the notation $r = |\mathbf{r}|$). With a dot over a quantity we indicate the derivative with respect to the time, then $\dot{\mathbf{z}}$ is the velocity and $\ddot{\mathbf{z}}$ is the acceleration.

Subtracting the first equation multiplied by m_1 from the second one multiplied by m_0, we can reduce the problem to a motion of a single body with reduced mass $\mathcal{M} = m_0 m_1/(m_0 + m_1)$ under the central force due to a body of mass $M = m_0 + m_1$.

$$\mathcal{M} \ddot{\mathbf{r}} = -\frac{G \mathcal{M} M}{r^3} \mathbf{r} \tag{2.2}$$

The differential equation (2.2) defines the Kepler problem and it is well known that the solutions are conic sections. Solving (2.2) we obtain $\mathbf{r}(t)$ and then the solutions of (2.1). Since we will treat the motion of satellites, we consider the case of negative energy, or equivalently, elliptic orbits.

Instead of $\mathbf{r}$ and $\dot{\mathbf{r}}$, we can describe the state of the bodies through new coordinates, called orbital elements and represented in Figure 2.1. They are the semi-major axis a, the eccentricity e, the inclination I, the argument of the pericenter ω, the longitude of the node Ω and the mean anomaly ℓ. In the two-body problem the orbits are fixed, then five over six elements are constant. Only the mean

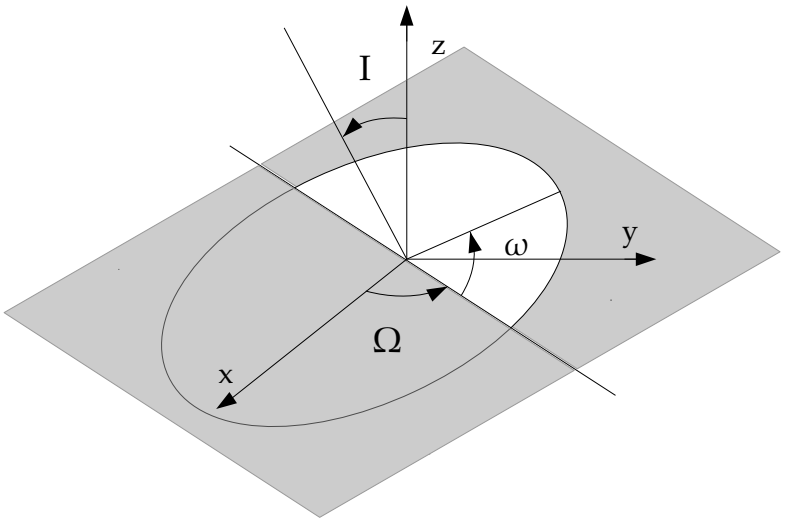

Figure 2.1.: *A generic elliptic orbit: the three angles* I, ω *and* Ω *describe the position of the ellipse in the space, while* a *and* e *define its shape.*

anomaly changes with time and it indicates the position of the body on the ellipse. Its rate is constant and it is called mean motion n.

Generally, in the real space the two-body dynamics is not enough to obtain an accurate description of the real motion. In fact, there can be other forces in the right hand side of the equations of motion (2.1) which are not negligible. Most of the times, they are small with respect to the main term due to the two-body dynamics, then we can use a perturbative approach and we suppose that at each instant the orbits are still elliptic. Because of the perturbations, the orbital elements are not constant, but they change with time.

For this reason, we introduce the notion of osculating elements: they are the instantaneous orbital elements of the body, if all perturbations vanish. Generally, they change wildly just during few orbital periods. These elements are important to have a precise knowledge of the orbit of the celestial body at a certain time t, but they are not very significant for a long period description of the motion.

There are three scales of time in celestial mechanics. Let be ϵ the small parameter of the perturbation, then we have:

- short period effects, with frequencies of the order of n;
- resonant effects, frequencies of the order of $n\sqrt{\epsilon}$;
- secular effects, frequencies of the order of $n\epsilon$.

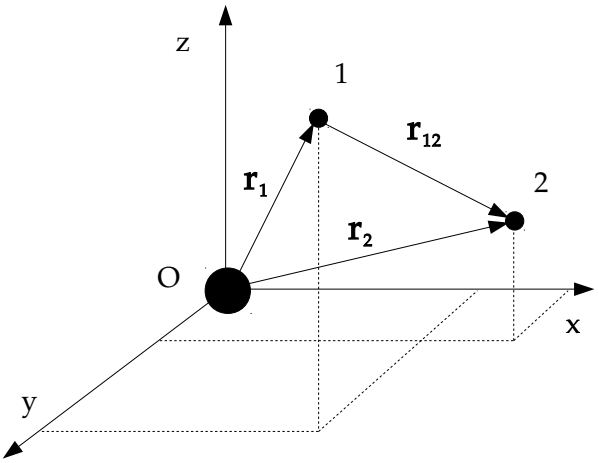

Figure 2.2.: *Three-body problem with the origin of the reference frame fixed in one of the body.*

The purpose of a secular theory is to describe the motion with elements that vary over long time scales only and that avoid the wide oscillations of the short period terms.

2.1 THIRD-BODY PERTURBATION

A classic example of perturbation is that due to the presence of a third body. If we consider the two-body problem (2.1) with a primary (mass m_0) and a secondary body (mass $m_1 \ll m_0$), it is convenient to consider a reference frame centered in the first one. This is the case of a satellite that orbits around a planet or a planet that orbits around its star. As the system is not inertial anymore, we have to consider also inertial forces and from (2.1) we obtain the acceleration

$$\ddot{\mathbf{r}}_1 = -\frac{G(m_0 + m_1)}{r_1^3}\mathbf{r}_1. \tag{2.3}$$

If we add a third body, for example another satellite with mass m_2 and planetocentric position $\mathbf{r}_2$, as represented in Figure 2.2, the secondary body will undergo a force

$$m_1\ddot{\mathbf{r}}_1 = Gm_1m_2\Big(\frac{\mathbf{r}_{12}}{r_{12}^3} - \frac{\mathbf{r}_2}{r_2^3}\Big), \tag{2.4}$$

where $\mathbf{r}_{12} = \mathbf{r}_2 - \mathbf{r}_1$ and r_{12} is its norm. In the right hand side of (2.4), the first term in the brackets is the direct term, while the second one is the indirect term, due to the new force acting on the primary.

As the two forces given by (2.3) and (2.4) are conservative, we can express them in term of a potential U. For the main term, also called Keplerian as it describes the two-body problem, we have

$$U_0 = \frac{G(m_0 + m_1)}{r_1}, \tag{2.5}$$

while for the third-body perturbation

$$U_{3b} = Gm_2\Big(\frac{1}{r_{12}} - \frac{\mathbf{r}_1 \cdot \mathbf{r}_2}{r_2^3}\Big). \tag{2.6}$$

In this case, the small parameter of the perturbation is $\epsilon = m_2/m_0$.

2.2 HAMILTONIAN THEORY

Since we will use the Hamiltonian formalism, we recall its main properties. We consider a function $\mathcal{H}(\mathbf{p}, \mathbf{q})$, called Hamiltonian, that depends on some coordinates $\mathbf{q}$ and their conjugated momenta $\mathbf{p}$.

From this function, we can define a system of first order differential equations

$$\begin{cases} \dot{\mathbf{p}} = -\dfrac{\partial \mathcal{H}}{\partial \mathbf{q}}, \\ \dot{\mathbf{q}} = \dfrac{\partial \mathcal{H}}{\partial \mathbf{p}}, \end{cases} \tag{2.7}$$

called Hamilton's equations. From (2.7), it is easy to verify that the Hamiltonian is a first integral of the motion.

We recall also the notion of canonical transformations. They are special variables transformations

$$\phi : (\mathbf{p}, \mathbf{q}) \mapsto (\mathbf{P}, \mathbf{Q}),$$

for which the Hamilton's equations relative to the new Hamiltonian

$$\mathcal{H}'(\mathbf{P}, \mathbf{Q}) = \mathcal{H}(\mathbf{p}(\mathbf{P}, \mathbf{Q}), \mathbf{q}(\mathbf{P}, \mathbf{Q}))$$

express the same dynamics of the initial differential equations.

An example of canonical transformation is the integral flow $\Phi^t_{\mathcal{H}}(\mathbf{x})$. In fact, if we consider the map $\mathbf{x} \mapsto \Phi^t_{\mathcal{H}}(\mathbf{x})$, we pass to a new Hamiltonian system, where in this case the Hamiltonian remains the same.

Another way to create canonical transformations is to use generating functions. They are functions of the coordinates (old or new) and the momenta (old or new).

For example, we suppose to have a function $F(\mathbf{q}, \mathbf{P})$ defined in an open domain and such that

$$\det\Big(\frac{\partial^2 F}{\partial \mathbf{q} \partial \mathbf{P}}\Big) \neq 0.$$

In order to obtain the associated canonical transformation, we have to compute the partial derivatives

$$\mathbf{Q} = \frac{\partial F}{\partial \mathbf{P}}\ , \qquad \mathbf{p} = \frac{\partial F}{\partial \mathbf{q}}\ ,$$

and through an inversion we get the expressions for the new momenta $\mathbf{P}$.

2.2.1 *Poincaré canonical coordinates*

Relative, or planetocentric, coordinates are not canonical variables, then we need to use different coordinates. We consider $N+1$ bodies with mass m_i and barycentric positions $\mathbf{z}_i$, $i = 0, N$. The idea is to pass to a mixed set of variables, known also as Poincaré coordinates: relative positions $\mathbf{r}_i = \mathbf{z}_i - \mathbf{z}_0$ and barycentric momenta $\mathbf{p}_i = m_i \dot{\mathbf{z}}_i$, $i = 1, N$. Instead, for the central body we take $\mathbf{r}_0 = \mathbf{z}_0$ and $\mathbf{p}_0 = \sum_{i=0}^{N} \mathbf{p}_i$.

The Hamiltonian is the sum of the kinetic energy

$$T = \frac{1}{2} \sum_{i=1}^{N} p_i^2 \Big(\frac{1}{m_i} + \frac{1}{m_0}\Big) + \frac{1}{2} \frac{p_0^2}{m_0} - \sum_{i=1}^{N} \frac{\mathbf{p}_0 \cdot \mathbf{p}_i}{m_0} + \sum_{0<i<k\leqslant N} \frac{\mathbf{p}_i \cdot \mathbf{p}_k}{m_0}$$

and the potential energy

$$U = -G \sum_{i=1}^{N} \frac{m_0 m_i}{r_i} - G \sum_{0<i<k\leqslant N} \frac{m_i m_k}{r_{ik}}.$$

Since $\mathbf{r}_0$ is missing, the conjugated momentum $\mathbf{p}_0$ is constant and we can set it to 0. We can reduce the problem to $3N$ degrees of freedom and the new Hamiltonian is

$$\mathcal{H} = \sum_{i=1}^{N} \Big(\frac{|\mathbf{p}_i|^2}{2\beta_i} - \frac{\mu_i \beta_i}{|\mathbf{r}_i|}\Big) + \sum_{0<i<k\leqslant N} \Big(-\frac{G m_i m_k}{|\mathbf{r}_{ik}|} + \frac{\mathbf{p}_i \cdot \mathbf{p}_k}{m_0}\Big), \tag{2.8}$$

where $\beta_i = m_0 m_i/(m_0 + m_i)$ and $\mu_i = G(m_0 + m_i)$.

It is worth noting that the first sum is the unperturbed Hamiltonian, composed just by two-body problems between the bodies 0 and i, while the second sum is due to the interactions between the bodies with $i = 1, N$. Moreover, with this formulation, the indirect part of the third-body perturbation (2.6) comes out from the kinetic part and not from the potential one.

2.2.2 *Delaunay variables*

Since we are interested in the secular theory of the motion, we need to use variables that vary slowly. Unfortunately, the orbital elements are not canonical. Therefore, it is necessary to consider another set of variables, in particular we choose the Delaunay variables. Starting from the Poincaré coordinates, the momenta are defined as follows

$$\tilde{L}_i = \beta_i \sqrt{G(m_0 + m_i)a_i}, \qquad \tilde{G}_i = \tilde{L}_i \sqrt{1 - e_i^2}, \qquad \tilde{H}_i = \tilde{G}_i \cos I_i.$$

The associated coordinates are the mean anomaly ℓ_i, the argument of the pericenter ω_i and the longitude of the node Ω_i.

Delaunay variables are action-angle canonical variables, which are suitable for integrable or quasi-integrable systems. Action-angle variables are a particular set of momenta and coordinates, for which the Hamiltonian depends only on the momenta and the solutions are contained in tori parametrized by the angle coordinates. In the case of the two-body problem, for which only $\tilde{L}$ appears in the Hamiltonian, we have that $\tilde{L} = h$ defines a 1-dimensional torus which is parametrized by ℓ. In the perturbed problem, there are conditions for which some tori in the space persist, if the perturbation is small enough (KAM theory).

The Delaunay variables have some singularities in their definition. In fact, when we consider circular orbits ($e = 0$), the angle ω is not defined, instead for planar orbits ($I = 0$ or $I = \pi$), Ω is not defined.

In order to remove these singularities, we can consider other canonical variables. First of all we pass to an intermediate set of canonical variables, called modified Delaunay variables, with new momenta

$$L_i = \tilde{L}_i, \qquad G_i = \tilde{L}_i - \tilde{G}_i, \qquad H_i = \tilde{G}_i - \tilde{H}_i, \tag{2.9}$$

while the new coordinates are the mean longitude $\lambda = \ell + \omega + \Omega$, minus the longitude of pericenter $\varpi = \omega + \Omega$ and minus the longitude of the node Ω.

In order to remove the singularities, we can use rectangular variables, which are defined as follows

$$\begin{aligned} x_i &= \sqrt{2G_i}\cos(\varpi_i), \qquad & y_i &= \sqrt{2G_i}\sin(\varpi_i), \\ u_i &= \sqrt{2H_i}\cos(\Omega_i), \qquad & v_i &= \sqrt{2H_i}\sin(\Omega_i); \end{aligned}$$

while L_i and λ_i remain the same.

In the Delaunay variables the unperturbed Hamiltonian becomes

$$\mathcal{H}_0 = -\sum_{i=1}^{N} \frac{\mu_i^2 \beta_i^3}{2L_i^2}. \tag{2.10}$$

From (2.10), the mean motions are $n_i = \mu_i^2 \beta_i^3 / L_i^3$.

2.3 EXPANSION OF THE PERTURBATION

From the celestial mechanics theory (see for example [10] or [34], Chapter 6), we know that (2.6) can be expanded in a Fourier series of cosines only

$$R^{(i,k)} = -\frac{G m_i m_k}{a_k} \sum_{\mathbf{j} \in \mathbb{N}^6} C_{\mathbf{j}}(a_i, a_k, e_i, e_k, I_i, I_k) \cos(\mathbf{j} \cdot \Theta), \tag{2.11}$$

where $\mathbf{j} = (j_l)_{l=1,6}$ is an integer vector and $\boldsymbol{\Theta} = (\lambda_i, \lambda_k, \varpi_i, \varpi_k, \Omega_i, \Omega_k)$. The expansion (2.11) is related to two generic bodies that orbit around the same object, and we indicate the inner one with the letter i and the outer one with k.

Moreover, from geometric and invariance considerations, we know that not all the terms of the series are allowed. Apart from restricting the expansion to cosines only, the D'Alembert rules say that each term must verify:

1. the sum of the coefficients j_l ($l = 1, 6$) is 0;
2. the sum of the coefficients of the variables Ω is even;
3. the minimum order in eccentricity (respectively inclination) of a term is equal to the sum of the absolute values of the coefficients of ϖ (respectively Ω).

From the third law we have that the main term of $C_{\mathbf{j}}$ is

$$c_{\mathbf{j}}(a_i/a_k) e_i^{|j_3|} e_k^{|j_4|} s_i^{|j_5|} s_k^{|j_6|}.$$

where $s_i = \sin(I_i/2)$ (analogous formula for s_k), and $c_{\mathbf{j}}(a_i/a_k)$ depends on the semi-major axes only, actually on their ratio a_i/a_k, and it is a combination of functions called Laplace coefficients. In order to compute the various coefficients $c_{\mathbf{j}}$, we refer to [34], Appendix B, which reports their exact formulas.

Since (2.11) is an expansion in e and $\sin(I/2)$, which in most of the cases are far smaller than 1, we can stop the expansion at an order for which the terms become small enough.

Once we consider (2.11), the Hamiltonian is in the form

$$\mathcal{H} = \mathcal{H}_0 + \epsilon \mathcal{H}_1. \tag{2.12}$$

In fact, we can separate $\mathcal{H}$ in the main and unperturbed part given by (2.10), and a perturbative part linear in the small parameter ϵ.

In the next section we will see how we can eliminate most of the terms of (2.11) through an operation of averaging.

2.4 AVERAGING

Since we want to pass to a secular theory, we need to remove all the short period terms from the Hamiltonian. This is possible through an operation called averaging, which is equivalent to calculate the mean of the Hamiltonian over the fast angles.

We use an approach based on Lie series. They allow to eliminate the terms of the expansion, through a canonical transformation (see [31]).

We showed that the Hamiltonian is in the form (2.12), where $\mathcal{H}_0$ is the Keplerian part and $\epsilon\mathcal{H}_1$ is the third-body perturbation. We can introduce a function $\chi = \epsilon\chi_1 + \epsilon^2\chi_2 + \dots$ that defines a canonical transformation ϕ_χ^ϵ such that, if we indicate with $\mathcal{H}' = \mathcal{H}'_0 + \epsilon\mathcal{H}'_1 + \epsilon^2\mathcal{H}'_2 + \epsilon^3\mathcal{H}'_3 + \dots$, the new Hamiltonian is

$$\begin{aligned}
\mathcal{H}'_0 =& \mathcal{H}_0,\\
\mathcal{H}'_1 =& \mathcal{H}_1 - \{\mathcal{H}_0, \chi_1\},\\
\mathcal{H}'_2 =& -\{\mathcal{H}_0, \chi_2\} - \{\mathcal{H}_1, \chi_1\} + 1/2\{\{\mathcal{H}_0, \chi_1\}, \chi_1\},\\
\mathcal{H}'_3 =& \dots
\end{aligned} \tag{2.13}$$

Through this procedure, we want to remove all the short period terms from $\mathcal{H}_1$, obtaining a new perturbative function $\mathcal{H}'_1$ with secular terms only.

In (2.13) we used the Poisson's brackets, which define the operation

$$\{f, g\} = \sum_i \Big(\frac{\partial f}{\partial q_i}\frac{\partial g}{\partial p_i} - \frac{\partial f}{\partial p_i}\frac{\partial g}{\partial q_i} \Big).$$

Therefore, if we want to remove a term in $\mathcal{H}_1$ containing $\alpha\lambda_2 - \beta\lambda_1$ in the argument of the cosine, for example

$$\mathcal{H}_1^{(\alpha,\beta)} = A(a_1, a_2) e_2^{|\alpha-\beta|} \cos(\alpha\lambda_2 - \beta\lambda_1 - (\alpha-\beta)\varpi_2),$$

we must define

$$\chi_1^{(\alpha,\beta)} = \frac{A(a_1, a_2)}{\alpha n_2 - \beta n_1} \sin(\alpha\lambda_2 - \beta\lambda_1 - (\alpha-\beta)\varpi_2).$$

In this way, since $\mathcal{H}_0$ depends on L_1 and L_2 only,

$$\begin{aligned}
\{\mathcal{H}_0, \chi_1^{(\alpha,\beta)}\} &= -\frac{\partial \mathcal{H}_0}{\partial L_1}\frac{\partial \chi_1^{(\alpha,\beta)}}{\partial \lambda_1} - \frac{\partial \mathcal{H}_0}{\partial L_2}\frac{\partial \chi_1^{(\alpha,\beta)}}{\partial \lambda_1} \\
&= -n_1 \frac{A(a_1,a_2)}{\alpha n_2 - \beta n_1} e_2^{|\alpha-\beta|}\cos(\alpha\lambda_2 - \beta\lambda_1 - (\alpha-\beta)\varpi_2)(-\beta) \\
&\quad - n_2 \frac{A(a_1,a_2)}{\alpha n_2 - \beta n_1} e_2^{|\alpha-\beta|}\cos(\alpha\lambda_2 - \beta\lambda_1 - (\alpha-\beta)\varpi_2)\alpha \\
&= -(\alpha n_2 - \beta n_1)\frac{A(a_1,a_2)}{\alpha n_2 - \beta n_1} e_2^{|\alpha-\beta|}\cos(\alpha\lambda_2 - \beta\lambda_1 - (\alpha-\beta)\varpi_2) \\
&= -A(a_1,a_2) e_2^{|\alpha-\beta|}\cos(\alpha\lambda_2 - \beta\lambda_1 - (\alpha-\beta)\varpi_2) = -\mathcal{H}_1^{(\alpha,\beta)}.
\end{aligned}$$

As shown in (2.13), this operation generates a new part $\mathcal{H}_2'$, but formally it is of the second order in the small parameter ϵ, then we can neglect it in an approximated model.

Apart from modifying the Hamiltonian, we are also changing the variables. In particular, when we conclude our operation of averaging, removing all the fast angles, we have new variables called mean orbital elements, which are different from the previous osculating elements.

The purpose of this procedure is to eliminate all the terms containing the mean longitudes, since their variation is faster than that of the other angles (ϖ_i and Ω_i, which vary only under the action of the perturbations). However, because of mean motion resonances, we have that some combinations $\alpha\lambda_2 - \beta\lambda_1$ have smaller rate than the mean longitudes alone.

Therefore, when we try to eliminate this term using Lie series, amongst the second order terms we have

$$\{\{\mathcal{H}_0, \chi_1^{(\alpha,\beta)}\}, \chi_1^{(\alpha,\beta)}\} = \{-\mathcal{H}_1^{(\alpha,\beta)}, \chi_1^{(\alpha,\beta)}\}.$$

The quantity $\chi_1^{(\alpha,\beta)}$ contains the factor $1/(\alpha n_2 - \beta n_1)$, and when we derive with respect to L_1 or L_2 we obtain $1/(\alpha n_2 - \beta n_1)^2$. As we said, the frequencies of the resonances are of the order of $n\sqrt{\epsilon}$, therefore, at the denominator we have a quantity that is near ϵ.

This is the problem of the small divisors and we cannot omit the terms containing these combinations without obtaining a bad approximation. In fact, in $\mathcal{H}_2'$ we find ϵ at the denominator, so that the real order of the associated function in the small parameter is one and not two.

In the next section we will show some examples for which the mean motion resonances have a very important impact in the evolution of the orbits.

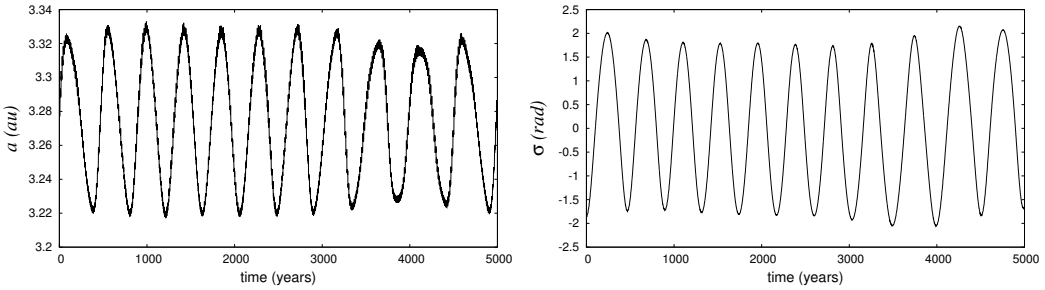

Figure 2.3.: *The semi-major axis* a *of the asteroid Dirichlet (left) and the resonant angle* $\sigma = 2\lambda_5 - \lambda - \varpi$ *(right).*

2.5 MEAN MOTION RESONANCES

Orbital resonances are not uncommon in the Solar System. In the main belt of asteroids between Mars and Jupiter, we can find several groups of asteroids in mean motion resonance with Jupiter. In the literature there are several works devoted to the study of resonant dynamics (see [33] and [36]).

If we take the acceleration of a main belt asteroid, we have a main term due to the gravitational force of the Sun and a secondary term due to the third-body perturbations of the planets. In particular, due to the great mass of Jupiter and the asteroid's position, we can consider just the perturbation due to the gas giant. In certain regions of the belt, it happens that asteroids suffer a strong influence by Jupiter. We know that the mean motion depends on the semi-major axis, therefore, we take an asteroid with a semi-major axis such that

$$jn - kn_5 \approx 0,$$

for certain integers j and k greater than 0. The number 5 indicates Jupiter, fifth planet of the Solar system. In this case, it is a mean motion resonance of ratio $j : k$ and order $|j - k|$.

If an asteroid is near to a resonance, then the terms of the series containing the combination $j\lambda - k\lambda_5$ have an important impact on the motion, inducing important variations in the orbital elements. If the resonance is strong enough, there can be angles that pass from circulation, i.e. a very small variation along $[0, 2\pi]$, to libration, i.e. an oscillation around a fixed value.

We reported as example the asteroid Dirichlet (number 11665), which is a main belt asteroid in $1 : 2$ resonance with Jupiter. Since the order of the resonance is 1, the resonant effects are quite strong. In fact, the main resonant term is linear in e. For the propagation of the asteroid we used orbit9, a code included in the OrbFit software and developed by the Celestial Mechanics Group of Pisa (see [30]). As shown in Figure 2.3, the resonant angle is librating around 0 and the variation

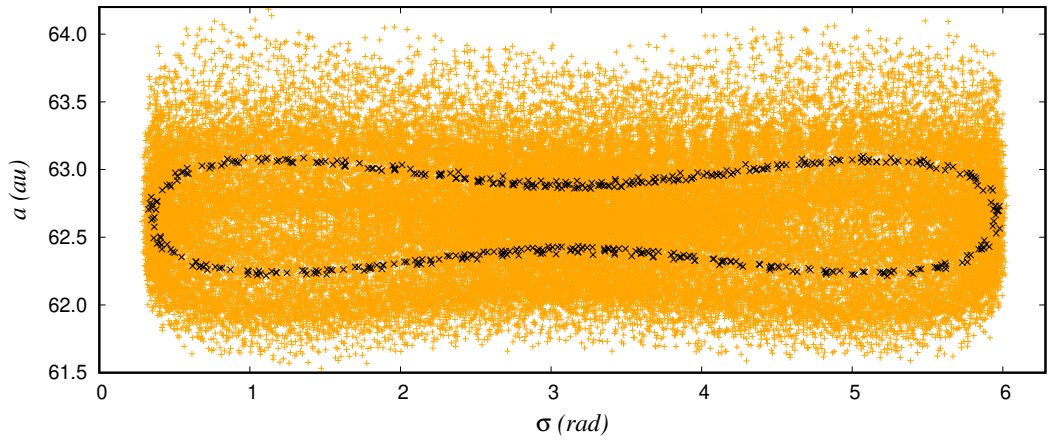

Figure 2.4.: *Points from an integration of the asteroid 136120 in the plane* (a, σ)*, with* a *the semi-major axis of the asteroid and* σ *the resonant angle. In orange we reported the points obtained by the numerical integration, while in black the same series after the application of a low pass filtering.*

of the semi-major axis is strongly influenced by the resonance, oscillating with an amplitude of almost 0.05 au and the period of the libration. In this case the resonant angle is $2\lambda_5 - \lambda - \varpi$, but how can we guess which it is? From the D'Alembert rules, we know that the combination $2\lambda_5 - \lambda$ must be completed in such a way that the sum of the coefficients is equal to 0. Since we search for terms with the minimum order in eccentricities and inclinations, and the sum of the coefficients of Ω angles must be even, the natural choice is $-\varpi$ or $-\varpi_5$. However, the eccentricity of Jupiter is generally smaller (almost 0.048) than the ones of the asteroids (in the case of Dirichlet, it is almost 0.15), then the first attempt should be $-\varpi$.

Resonances do not occur only for main belt asteroids, but also in other scenarios, such as transneptunian asteroids (resonance with Neptune), exoplanets of a same star (resonance between themselves) and satellites of a same planet (resonance between themselves).

In [40], we studied the orbital evolution of some transneptunian objects in mean motion resonance with Neptune. Also in this case we used orbit9 software for the numerical propagation. We report just an example of a resonant asteroid, numbered with 136120, for which the resonance with Neptune has commensurability $1 : 3$.

In the paper we used numerical integrations in order to find suitable initial conditions for the secular model developed in [39]. In particular, applying a digital filter to the semi-major axis of the asteroid and the resonant angle $\sigma = 3\lambda - \lambda_8 - 2\varpi$ (8 indicates Neptune, eighth and last planet of the Solar system), we found the corresponding level curve of the semi-secular Hamiltonian. In the case of 136120, as it is showed Figure 2.4, the mean elements (a, σ) follow a horse-shoe shape

curve, librating around an unstable equilibrium point. One of the parameter we had to calculate in order to use the secular model was the area contained inside the level curve we found, which is related to the angular momentum of the asteroid that is conserved for the adiabatic approximation.

In the case of the Galilean satellites we know that the system is near two 2 : 1 mean motion resonances, being $n_1 - 2n_2 \approx 0$ and $n_2 - 2n_3 \approx 0$. From the D'Alembert rules, the resonant angles must contain also the longitudes of the pericenters. In particular the following relations are verified

$$\begin{aligned} &\lambda_1 - 2\lambda_2 + \varpi_1 \approx 0^\circ, \\ &\lambda_1 - 2\lambda_2 + \varpi_2 \approx 180^\circ, \\ &\lambda_2 - 2\lambda_3 + \varpi_2 \approx 0^\circ, \end{aligned} \tag{2.14}$$

where the approximately equal signs indicate that the value of the angles is not fixed, but they librate around it. The combinations (2.14) mean that whether Io and Europa are in conjunction ($\lambda_1 = \lambda_2$), then Io is near its pericenter (first relation) and Europa is near its apocenter (second relation); while, whether Europa and Ganymede are in conjunction ($\lambda_2 = \lambda_3$), then Europa is near its pericenter (third relation). From (2.14) we find that

$$\phi = \lambda_1 - 3\lambda_2 + 2\lambda_3 \approx 180^\circ, \tag{2.15}$$

which is the resonant angle related to the three-body mean motion resonance and from which we obtain the classic relation on the mean motions

$$n_1 - 3n_2 + 2n_3 \approx 0. \tag{2.16}$$

From (2.16) we have the inequality

$$\nu = n_1 - 2n_2 \approx n_2 - 2n_3, \tag{2.17}$$

that nowadays is equal to $0.7395\ \mathrm{rad/day}$, which is minus the current rate of change of the longitudes of the pericenters ϖ_1 and ϖ_2.

The conditions (2.14) with equals instead of approximately equals, coupled with the ulterior condition $\lambda_2 - 2\lambda_3 + \varpi_3 = 180^\circ$, characterize the so-called de Sitter resonance. It is the special case, studied in [6], for the existence of periodic orbits of the system composed by Io, Europa and Ganymede.

In Chapter 3 we implement a semi-analytical model of the motion of the Galilean satellites, in order to study the main features of their dynamics, including the three-body mean motion resonance.

3 THE DYNAMICAL MODEL

Dynamical models based on analytical expansions of the perturbative functions were commonly used in the last century, in order to study the motion of the Galilean satellites. For models that include a large number of terms, a numerical integration of the resulting differential equations is necessary to obtain a precise output from the model. For this reason this kind of models are called semi-analytical.

In the introduction, we presented [6] as first example of sophisticated dynamical model of the Galilean satellites' motion. However, other works, such as [45], developed and implemented more precise models in order to study the Laplace resonance. After the discovery of the huge tidal friction within Io, some authors, such as in [28] and [50], used a semi-analytical approach in order to investigate the origin and the evolution of the system. More recently, in [5], the authors studied the de Sitter resonance and the configurations near this state.

Although in the literature there are several Galilean satellites' semi-analytical models, we developed our own (presented in [27]) mainly for four reasons:

- to have a model we can modify as we want. We can add or remove single terms in order to verify their effect in the dynamics; moreover, we can investigate by our own the evolution of the system due to the tidal dissipation.
- To have a good description of all the orbital elements. Generally, in the papers of the past, it was supposed a planar motion; instead, we want to take into account also the nodes and the inclinations of the moons.
- To add effects that in other models were not included. In fact, since the interest was focused on the three inner Galilean satellites, generally Callisto was not considered in the propagation. And more, since the inclinations were set to 0, also the Sun was neglected. Both the two bodies are very important to approximate well the actual dynamics of the moons.
- To show, by a comparison with numerical models, that a semi-analytical model can really capture all the main resonant and secular features of the dynamics.

The reason of the differences with previous models is due to their aims: the Laplace resonance and the tidal effects involve mainly the three inner Galilean

satellites; moreover, the inclinations do not give a direct contribution to the problem. However, the combination of all the effects can bring to some differences for long period propagations; we will present the example of the mutual perturbation between Ganymede and Callisto. Therefore, we preferred to implement a model able to replicate all the details of the actual dynamics, in order to better describe the mean and long-term evolution of the motion.

In order to develop our model, we use the theory presented in Chapter 2; in particular, we fix an equatorial reference system and we consider Poincaré coordinates and Delaunay variables. We know that if we consider just the two-body dynamics of the moons and Jupiter, the unperturbed Hamiltonian is described by (2.10), with $N = 4$. If $\mathcal{H} = \mathcal{H}_0$, only λ_i change with time, while the other orbital parameters remain constant. This is far from the actual dynamics of the Jovian system. There are several additional forces that influence the satellites' dynamics, and some of them have very important effects on the motion.

3.1 PERTURBATIONS

The choice of which forces to include into the model depends on its purpose. If we want a dynamical model for very precise ephemerides or for predicting very accurate observations (as for example spacecraft tracking data), we have to consider a long list of perturbations. However, this is not the case of a semi-analytical model, whose task is to capture the main features of the resonant and secular motion. In the model we included the following perturbations:

- quadrupole moment J_2 of the Jupiter's gravitational field,
- mutual gravitational perturbation between the satellites,
- third-body perturbation of the Sun,
- octopole moment J_4 of the Jupiter's gravitational field.

In [20] it is shown that these forces are by far the most important perturbations in the Jovian system. In particular, the following force in the list would be the effect of the coefficient C_{22} of the Io's gravitational field, whose effect on the mean longitude of the little moon is more than ten times smaller than the one of J_4. Since the effect of J_4 is quite limited, at least for the purpose of our model, we can represent very well the actual dynamics with just the forces reported in the list.

3.1.1 *Jupiter's oblateness*

Jupiter is not a perfect sphere, but it is more flat toward its equator. Therefore, for a more realistic model, we cannot approximate its gravitational field as a point mass only, but we have to take into account its shape.

In order to do this, we add the acceleration due to the gravitational anomalies of an extended body, as described in [32]. We consider an expansion of the gravitational potential in zonal harmonics

$$U_{obl} = -\frac{Gm_0}{r}\sum_{l=2}^{\infty} J_l\left(\frac{R_0}{r}\right)^l P_l(\sin\phi), \tag{3.1}$$

where the coefficients J_l characterize the field, R_0 is the radius of the planet (fixed to 71398 km) and ϕ is the latitude of the body in an equatorial system. In the case of Jupiter, the most important terms are the ones with J_2 and J_4; the values of the parameters are respectively -0.01735 and 0.000588, as taken from the ephemerides L3 of the IMCCE.

In order to add this perturbation into the model, we have to take its secular part. In (3.1), we replace r with its expression in terms of the orbital elements $r = a(1 + e\cos(E))$, where E is the eccentric anomaly and it is related to the mean anomaly by the relation $\ell = E - e\sin(E)$.

Finally, we perform an averaging over the variable E. We do not report here the details, which can be found in [34], Chapter 6. We add to the Hamiltonian the resulting secular perturbative functions ($i = 1, 4$):

$$\begin{aligned} R_J^{(i)} = &-\frac{Gm_0}{a_i}\Big[\frac{1}{2}J_2\left(\frac{R_0}{a_i}\right)^2 - \frac{3}{8}J_4\left(\frac{R_0}{a_i}\right)^4 + \left(\frac{3}{4}J_2\left(\frac{R_0}{a_i}\right)^2 - \frac{15}{8}J_4\left(\frac{R_0}{a_i}\right)^4\right)e_i^2 \\ &- \left(\frac{3}{4}J_2\left(\frac{R_0}{a_i}\right)^2 - \frac{15}{8}J_4\left(\frac{R_0}{a_i}\right)^4\right)s_i^2\Big], \end{aligned}$$

with $s_i = \sin(I_i/2)$.

3.1.2 *Mutual perturbations*

From (2.4), we know that each satellite is accelerated by the others. As shown in Chapter 2, the perturbative function can be expanded in a Fourier series (2.11). From the averaging operation we remain with long periodic, resonant and secular terms; for this reason we define the model semi-secular, or resonant. We choose to include all the terms up to order three in eccentricities and inclinations. Generally, for the Galilean satellites, expansions up to second order are enough to have a good representation of the orbital elements, however, we noted that the improvement given by the third order terms is worth being added to have a better matching with the actual dynamics.

We avoid writing here the whole Hamiltonian of the mutual perturbations (that can be found in Appendix A), however, as example, we write below the potential between Io and Europa (for the sake of simplicity we reported the terms up to the

second order). The only small divisor is $2n_2 - n_1$, then we keep the terms with arguments containing $2\lambda_2 - \lambda_1$.

$$\begin{aligned}
R^{(1,2)} = &- \frac{Gm_1m_2}{a_2}\Big\{c_{(0,0,0,0,0,0)}(a_1/a_2) \\
&+ c^1_{(0,0,0,0,0,0)}(e_1^2 + e_2^2) + c^2_{(0,0,0,0,0,0)}(s_1^2 + s_2^2) \\
&+ c_{(0,0,-1,1,0,0)}e_1e_2\cos(\varpi_2 - \varpi_1) + c_{(0,0,0,0,-1,1)}s_1s_2\cos(\Omega_2 - \Omega_1) \\
&+ c_{(-1,2,-1,0,0,0)}(a_1/a_2)e_1\cos(2\lambda_2 - \lambda_1 - \varpi_1) \\
&+ c_{(-1,2,0,-1,0,0)}(a_1/a_2)e_2\cos(2\lambda_2 - \lambda_1 - \varpi_2) \\
&+ c_{(-2,4,-2,0,0,0)}e_1^2\cos(4\lambda_2 - 2\lambda_1 - 2\varpi_1) \\
&+ c_{(-2,4,0,-2,0,0)}e_2^2\cos(4\lambda_2 - 2\lambda_1 - 2\varpi_2) \\
&+ c_{(-2,4,-1,-1,0,0)}e_1e_2\cos(4\lambda_2 - 2\lambda_1 - \varpi_1 - \varpi_2) \\
&+ c_{(-2,4,0,0,-2,0)}s_1^2\cos(4\lambda_2 - 2\lambda_1 - 2\Omega_1) \\
&+ c_{(-2,4,0,0,0,-2)}s_2^2\cos(4\lambda_2 - 2\lambda_1 - 2\Omega_2) \\
&+ c_{(-2,4,0,0,-1,-1)}s_1s_2\cos(4\lambda_2 - 2\lambda_1 - \Omega_1 - \Omega_2)\Big\}. \qquad (3.2)
\end{aligned}$$

The linear terms in e_i influence strongly Io and Europa's orbits; we will show their effects in the next section. It is worth noting that only for their coefficients and the first term $c_{(0,0,0,0,0,0)}$ we consider the dependence on the semi-major axes in the derivation of the Hamilton's equations, while the others c_j are computed at the beginning of the propagation and are left fixed. However, also second order terms are necessary for a good representation of the motion. As we said, third order terms add small details, that bring to an excellent comparison with the actual dynamics, especially for the eccentricity of Io and the inclinations. The terms can be classified in terms of their arguments:

$0,\ \varpi_2 - \varpi_1,\ \Omega_2 - \Omega_1,$	secular;
$2\lambda_2 - \lambda_1 - \varpi_1,\ 2\lambda_2 - \lambda_1 - \varpi_2,$	first order resonant;
$4\lambda_2 - 2\lambda_1 - 2\varpi_2,\ 4\lambda_2 - 2\lambda_1 - 2\varpi_1,$	
$4\lambda_2 - 2\lambda_1 - \varpi_2 - \varpi_1,\ 4\lambda_2 - 2\lambda_1 - 2\Omega_1,$	
$4\lambda_2 - 2\lambda_1 - 2\Omega_2,\ 4\lambda_2 - 2\lambda_1 - \Omega_2 - \Omega_1,$	second order resonant.

The perturbation between Europa and Ganymede is similar to the previous, while for the couple Io-Ganymede, since we truncate the expansion at the third order, we have to consider the angles' combinations containing $4\lambda_3 - \lambda_1$. For all the other couples (Io-Callisto, Europa-Callisto and Ganymede-Callisto) we keep only the secular terms.

3.1.3 *Sun's perturbation*

The last perturbation that has a significant effect on the dynamics is the gravitational perturbation of the Sun. In particular, the inclinations of the outer satellites are strongly influenced by the star and if we did not consider it, the result would be completely different from their actual behaviour.

We make the reasonable approximation for which the star is not affected by the moons, so that for the Sun's propagation we have to integrate a simple two-body dynamics with Jupiter. As the planet is in the origin, we have the Sun orbiting around the planet.

Since the period of revolution of the Sun around Jupiter is almost 11 years, which is comparable to the resonant time scale, we have to pay attention to which terms to keep in the expansion. We can use the same approach we adopted for the mutual perturbation between the moons, but we cannot discard indiscriminately the longitude of the Sun λ_s, since in the context of the Galilean satellites' motion it is a slow angle. However, we can eliminate all the arguments containing the longitudes of the moons, as they are still short period terms. In the end, the terms we have to include in the model are the secular ones and others we call mid-period terms. Their arguments are:

$$\begin{aligned} &0,\ \varpi_s - \varpi_i,\ \Omega_s - \Omega_i, && \text{secular;} \\ &\lambda_s - \varpi_i,\ 2\lambda_s - 2\varpi_i,\ 2\lambda_s - \varpi_s - \varpi_i, \\ &2\lambda_s - 2\Omega_i,\ 2\lambda_s - \Omega_s - \Omega_i, && \text{mid-period.} \end{aligned}$$

3.2 FORCED ECCENTRICITIES

Even if we will present the results of the model's propagation in the next sections, we want to highlight the importance to have a model based on an analytical expansion of the perturbations.

As in this section we want to show some important effects on the orbital elements, we do not use the Hamilton's equations, but we consider the Lagrange planetary equations (see [34], Chapter 6). They are differential equations of the orbital elements obtained from the Lagrangian of the system.

In particular, we are interested in the differential equation for ϖ_1, considering just the J_2 perturbation and the linear term in e_1 of the mutual perturbation be-

tween Io and Europa (3.2). For these perturbations, the approximated Lagrange equation is

$$\begin{aligned}\dot{\varpi}_1 &= \frac{1}{m_1 n_1 a_1^2 e_1}\frac{\partial R}{\partial e_1}\\ &= \frac{1}{m_1 n_1 a_1^2 e_1}\Big(\frac{3}{2}\frac{Gm_0}{a_1}J_2\frac{R_0^2}{a_1^2}e_1 + \frac{Gm_1 m_2}{a_2}c_{(-1,2,-1,0,0,0)}e_1\cos(2\lambda_2-\lambda_1-\varpi_1)\Big)\\ &\approx n_1\Big(\frac{3}{2}J_2\frac{R_0^2}{a_1^2} + \frac{m_2}{m_0}\frac{a_1}{a_2}c_{(-1,2,-1,0,0,0)}\frac{1}{e_1}\cos(2\lambda_2-\lambda_1-\varpi_1)\Big).\end{aligned}$$

From (2.14), we know that $2\lambda_2-\lambda_1-\varpi_1$ is a resonant angle that librates around 0 and from (2.17) it must be $\dot{\varpi}_1 = 2n_2-n_1 \approx -0.7395\ ^\circ/day$. From the first term of the second hand side we can estimate the contribution of J_2, which is almost $0.1256\ ^\circ/day$. Moving it over to the left-hand side of the equation, we get $\dot{\varpi}_1^* = \dot{\varpi}_1 - 0.1256 = -0.8561$. We invert the relation between ϖ_1 and e_1 and we find

$$e_1 = n_1\frac{m_2}{m_0}\frac{a_1}{a_2}c_{(-1,2,-1,0,0,0)}\frac{1}{\dot{\varpi}_1^*} \approx 0.0045,$$

which is almost equal to the total mean value of Io's eccentricity (see Table 1.1). This shows that the orbital element is forced to its current value by the mean motion resonance with Europa.

A similar analysis can be done for Europa, considering both the perturbation with Io and the one with Ganymede. The forced eccentricity of Io due to the resonance with Europa is essential to recover the huge tidal dissipation within the satellite.

3.3 RESONANT VARIABLES

In (2.11) we have an expansion in eccentricities e_i and sinus of inclinations s_i, but we need to write the expansion in terms of canonical variables, in order to use the Hamiltonian theory. The variables we choose are the ones defined in (2.9). As the eccentricities and the inclinations are small, we consider the following approximations (for $i = 1,4$)

$$e_i \approx \sqrt{\frac{2G_i}{L_i}}, \qquad s_i \approx \sqrt{\frac{H_i}{2L_i}}.$$

As shown in Chapter 2, a generic $N+1$-body problem can be reduced to $3N$ degrees of freedom. Therefore, since in the case of the Galilean satellites $N = 4$, we start with 24 variables (6 per moon). Since the Sun motion is determined by a simple two-body dynamics, we have constant values for all its orbital elements, except for the mean longitude.

Since we want to study the secular dynamics, we can make an ulterior reduction of the problem. In fact, once we write the whole Hamiltonian, we can check if some variables are missing in the function or if we can perform canonical transformations in order to diminish the degrees of freedom of the problem. For example, since for Callisto we considered secular terms only, λ_4 is surely missing from the Hamiltonian.

We make a change of variables in order to pass to slow variables: from the Delaunay variables to a set of resonant variables. We define a suitable linear generating function F:

$$\begin{aligned} F(\mathbf{q},\mathbf{P}) =&(2\lambda_2-\lambda_1-\varpi_1)\Sigma_1+(2\lambda_2-\lambda_1-\varpi_2)\Sigma_2\\ &+(2\lambda_3-\lambda_2-\varpi_3)\Sigma_3-\varpi_4\Sigma_4\\ &+(2\lambda_2-\lambda_1-\Omega_1)\Xi_1+(2\lambda_2-\lambda_1-\Omega_2)\Xi_2\\ &+(2\lambda_3-\lambda_2-\Omega_3)\Xi_3-\Omega_4\Xi_4\\ &+(\lambda_1-3\lambda_2+2\lambda_3)\Gamma_1+(\lambda_2-2\lambda_3)\Gamma_2\\ &+\lambda_3\Gamma_3+\lambda_4\Gamma_4 \end{aligned}$$

The new angle variables can be obtained by $\mathbf{Q}=\partial F/\partial\mathbf{P}$:

$$\begin{aligned} \sigma_1&=2\lambda_2-\lambda_1-\varpi_1, & \sigma_2&=2\lambda_2-\lambda_1-\varpi_2,\\ \sigma_3&=2\lambda_3-\lambda_2-\varpi_3, & \sigma_4&=-\varpi_4,\\ \xi_1&=2\lambda_2-\lambda_1-\Omega_1, & \xi_2&=2\lambda_2-\lambda_1-\Omega_2,\\ \xi_3&=2\lambda_3-\lambda_2-\Omega_3, & \xi_4&=-\Omega_4,\\ \gamma_1&=\lambda_1-3\lambda_2+2\lambda_3, & \gamma_2&=\lambda_2-2\lambda_3,\\ \gamma_3&=\lambda_3, & \gamma_4&=\lambda_4. \end{aligned}$$

As described in Chapter 2, the new momenta Σ_i, Ξ_i e Γ_i (with $i=1,4$) are defined by $\mathbf{p}=\partial F/\partial\mathbf{q}$,

$$\begin{aligned} &\Sigma_i=G_i, \qquad \Xi_i=H_i, \qquad i=1,4\\ &\Gamma_1=L_1+G_1+G_2+H_1+H_2,\\ &\Gamma_2=3L_1+L_2+G_1+G_2+G_3+H_1+H_2+H_3,\\ &\Gamma_3=4L_1+2L_2+L_3,\\ &\Gamma_4=L_4. \end{aligned}$$

The coordinates γ_3 and γ_4 are missing in the new Hamiltonian, and consequently the momenta Γ_3 and Γ_4 are constant. After the transformation, the dimension of the problem decreases to 20. Moreover, all the angle variables are slow

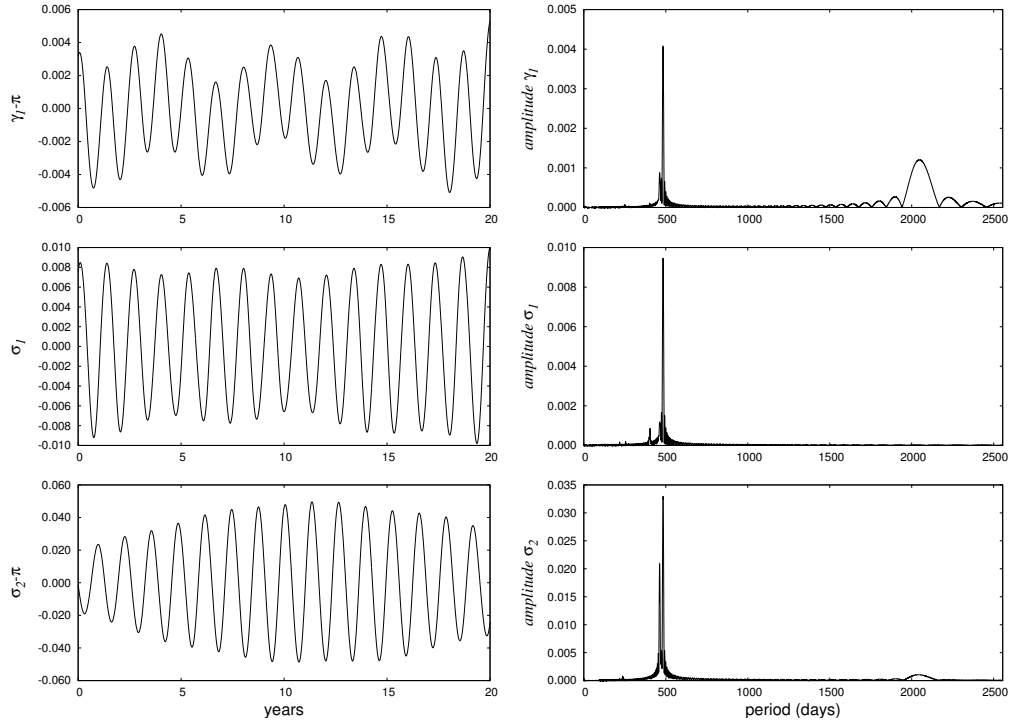

Figure 3.1.: *The three resonant angles γ_1, σ_1 and σ_2 (radians, left) and their spectrum (right) from the propagation of the semi-analytical model. The angles γ_1 and σ_2 are shifted of π radians in order to make clear the amplitude of their libration.*

with respect to the orbital periods, as they contain resonant combinations. We will see that their periods of circulation or libration are over one year.

In order to simplify the Hamiltonian, we pass to rectangular variables: the new momenta are x_i (respectively u_i) and the coordinates y_i (v_i), which are defined as follows

$$x_i = \sqrt{2\Sigma_i}\cos(\sigma_i), \qquad y_i = \sqrt{2\Sigma_i}\sin(\sigma_i),$$
$$u_i = \sqrt{2\Xi_i}\cos(\xi_i), \qquad v_i = \sqrt{2\Xi_i}\sin(\xi_i).$$

We do not change instead the variables Γ_i e γ_i. They are very similar to the rectangular coordinates defined in Chapter 2, for this reason we used the same notation.

In this way we treat polynomials of x_i and y_i (respectively u_i and v_i), instead of $\cos(\sigma_i)$ and $\sin(\sigma_i)$ (respectively $\cos(\xi_i)$ and $\sin(\xi_i)$). The entire writing of the Hamiltonian in terms of these variables is reported in Appendix A.

3.4 INITIAL CONDITIONS

The ephemerides, for example the ones of the JPL (last release JUP310) or IMCCE (last release L3), provide the instantaneous positions and velocities of the bodies for a time span of almost 100 years. From these tables we get the Galilean satellites' osculating elements, which suffer the whole dynamics, short period effects too. Therefore, we cannot use them as initial conditions for our semi-secular model, since it contains the resonant and secular dynamics only. If we used osculating elements as initial conditions, we could get values very distant from the mean elements, compromising the propagation.

A possible solution is to filter the osculating elements, in order to remove the short period terms from the numerical output. For this task we have to use a filter that kills the high frequencies, called low pass filter. We will describe the operation of filtering in the next chapter, when we will compare the results of the semi-analytical model with the ones of the ephemerides.

3.5 PROPAGATION

From the Hamiltonian, we can calculate the Hamilton's equations. Since the function comprehends a large number of terms, we use a symbolic manipulation software in order to avoid undesired errors.

For the propagation we use an implicit three-stages Runge-Kutta-Gauss method, which is a symplectic integrator. This property is very important, as it ensures to remain in a Hamiltonian context. In fact, each pass of the integration is a canonical transformation, where the new elements are the new variables of the Hamiltonian (which is invariant). Since we passed to a slow dynamics, we can use a larger time step for the integration: for our simulations we chose a pass of 2 days, which is small enough to obtain accurate results.

As stated in the previous section, we take the initial conditions from the filtering of the numerical output and we perform a 100 years integration. In this section and in the next chapter we present the results we obtain for the semi-major axes, the eccentricities, the inclinations and the resonant angles.

We start with the last ones: in Figure 3.1 we reported the evolution of γ_1, σ_1 and σ_2 and at their side the corresponding spectrum. In order to highlight the libration periods we limited the time interval to 20 years. Apart from the common period of 486.89 days, which is the period related to (2.17) and we can identify with the period of circulation of γ_2, each resonant angle has its proper frequency, which is related to its libration. For σ_1 we found a period of almost 403.82 days, for σ_2 almost 462.45 days and for γ_1 almost 2047.85 days. These values are in good agreement with the ones published in previous studies, in particular from [22] they are respectively 486.81, 403.52, 462.51 and 2059.62.

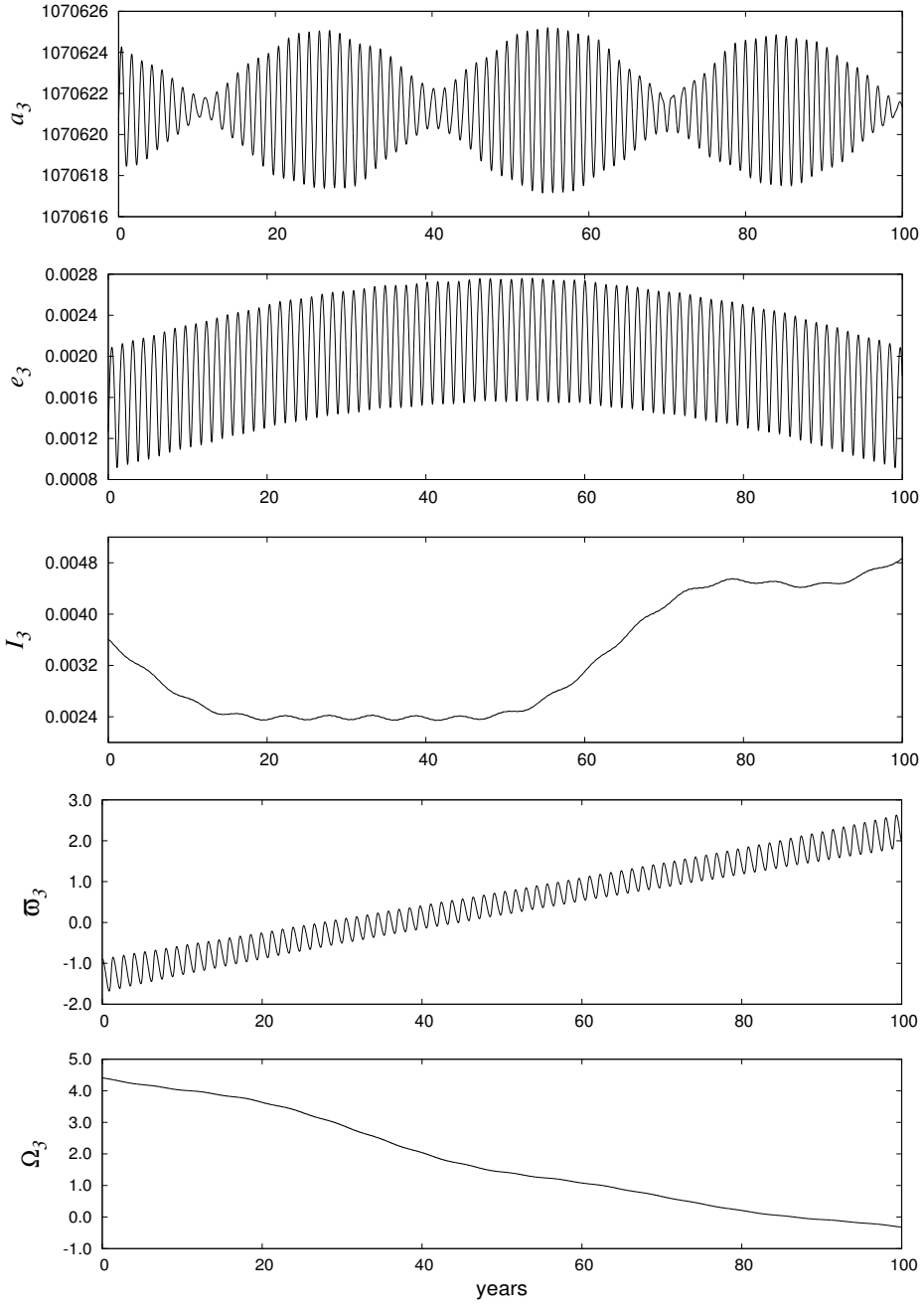

Figure 3.2.: *In order from the top, the Ganymede's semi-major axis (km), eccentricity, inclination, longitude of the pericenter and longitude of the node (radians).*

In Figure 3.2 we report some elements of Ganymede as examples, although in Chapter 4 we will show the output of the orbital elements of all the satellites for the comparison with the ephemerides. We give a short description of the series, using the explicit expression present in the Hamiltonian

- The mean semi-major axis oscillates with an amplitude of almost 3 km, that is far smaller than the amplitude of the corresponding osculating element, which is greater than 150 km. In its spectrum only resonant frequencies are evident: the main feature is the beat between the two resonant frequencies related to σ_2 and γ_2.

- The eccentricity has both resonant and secular signals in its spectrum. In the figure it is dominant a hump, which is the sign of an effect with a period longer than 100 years. With the semi-analytical model it is easy to prove that it is due to the term $e_3 e_4 \cos(\varpi_4 - \varpi_3)$ of the mutual perturbation with Callisto. In fact, using a longer propagation, we calculated the period of the signal, which is 181.5 years. This period is very close to the computed value for the circulation of $\varpi_4 - \varpi_3$ (almost 182.2 years).

- The inclination has a main term with a secular period of almost 137 years, which is the period of circulation of Ω_3, given mainly by the perturbation of J_2. Moreover, also the contribution of the Sun is very important, though as an indirect effect, as we will explain in Chapter 4.

- The longitude of the pericenter has a linear rate of 4.62×10^{-2} rad/year, which does not verify the condition of the de Sitter resonance. This value is given mainly by the effect of J_2; however, because of the proximity to the resonance, we find evident oscillations with the period of γ_2.

- The longitude of the node has a linear rate of -4.59×10^{-2} rad/day, given mainly by the effect of J_2, which influences the evolution of the inclination. The decreasing of the angle is not perfectly linear, but there is an evident oscillation given mainly by the term $s_2 s_3 \cos(\Omega_3 - \Omega_2)$ of the perturbation with Europa.

With the short analysis above, we showed the strength of the semi-analytical model. Performing a frequency analysis, we manage to describe and to understand the main aspects of the motion. All the frequencies in the output can be explained looking at the single terms written explicitly into the Hamiltonian.

The analysis made for Ganymede can be replied for all the other moons. In this section we chose Ganymede as example, since both resonant and secular features are clear in the series of Figure 3.2. In Chapter 4 we will give a brief description of the orbital elements of all the moons.

4 COMPARISON WITH NUMERICAL MODELS

In order to validate the semi-analytical model, we compare the results of its propagation with the ephemerides of the moons. We choose the JUP310 ephemerides of the JPL, which cover the time span between 1900 and 2100. In particular, we will present the results of a 100 years propagation of our model, including the filtered series of the ephemerides in the same figures, in order to show the good level of accuracy we reached. For a validation on longer time scales we can use some works present in the literature. For example, in [35] the authors developed a numerical model for long propagation of the Galilean satellites, while in [22] the authors presented a synthetic representation of the moons' motion, providing Fourier series for all the orbital elements. In this chapter we will compare the amplitudes and the frequencies of the main terms of these series with the output of a long-term propagation of the semi-analytical model.

As we stated for the initial conditions' choice, also for the comparison with numerical models, it is necessary to eliminate the short period effects present in their output. This is possible thanks to a low pass filter for the ephemerides, while for the synthetic representation of [22] we need just to remove the short period terms from the series.

4.1 DIGITAL FILTERING

We can recover digitally the secular dynamics from a numerical model's integration. We must apply a filter that kills the high frequencies from the output. In this section we describe the digital filtering following [3], to which we refer for more details.

A filter is a process that acts on the spectrum of the frequencies; a low pass filter d is a filter that passes the band of frequencies lower than a certain cut-off frequency f_c, while it removes those higher. It can be represented as a function that has value 1 for $f < f_c$ and 0 for $f > f_c$. The result of the filtering on a sequence $(x_k)_{k=1}^n$ is a new series $(y_k)_{k=1}^n$ obtained by a convolution

$$y_m = (x * d)_m = \sum_{k=-M}^{M} d_k x_{m-k},$$

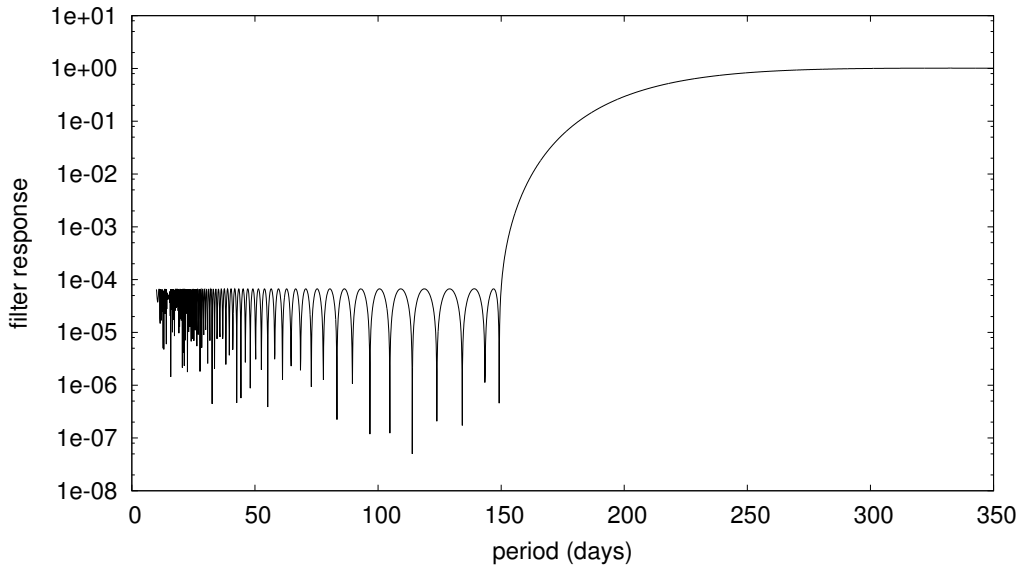

Figure 4.1.: *Response of the filter we used for filtering the numerical output. In the* x*-axis it is reported the period* T *and not the frequency* f *(they are inversely proportional* $T = 2\pi/f$*). The pass band is almost* 300 *days: the signals with period below* 150 *years are removed, while the band between* 150 *and* 300 *is damped by a factor between* 0 *and* 1*. The choice of the pass band is appropriate to preserve the resonant periods, which are greater than* 400 *days.*

where m indicates a generic element of the series, M is the length of the filter and d_k its elements.

In order to have an analytical filter, we cannot hope to have a response identically equal to 0 or 1, but we must have a behaviour like the one shown in Figure 4.1. The frequencies we want to eliminate are multiplied for numbers near 0 (less than 10^{-4}), while the ones greater than f_c remain almost unchanged. In the middle there is a small band for which the filter takes values between 0 and 1. The response in frequency is

$$\hat{d}(f) = \sum_{k=-M}^{M} d_k \exp(-ikfT_s),$$

where i is the imaginary unit and T_s is the period of sampling of the series we are going to filter.

Short periods and secular periods are very distant one from each others, then it is possible to choose a suitable filter that removes the high frequencies without ruining the low frequency signal. However, it is possible that some intermediate frequencies are touched by the filter; in our case, since we want to keep the resonant terms, we have to pay attention not to eliminate a band too large. As

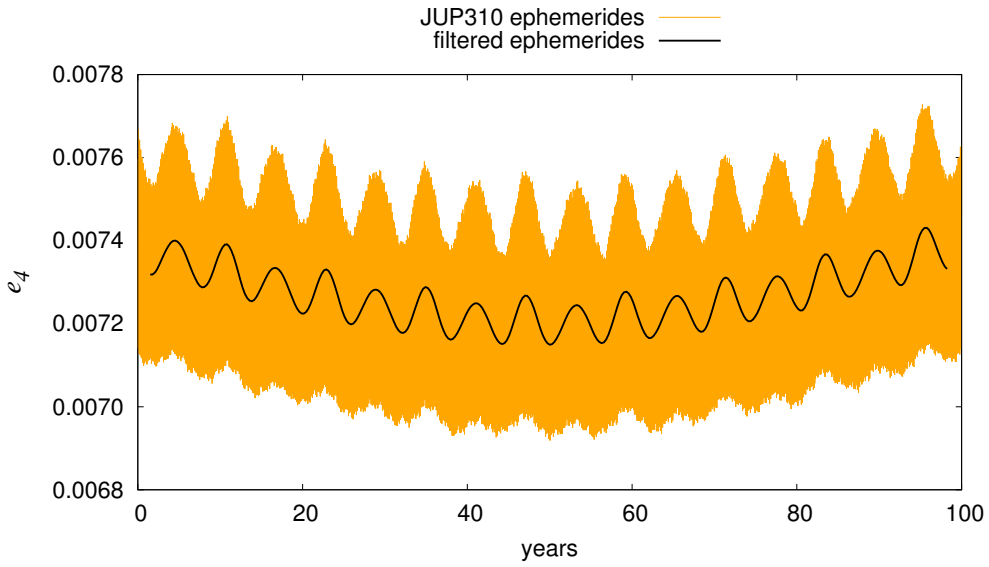

Figure 4.2.: *In orange the Callisto's eccentricity from the JPL ephemerides, in black the same output after the application of the digital filtering.*

we know the periods of the resonant angles, we can choose a suitable filter that preserve them.

In the following analysis, we will consider a time span of 100 years, that allows to fully show the resonant features of the dynamics, but also to recognize the secular dynamics. The low pass filter we use is chosen in order to eliminate periods below 150 days, as shown in Figure 4.1. In fact, we need to eliminate the signals up to 138 days, which is the maximum significant period we find in the numerical output and not in the semi-analytical model. The period of the first significant resonant signal is 255 days, which is almost at the end of the intermediate band; therefore, the signal is damped by a factor between 0.8 and 0.9. However, its contribution is quite limited and it will not affect the results.

In Figure 4.2 we reported an example of the filtering. In orange, we have the eccentricity of Callisto obtained directly from JUP310 ephemerides, therefore including also the short period effects. We applied a low pass filter in order to preserve the resonant and secular frequencies. The result of the filtering is shown in black: the wild high frequencies are removed from the numerical output, leaving a signal more clear and readable.

When we apply a low pass filter on a numerical output, such as the one of the JPL ephemerides, we smooth the signal. It is a sort of averaging, but performed *a posteriori*. We get new elements that are (or should be) almost equal to the mean elements we obtained with the semi-analytical resonant model, which builds on an averaging of the Hamiltonian. In the next section we will show a full comparison of the two models.

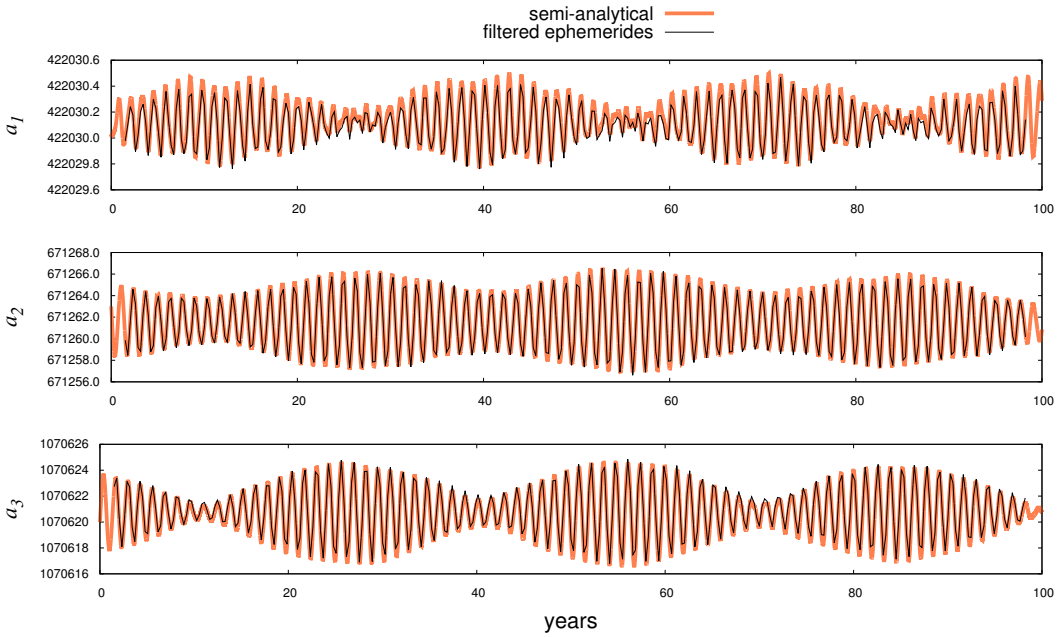

Figure 4.3.: *Galilean satellites' semi-major axes (km) over 100 years starting from J2000. In black we have the filtered elements taken from JUP310 ephemerides, while the thick coral line is the output of the semi-analytical model. We do not report the semi-axis of Callisto, since it is constant in the semi-secular model.*

4.2 MATCHING OF THE MODELS

The dimension of the resonant model is 20, and even if it would be interesting to show how good the comparison is for all the variables, there are elements that are more significant than others. We decided to report the semi-major axes of Io, Europa and Ganymede (Figure 4.3), the eccentricities of all the satellites (Figure 4.4), the inclinations of all the satellites (Figure 4.5) and the three independent resonant angles σ_1, σ_2 and γ_1 (Figure 4.6).

From a first look at the figures, we can appreciate how the semi-analytical model's output matches with the ephemerides. In particular Figure 4.6, shows that the resonant frequencies and amplitudes are captured almost perfectly. This

	$\dot{\omega}_1$	$\dot{\omega}_2$	$\dot{\omega}_3$	$\dot{\omega}_4$	$\dot{\Omega}_1$	$\dot{\Omega}_2$	$\dot{\Omega}_3$	$\dot{\Omega}_4$
S-A	-4.7102	-4.7102	0.0462	0.0117	-0.8407	-0.2086	-0.0459	*

Table 4.1.: Rates of change of the longitudes of the pericenters and of the nodes, computed from a 10000 years propagation. (*) For Ω_4 we did not find an evident linear rate, but an oscillation with a very long period of almost 580 years.

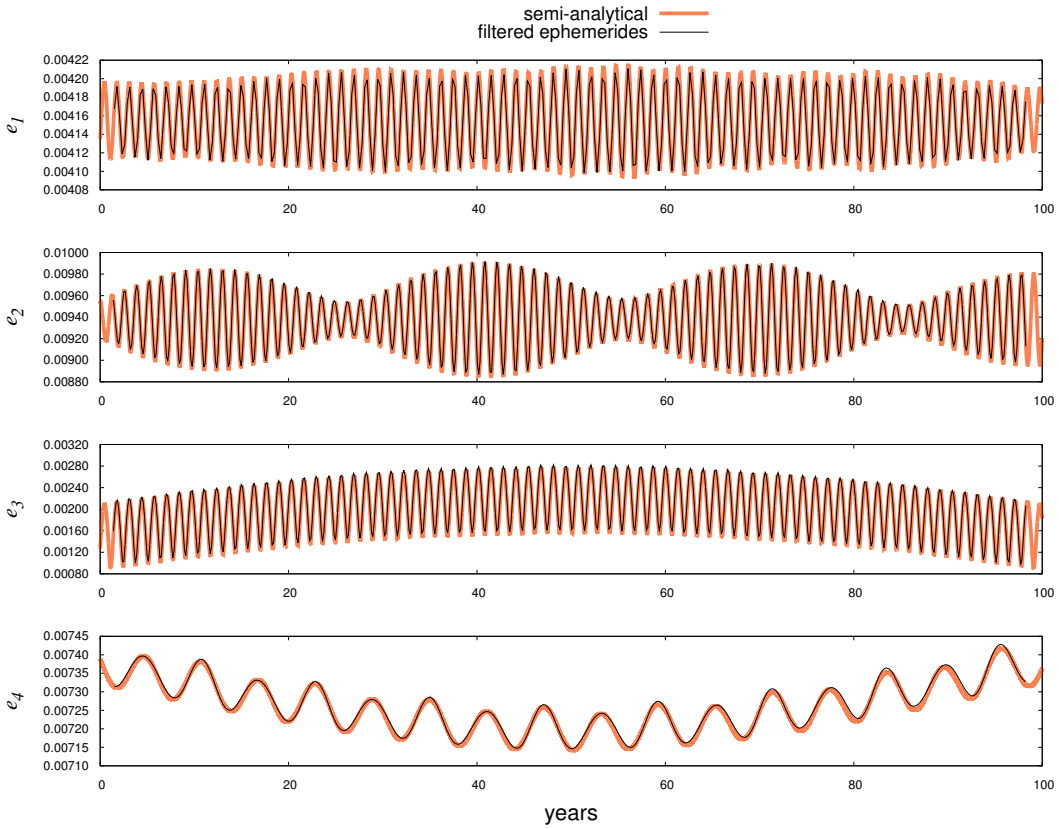

Figure 4.4.: *Galilean satellites' eccentricities over 100 years starting from J2000. In black we have the filtered elements taken from JUP310 ephemerides, while the thick coral line is the output of the semi-analytical model.*

allows not to get undesired signals in the output of the orbital elements. In fact, both eccentricities and semi-major axes, which suffer greatly the resonant effects, are well represented, with small differences due to the approximations of the model. Amongst the various resonant features, it is worth noting that the common signal in the semi-major axes and in the Europa's eccentricity is due to the beat of the resonant frequencies of σ_2 and γ_2.

Not only the resonant part, but also the secular dynamics is well represented by the semi-analytical model. The main secular features can be observed in the Ganymede and Callisto's eccentricities and all the inclinations. We give a brief description of all the elements reported in the figures and we try to explain all signals in the series, simply looking at the frequencies and at the Hamiltonian of the semi-analytical model.

We begin from the eccentricities of Figure 4.4. We know that, because of the resonances, $\dot{\varpi}_1$ and $\dot{\varpi}_2$ are equal to $-\nu$, whose period's scale is resonant. The longitudes of the pericenters of Io and Europa vary very fast, for this reason there

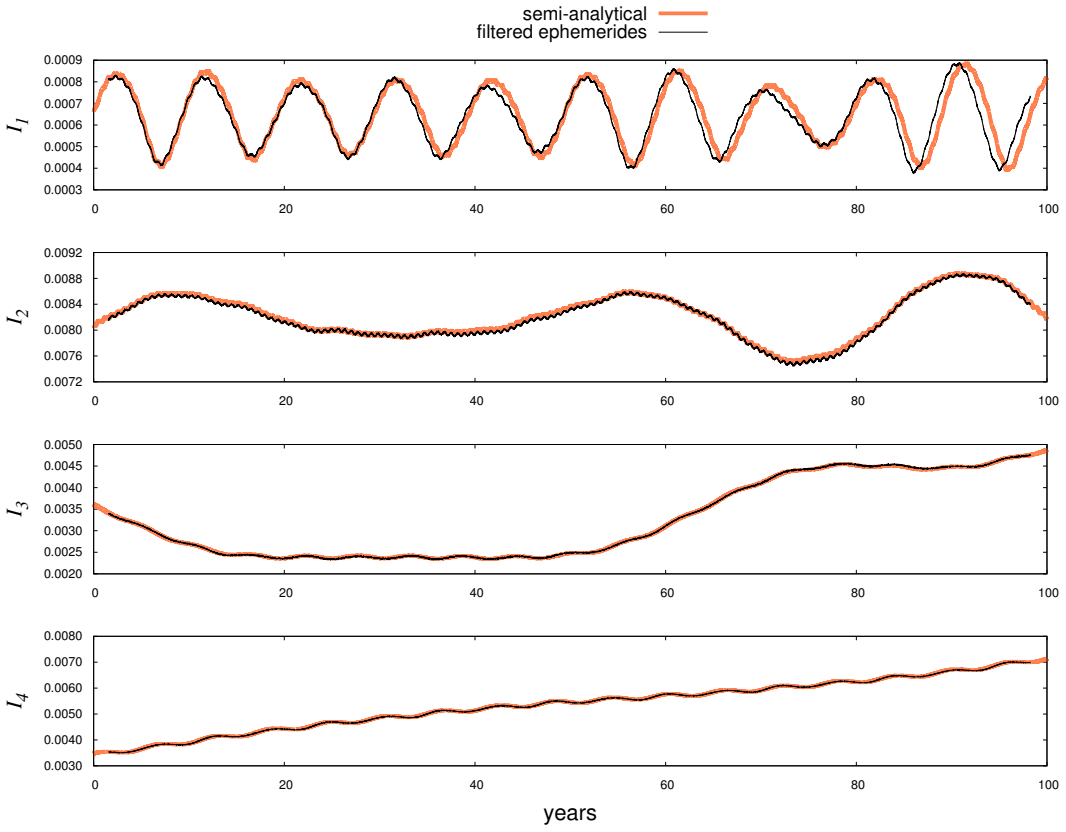

Figure 4.5.: *Galilean satellites' inclinations (radians) over 100 years starting from J2000. In black we have the filtered elements taken from JUP310 ephemerides, while the thick coral line is the output of the semi-analytical model.*

are not evident secular signals in the output of the two moons' eccentricity. While for Io the beat between the proper frequency of σ_1 and γ_2 is almost invisible because of the small amplitudes of the first, for Europa the beat between the proper frequency of σ_2 and γ_2 is the main feature. Instead, as described in Chapter 3, for the Ganymede's eccentricity we can see the hump due to the secular effects: the same behaviour can be found in the eccentricity of Callisto, with an apparent same period. This is due to the common term in the mutual perturbative function $e_3 e_4 \cos(\varpi_4 - \varpi_3)$, which produces an effect with a period of almost 181.5 that is the period of circulation of $\varpi_4 - \varpi_3$. Another clear signal is the one with period near 6 years in the Callisto's eccentricity: it is due to the term $e_4^2 \cos(2\lambda_s - 2\varpi_4)$ of the Sun's perturbation. In fact, the period is half the period of revolution of the star around Jupiter.

From Figure 4.5 we can see that in the inclinations, resonant signals are very weak. They are slightly visible just in the Io and Europa's inclinations, as very small oscillations. The main features are due to the secular periods of the circula-

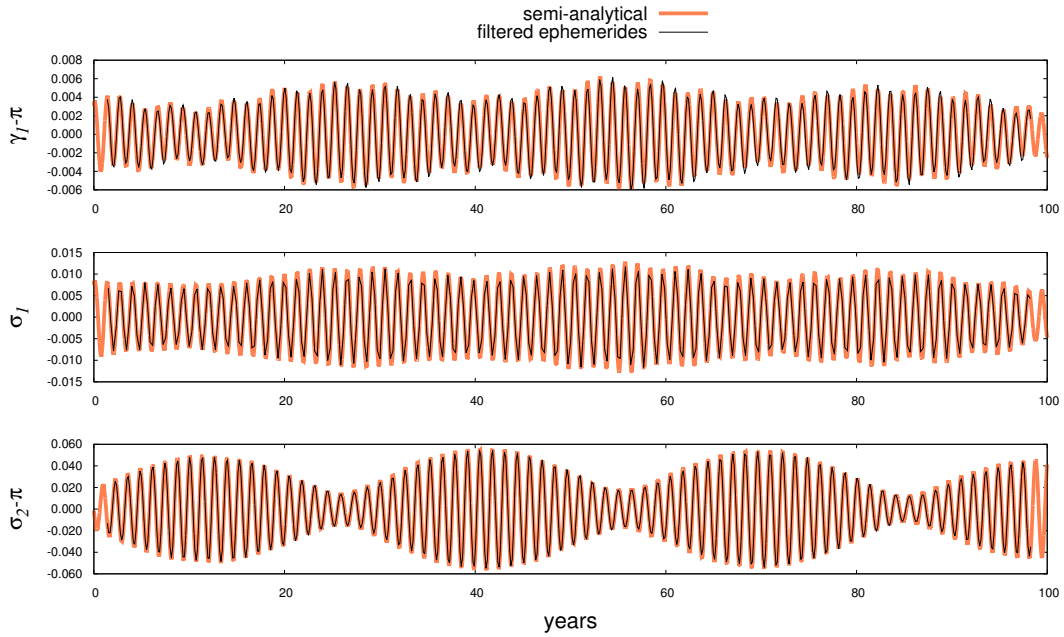

Figure 4.6.: *The three resonant angles γ_1, σ_1 and σ_2 (radians) over 100 years starting from J2000. In black we have the filtered elements taken from JUP310 ephemerides, while the thick coral line is the output of the semi-analytical model. The angles γ_1 and σ_2 are shifted of π radians in order to make clear the amplitude of their libration.*

tion of the longitudes of the nodes, whose rates are presented in Table 4.1. Since Io is the closest to Jupiter, the effect of J_2 is very strong and Ω_1 is pretty fast, with a period of circulation of almost 10 years, which is near the resonant scale. As shown in Table 4.2 there are two main secular signals in Europa's inclination: one has the period of circulation of Ω_2, while the other the period of circulation of $\Omega_3 - \Omega_2$. The last one comes out from the term $s_2 s_3 \cos(\Omega_3 - \Omega_2)$ of the perturbative function between Europa and Ganymede.

It is very interesting to investigate the effect of the Sun on the inclinations. The main effect is on the longitude of the node of Callisto: while we find it oscillating

	e_1	e_2	e_3	e_4	I_1	I_2	I_3	I_4
S-A	*	*	181.52	181.67	9.94	30.19/38.63	137.44	580.06

Table 4.2.: Secular periods of the main signals in the eccentricities and inclinations, computed from a 10000 years propagation. (*) We did not report any value for e_1 and e_2, since they are characterized by resonant effects mainly. For the inclination of Europa we have two values, since the contribution of the two signals is almost equivalent.

	z_1		z_2		z_3		z_4	
	amp	freq	amp	freq	amp	freq	amp	freq
S-A	1749	−0.0129030	6274	−0.0129030	1501	0.0001263	13874	0.0000320
	15	0.0001263	138	0.0001263	825	0.0000320	289	0.0001263
	8	0.0000320	123	0.0006766	634	−0.0129030	102	0.0028692
	3	0.0026554	80	0.0000320	8	−0.0259323	37	0.0000000
	2	0.0006766	10	−0.0259323	7	0.0006766	17	0.0014506
	1	−0.0264826	5	−0.0258381	5	0.0027750	2	0.0027750
[22]	1752	−0.0129069	6282	−0.0129069	1530	0.0001273	13889	0.0000321
	15	0.0001273	144	0.0001273	826	0.0000321	293	0.0001273
	8	0.0000321	133	0.0006777	634	−0.0129069	102	0.0028683
	6	0.0026643	81	0.0000321	7	−0.0259410	37	0.0000000
	2	0.0006777	9	−0.0259410	7	0.0006777	17	0.0014502
			5	−0.0258457	5	0.0027731	11	0.0043198*

Table 4.3.: Frequency analysis of the variables $z_i = e_i \exp(i\varpi)$. On the top we reported the six main frequencies and the corresponding amplitudes of the signals we found in a 10000 years propagation of the semi-secular model. On the bottom we did the same with the terms written in the series in [22]. The amplitudes are in km, as they are multiplied by the semi-major axis a_i. (*) Signals we did not find in our frequency analysis.

	ζ_1		ζ_2		ζ_3		ζ_4	
	amp	freq	amp	freq	amp	freq	amp	freq
S-A	132	−0.0023151	2736	−0.0005787	1734	−0.0001257	7246	0.0000000
	42	−0.0005787	158	−0.0001257	910	0.0000000	4171	−0.0000306
	8	0.0000000	114	0.0000000	368	−0.0000306	495	−0.0001257
	7	−0.0001257	40	−0.0000306	164	−0.0005787	63	0.0029012
	2	−0.0000306	8	−0.0023151	17	0.0029012	9	−0.0005787
	2	−0.0252274	8	−0.0252274	2	−0.0252274	6	0.0029318
[22]	133	−0.0023151	2712	−0.0005692	1706	−0.0001249	7235	0.0000000
	38	−0.0005692	147	−0.0001249	913	0.0000000	4228	−0.0000306
	7	0.0000000	111	0.0000000	376	−0.0000306	490	−0.0001249
	7	−0.0001249	39	−0.0000306	154	−0.0005692	63	0.0029004
	2	−0.0000306	7	−0.0023151	17	0.0029004	9	−0.0014500*
	2	−0.0252445	7	−0.0252445	3	−0.0014500*	9	−0.0005692

Table 4.4.: Frequency analysis of the variables $\zeta_i = \sin(I_i/2) \exp(i\Omega)$. On the top we reported the six main frequencies and the corresponding amplitudes of the signals we found in a 10000 years propagation of the semi-secular model. On the bottom we did the same with the terms written in the series in [22]. The amplitudes are in km, as they are multiplied by the semi-major axis a_i. (*) Signals we did not find in our frequency analysis.

with a period greater than 500 years, if we did not consider the Sun's perturbation, it would circulate with a rate of almost $-0.0097\ rad/year$. In this second case, the main signal on the inclinations of Ganymede and Callisto would have a period of almost 176 years, related to the circulation of $\Omega_4 - \Omega_3$, present in the term $s_3 s_4 \cos(\Omega_4 - \Omega_3)$ of the perturbative function. As shown in Table 4.2, it is far from the values we obtain with a more complete model. For this reason, a model without the Sun would get results on the inclinations very different from their actual behaviour.

In the semi-major axes we do not have apparent secular effects, as it is shown in the semi-analytical model. The main signal is due to the beat between the proper frequency of σ_2, which has the biggest amplitude amongst the resonant angles, and γ_2. In the semi-major axis of Io the contribution of γ_1 is slightly visible, while in the others it is completely hidden. In the semi-secular model the semi-major axis of Callisto is constant, as λ_4 is missing from the Hamiltonian and L_4 does not change.

For a long-term validation of our model, independent from the 100 years limitation of the ephemerides, we compare the signals we find in the eccentricities and inclinations output with the terms of the synthetic series presented in [22]. The results of the frequency analysis are shown in Table 4.3 and 4.4: all the amplitudes and frequencies are in good agreement with the results of the paper, from which we can easily recognize the source of the signals thanks to the identified linear combinations of the orbital angles reported in the article.

The semi-analytical model provides good results for all the orbital elements, that authorize to investigate new aspects of the dynamics. We can consider other significant effects that act on the system; in particular, we are interested in the tidal forces. In the next section, we will add their secular effects and we will study the evolution of the system.

4.3 TIDAL DISSIPATION

During the billions years of their lives, the satellites' orbits can change for several reasons. One of the possible causes is the energy dissipation due to the tidal forces. It is well known that it is for the tidal dissipation that the Moon looks at the Earth always with the same face, like the majority of satellites does with their planet. This configuration is called synchronous resonance and it is important to explain the dissipative effects on Io.

The tides are a differential force that acts on an extended body: in particular, the tidal force is defined as the difference between the gravitational force acting on a point minus the gravitational force acting on the center of mass. Since the force is not equal for all the points of the extended body, the tidal force is not trivial. We consider an extended body 0 and a point mass 1. The points of the face of 0 closer

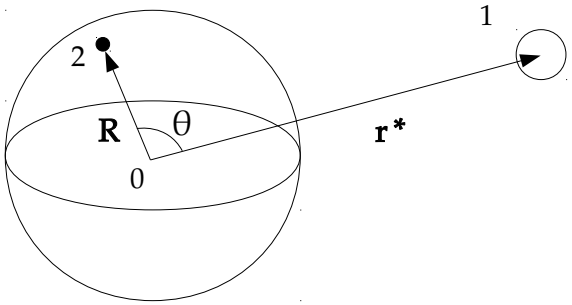

Figure 4.7.: *Representation of an extended body 0 that suffers the gravitational force of a point mass 1. With 2 we indicate a generic point of the first body.*

to the body 1 suffer a greater force than the ones on the far side. Moreover, also the direction of the force is different. This brings to a deformation of 0 along the line of conjunction between the centers of mass of the two bodies, forming two tidal bulges.

As shown in [19], in a reference frame centered in the deformed body, the potential associated with the tidal force is

$$W(\mathbf{R}, \mathbf{r}^*) = \frac{Gm}{r^*} \sum_{l=2}^{+\infty} \left(\frac{R}{r^*}\right)^l P_l(\cos\theta), \tag{4.1}$$

where $\mathbf{R}$ is the position of a point of the body 0, $\mathbf{r}^*$ is the position of the body 1 that raises the tides and θ is the angle between them (see Figure 4.7). The potential W is expanded in Legendre polynomials P_l and we indicate with W_l the l-th term of the series.

The deformation generates an additional field around the extended body, due to the displacement of the original mass (see [19]). Generally, it is supposed a linear response to the tidal potential (4.1):

$$U_l(\mathbf{r}, \mathbf{r}^*) = k_l \left(\frac{R}{r}\right)^{l+1} W_l(\mathbf{R}, \mathbf{r}^*), \tag{4.2}$$

with $\mathbf{r}$ the position of the external point where we calculate the induced potential U and $\mathbf{R}$ the point on the surface of 0 on the same line of $\mathbf{r}$. The parameters k_l are called Love numbers, and they quantify the deformation of the body, in particular, how much strong it is the response to W. Since the first term, $l = 2$, is the most important, in the next formulas we will consider just the effect of k_2.

As we consider real bodies, we cannot assume an immediate response to the tidal force (elastic tides). For a more realistic model we have to consider a time lag in the response of the body to the deformation. Geometrically, we have an angle of lag δ between the conjunction line of the two bodies and the direction of the tidal bulges, as represented in Figure 4.8. This angle is related to the parameter Q,

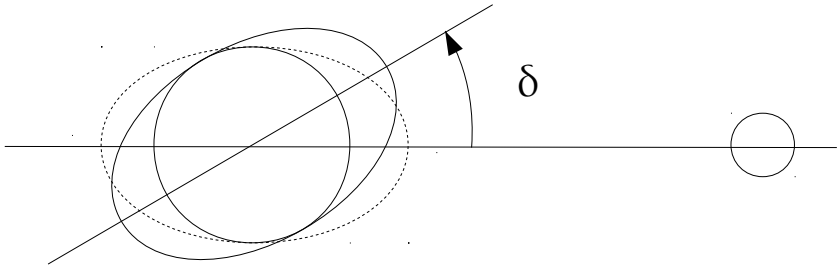

Figure 4.8.: *Anelastic tides; the tidal bulges are not aligned with the perturbing body (dash line), but they differ for an angle δ (continue line).*

called tidal quality factor, which describes the amount of energy dissipated during a tidal cycle

$$\frac{1}{Q} = \frac{1}{2\pi E_0} \oint -\left(\frac{dE}{dt}\right) dt.$$

In particular, for regular bodies, we have the following relation (see [9])

$$\frac{1}{Q} = \tan 2\delta \approx 2\delta.$$

There are two main secular effects we have to take into account, one due to the tides raised on the planet and the other one due to the tides raised on the satellite. In both cases we are considering the effect of the tides directly on the body that generates them; therefore, in (4.2), we take $\mathbf{r} = \mathbf{r}^*$

The tides that a satellite raises on the planet do not lie perfectly on the conjunction line between the two bodies, but they are dragged or slowed by the rotation of the planet. In the case of Jupiter and Io, the spin of the planet is faster than the mean motion of the moon, therefore, the tidal bulges are pushed ahead, forming an angle of lag. As shown in Figure 4.9, the satellite acts a torque τ on the two tidal bulges, which slows the spin of the planet:

$$\tau = -\frac{3}{2}\frac{k_2}{Q}\frac{G m^2 R^5}{a^6},$$

where k_2, Q and R are the Love number, the tidal quality factor and the radius of the planet, while m and a are the mass and the semi-major axis of the moon. For the conservation of the total angular momentum, the satellite must change its angular momentum $J = m\sqrt{G(m_0 + m)a(1 - e^2)}$ of the same quantity, but with the opposite sign. The variation of the semi-major axis is

$$\frac{1}{a}\frac{da}{dt} = \frac{2}{J}\frac{dJ}{dt} = -\frac{2}{J}\tau,$$

therefore, the body moves away from its planet and decelerates.

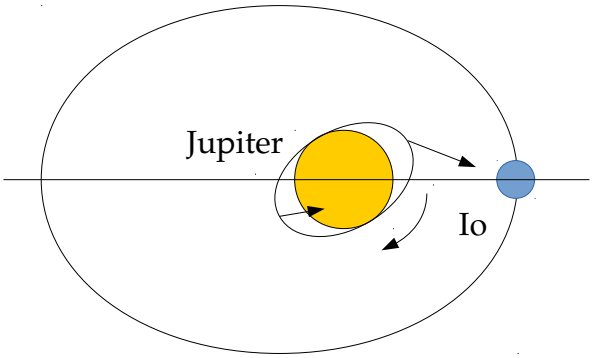

Figure 4.9.: *Tides on Jupiter. Because of the anelastic tides, the force that Io acts on the tidal bulges generate a torque which slows the spin of the planet.*

Also the tides that a planet raises on one of its moon change the orbit of the satellite. If we have a satellite in synchronous resonance with an eccentricity different from zero, such as Io, it happens that the point of maximum tides moves both radially and transversally on the surface, as shown in Figure 4.10. In fact, the distance of the moon from the planet is not constant, and then tides' height changes during a whole orbit (radial tides). Moreover, the moon looks, as a first approximation, at the empty focus during its rotation, so that the maximum tides oscillate around a fixed point on the surface of the moon (librational tides). In [38], the authors showed how this continuous compression produces energy dissipation within the body, stealing energy $E = -Gm_0m/(2a)$ from the moon's orbit.

$$\frac{dE}{dt} = -\frac{21}{2}\frac{k_2}{Q}\frac{Gm_0^2 n R^5 e^2}{a^6},$$

where k_2, Q, R, n, e and a are the Love number, the tidal quality factor, the radius, the mean motion, the eccentricity and the semi-major axis of the satellite.

In this case, the semi-major axis tends to decrease

$$\frac{1}{a}\frac{da}{dt} = -\frac{1}{E}\frac{dE}{dt}$$

and consequently the satellite accelerates along its orbit. Moreover, since only the energy is dissipated, but the angular momentum must remain constant, we have also an effect on the eccentricity

$$\frac{de}{dt} = \frac{1}{2e}\frac{1}{a}\frac{da}{dt}.$$

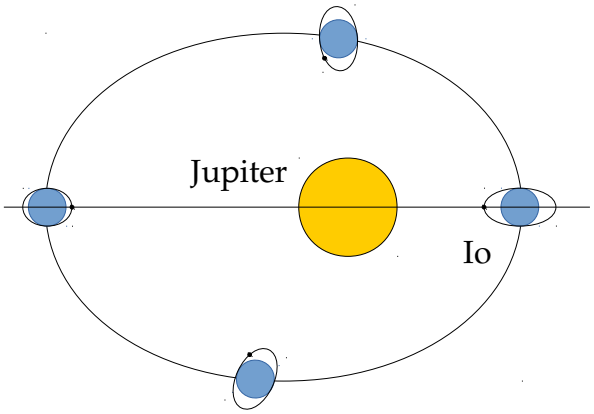

Figure 4.10.: *Tides on Io. We emphasized the radial tides (change in the height) and the librational tides (libration around the black point).*

In order to include these two effects into our model, we add the dissipative terms into the differential equations of the semi-major axis and the eccentricity of Io. Following the notation of [28] and [50], we write

$$\frac{da_1}{dt} = \frac{2}{3}c(1 - 7De_1^2)a_1, \tag{4.3}$$

$$\frac{de_1}{dt} = -\frac{7}{3}cDe_1; \tag{4.4}$$

where the coefficients c and D are

$$D = \frac{k_2^1}{k_2^0}\left(\frac{R_1}{R_0}\right)^5\left(\frac{m_0}{m_1}\right)^2\frac{Q^0}{Q^1},$$

$$c = \frac{9}{2}\frac{k_2^0}{Q^0}\frac{m_1}{M_0}\left(\frac{R_0}{a_1}\right)^5 n_1.$$

In the formulas above the superscripts of k_2 and Q indicate if they are referred to Io or Jupiter. In (4.3) and (4.4) the terms with cD are related to the dissipation in Io, while the terms with c alone are due to the tides on Jupiter.

We can translate the differential equations (4.3) and (4.4) in differential equations for the modified Delaunay momenta L_1 and G_1:

$$\dot{G}_1 = -\frac{14}{3}cDG_1,$$

$$\dot{L}_1 = \frac{1}{3}cL_1 - \frac{14}{3}cDG_1.$$

For the new momenta Γ_i $(i = 1, 3)$ and Σ_1, we have:

$$\begin{aligned}
\dot{\Sigma}_1 &= \dot{G}_1, \\
\dot{\Gamma}_1 &= \dot{L}_1 + \dot{G}_1, \\
\dot{\Gamma}_2 &= 3\dot{L}_1 + \dot{G}_1, \\
\dot{\Gamma}_3 &= 4\dot{L}_1.
\end{aligned}$$

Although we are considering a dissipation, i.e. a non conservative effect, we continue to use Hamilton's equations, as the tides are smaller than the other forces in the system. At the end of the propagation we can check if the amount of dissipated energy coincides with the variation of the Hamiltonian (which contains the orbital energy of the moons).

It is well known that resonant interaction spreads the dissipation in the system (see for example [34], Chapters 4 and 8, and [50]), affecting also Europa and Ganymede's orbits. We can perform a test with our semi-analytical model in order to check how well it describes this aspect of the dynamics.

For the dissipative parameters k_2^1/Q^1 and k_2^0/Q^0, we consider the values reported in [24], which are 0.015 and 1.102×10^{-5} respectively.

The results we obtained as variation in the mean motions over mean motions (unit 10^{-10} $rad/year$) are

$$\frac{\dot{n}_1}{n_1} = 0.355, \qquad \frac{\dot{n}_2}{n_2} = -0.303, \qquad \frac{\dot{n}_3}{n_3} = -1.626 \tag{4.5}$$

In Figure 4.11 we reported the difference in the semi-major axis between a simulation with dissipation and another one without dissipation. After a filtering operation, it remains a linear term in the semi-major axes of the three Galilean satellites; over 100 years they change few meters and the effect on the position along the orbit is approximated by

$$S_i = \frac{1}{2}\frac{dn_i}{dt}(t - t_0)^2 a_i.$$

It is worth noting that the effect is quadratic in time; although it appears as a small effect in the short time, if we consider a time span large enough, it will be detectable by the observations of the moons. In particular, after 100 years Io is 93 km ahead along its orbit, Europa 65 km and Ganymede 277 km behind. In [24] the dissipative parameters were estimated considering almost 100 years of astrometric observations. In 4 years, almost the nominal duration of the JUICE mission, the shifts are of the order of hundreds of meters, with the maximum effect of almost 500 meters on Ganymede. This estimation is very important for the second part of this thesis, where we investigate the possible determination of the dissipative parameters from JUICE data.

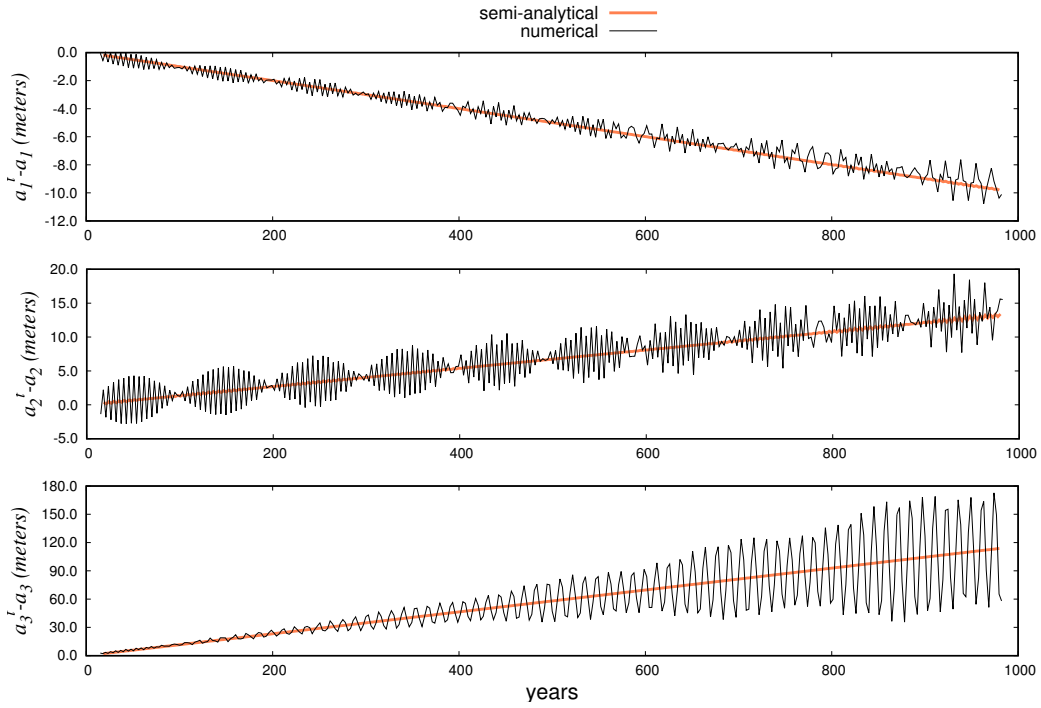

Figure 4.11.: *Effect of the tidal dissipation on the Galilean satellites orbits over* 1000 *years integration. We reported the filtered difference in the semi-major axis between a simulation with dissipation and another one without dissipation. We chose a time interval of* 1000 *years, instead of* 100*, in order to make the tidal effects clearer.*

In order to validate the results we obtained, we add the dissipative effects to a numerical model containing the same effects of the semi-secular one, considering the force $\mathbf{F}$ that a body undergoes by the tides it raises on another body. The formulation we use is taken from [29], which considers a lag in the position of the first body in order to take into account the dissipation, and it is often used for the investigation of the tidal evolution (see [9], [23] and [24]):

$$\mathbf{F} = -3\frac{k_2 G m^2 R^5}{r^7}\Delta t\left(2\frac{\mathbf{r}}{r}\frac{\mathbf{r}\cdot\mathbf{v}}{r^2} + \frac{\mathbf{r}\times\boldsymbol{\omega}+\mathbf{v}}{r}\right), \tag{4.6}$$

where m, $\mathbf{r}$ and $\mathbf{v}$ are the mass, position and velocity of the body that raises the tides, while k_2, R and $\boldsymbol{\omega}$ are the Love number, radius and angular velocity of the other body. The factor Δt is the time lag and it contains the quality factor Q of the deformed body,

$$\Delta t = \frac{T}{2\pi}\arctan\left(\frac{1}{Q}\right) \approx \frac{T}{2\pi}\frac{1}{Q},$$

where T is the period of one tidal cycle. Following [24] and denoting with n the mean motion of the satellite, in the case of tides on the planet $T = 2\pi/(2(|\boldsymbol{\omega}| - n))$,

which is the time that the moon takes to pass from a point over the planet's surface to its antipode, so that the tidal deformation comes back to its initial configuration. Instead, for tides acting on a synchronous satellite $T = 2\pi/n$, which is the time that the tidal deformation takes to complete a whole libration.

While for Jupiter we can consider a constant spin rotation, we cannot do the same for Io, as we supposed a synchronous resonance. In [34], Chapter 4, the authors expanded the tidal potential acting on a satellite locked in this kind of resonance and obtained two main terms, one due to the radial oscillation of the tides and the other due to the librational tides. Assuming that the satellites' Q is constant, the two tidal oscillations are linear and their contribution can be calculated separately. They computed the work related to the tidal deformation for both the terms and they found that the energy dissipated by the librational tides is exactly $4/3$ times the one of the radial tides. Therefore, for Io we adopt the following approach: first we evaluate the dissipation due to the radial tides considering $\boldsymbol{\omega} = \mathbf{r} \times \mathbf{v}/r^2$,

$$\begin{aligned}
\mathbf{F} &= -3\frac{k_2 G m^2 R^5}{r^7}\Delta t\left(2\frac{\mathbf{r}}{r}\frac{\mathbf{r}\cdot\mathbf{v}}{r^2} + \frac{1}{r}\left(\mathbf{r}\times\frac{\mathbf{r}\times\mathbf{v}}{r^2} + \mathbf{v}\right)\right) \\
&= -3\frac{k_2 G m^2 R^5}{r^7}\Delta t\left(2\frac{\mathbf{r}}{r}\frac{\mathbf{r}\cdot\mathbf{v}}{r^2} + \frac{1}{r}\left(\frac{\mathbf{r}\cdot(\mathbf{r}\cdot\mathbf{v}) - \mathbf{v}\cdot(\mathbf{r}\cdot\mathbf{r})}{r^2} + \mathbf{v}\right)\right) \\
&= -3\frac{k_2 G m^2 R^5}{r^7}\Delta t\left(3\frac{\mathbf{r}}{r}\frac{\mathbf{r}\cdot\mathbf{v}}{r^2}\right),
\end{aligned}$$

and then we add $4/3$ of their effect for taking into account the contribution of the librational tides. In the end we have a factor 7 inside the brackets, instead of 3

$$\mathbf{F} = -3\frac{k_2 G m^2 R^5}{r^7}\Delta t\left(7\frac{\mathbf{r}}{r}\frac{\mathbf{r}\cdot\mathbf{v}}{r^2}\right) \tag{4.7}$$

The values for the variation of the mean motions we obtain with the numerical model are close to the ones already presented for the semi-analytical model (see Figure 4.11)

$$\frac{\dot{n}_1}{n_1} = 0.343, \qquad \frac{\dot{n}_2}{n_2} = -0.306, \qquad \frac{\dot{n}_3}{n_3} = -1.629.$$

Although the qualitative behaviour is the same, the values we obtained are different from the ones published in [24], which are 0.14, -0.43 and -1.57 respectively. The possible reason for this disagreement can be a different model of Io's rotation. In our dynamical models we considered Io perfectly locked in synchronous resonance, but other models include physical or geometric librations, such as in [7]. In the next future, it could be interesting to test different models of the rotation of Io and to see how the orbital migration changes. However, it is worth noting that the knowledge on the internal structure of Io is quite limited, therefore, it is not

trivial to say which rotational model can better represent the actual rotation of the satellite. For what concerns our assumptions, the results are optimal, since in the same condition of synchronous rotation given by (4.7), we obtain almost the same values from both the semi-analytical model and the numerical one.

Finally, in order to quantify the current evolution of the system we check how the two-body resonances of the couples Io-Europa and Europa-Ganymede change. Nowadays, the value of the quantity ν defined in (2.17) is greater than 0. The variation of ν,

$$\dot{\nu} = \dot{n}_1 - 2\dot{n}_2 = \dot{n}_2 - 2\dot{n}_3,$$

indicates if the resonances are going deeper in their state ($\dot{\nu} < 0$), or they are evolving outward ($\dot{\nu} > 0$). With the values (4.5), we have $\dot{\nu} = 8.5 \times 10^{-8}\ rad/year^2$, which is close to 7.4×10^{-8} of [24]. This quantity allows in part to describe how the two 2:1 resonances varying, with a direct effect on the system (e.g. the value of the moons' forced eccentricities), but it does not describe the long-term evolution of the Laplace resonance, for which a dedicated investigation on longer time scales must be conducted.

These results depend on the values of the dissipative parameters k_2^1/Q^1 and k_2^0/Q^0. We chose the last ones published, in order to compare the accelerations we found with the ones of the paper. As we said, they were obtained from a fit of 100 years of astrometric observations; it is possible that with new observations, for example with the extremely precise data of the JUICE mission as we are going to investigate in the next part of the thesis, a new independent estimation of the parameters could describe a different evolution of the Laplace resonance.

Part II

ORBIT DETERMINATION WITH JUICE MISSION DATA

5 JUICE SPACE MISSION

In 2004, the European Space Agency (ESA) called for new astrophysics and space missions proposals to be launched between 2015 and 2025. The name of the programme is Cosmic Vision and it comprehends different classes of missions: S (small), M (medium) and L (large) classes. The most expensive and challenging projects are classified with an L. In 2007, the JUICE mission was one of the candidates for the first call of L-class missions and it was chosen in 2012.

The initial idea of the project came from another proposal, called EJSM/Laplace (Europa Jupiter System Mission), that was intended as a joint ESA and NASA mission. The collaboration stopped before the approval; while ESA is currently working on JUICE, NASA is developing a new project called Europa Clipper, devoted to an extensive observation of Europa through multiple flybys.

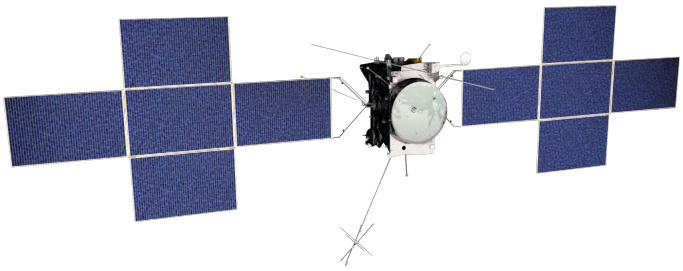

Figure 5.1.: *Model of the spacecraft, taken from ESA's website.*

The main task of JUICE is the exploration of the Galilean satellites of Jupiter. It will encounter Europa, Ganymede and Callisto, avoiding Io, because of the huge radiation in the regions closer to Jupiter, that could compromise the spacecraft's functionality. The mission comprehends both flybys of the moons and an orbiting phase around Ganymede. A flyby is a close approach to a satellite: the spacecraft's orbit around Jupiter is designed in such a way that the spacecraft's distance from the satellites can reach few thousands of kilometers. Some of the flybys are very low (few hundreds of kilometers from the surface), allowing to obtain pictures with a great resolution and very accurate data. In the case of a flyby, if we center our reference frame in the satellite, the orbit of the spacecraft is not elliptic, but

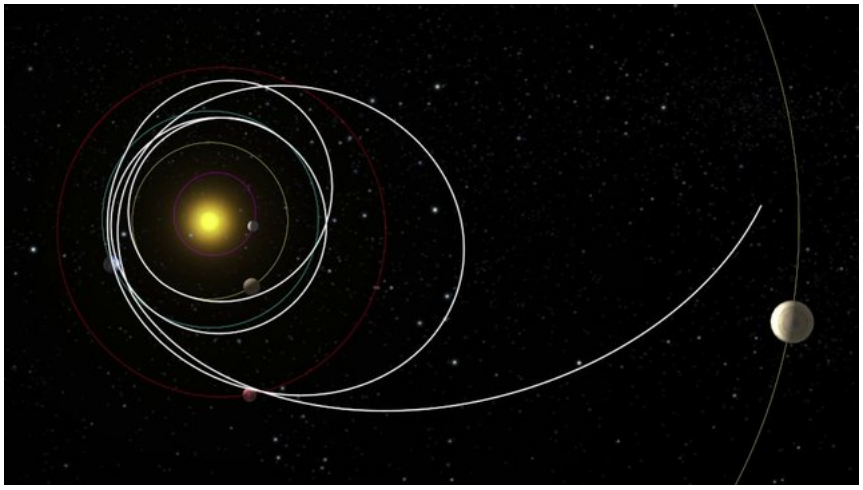

Figure 5.2.: *The interplanetary journey of JUICE, taken from ESA's website. The total time to arrive at the Jovian system will be over 8 years.*

hyperbolic, because of the huge velocity of the probe that makes the satellite-centric energy positive.

The description of all the instruments on-board the probe is not an aim of this thesis and more information can be found in [17], which is the official report of the mission. The objectives of the JUICE Science Team can be divided into two main topics.

- Explore the habitable zone: Ganymede, Europa and Callisto. It comprehends the study of the structure and the composition of the icy satellites.
- Explore the Jupiter system as archetype of gas giants. It comprehends the study of the composition and the atmosphere of Jupiter, but also the monitoring of Io's volcanic activity.

This part of the thesis is mainly related to the first point, although it cannot be completely separated to the second one. In fact, the observations and measurements of Io (for example of its heat flow) can help to understand better the energy dissipation within the little moon. We know that tidal friction is the source of energy that lets hope to find life on the satellites: liquid oceans can be preserved by the tidal heating within the moons. The Laplace resonance and the tidal forces could have played a synergic role to create the conditions for life. The amount of energy released in the satellites depends on the magnitude of the dissipative parameters; an improvement on their knowledge could provide new evidences about the history and the future of the system.

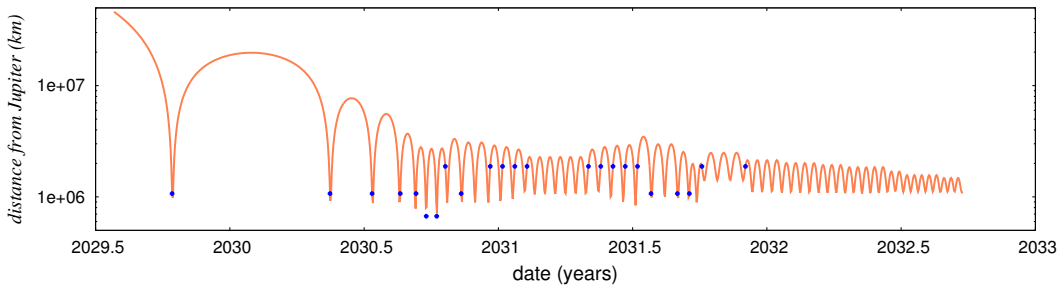

Figure 5.3.: *Distance of the spacecraft from Jupiter during the orbiting phase around the planet. Blue dots indicate the flybys: from their height it is possible to recognize the flybys of Europa (the two lower dots), the flybys of Callisto (the twelve higher dots) and the flybys of Ganymede (the remaining dots).*

5.1 OVERVIEW OF THE MISSION

According to the plan of the mission, the probe will be launched on June 2022. Before arriving at Jupiter, it will perform a series of gravity assists with some internal planets: the spacecraft will encounter the Earth (May 2023, September 2024 and November 2026), Venus (October 2023) and Mars (February 2025) in order to gain the necessary speed to reach the Jupiter's system without an excessive expense of fuel. The arrival at Jupiter is expected on October 2029.

The tour in the Jovian system we are going to describe is taken directly from the JUICE Spice Kernel

juice_mat_crema_3_2_20220601_20330626_v01.bsp,

which can be downloaded freely from the JUICE repository [18] in the ESA's website. It is worth noting that for the generation of this SPICE Kernel, the states of the Galilean satellites were taken from the L3 ephemerides of the IMCCE. Their denomination in the same repository is

noe-5-2017-gal-a-reduced.bsp,

and we used it for getting the initial conditions of the moons' propagation.

Once performed the manoeuvre of insertion into the Jupiter system (JOI), JUICE will orbit around Jupiter for almost three years. During this period, 23 flybys of the moons are scheduled. They will be the most important occasions to observe Europa and Callisto. In fact, after almost 900 days, the spacecraft will enter in orbit around Ganymede for a nine months orbiting phase.

The exact series of flybys is shown in Figure 5.3, where it is also plotted the spacecraft's distance from the planet. In particular, at the beginning of the sequence, we have five flybys of Ganymede (the first one before the JOI manoeuvre). Successively, the probe will encounter Europa two times, with a time gap of 15

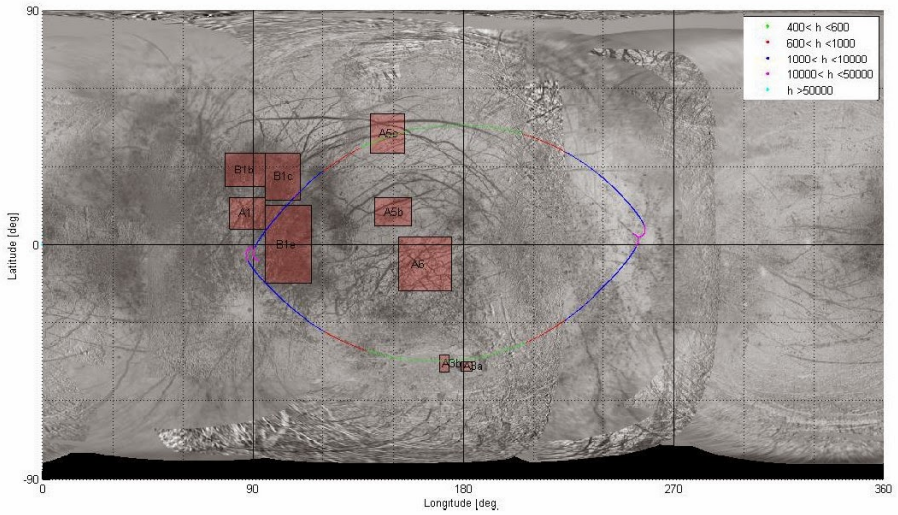

Figure 5.4.: *Tracks of the two flybys of Europa over the moon's surface, taken from [17]. The different colours indicate the altitude from the surface.*

days in the middle (see Figure 5.4). These will be the only opportunities to explore Europa directly, as the spacecraft will return to higher orbits.

After a flyby of Callisto and another one of Ganymede, a series of nine flybys of Callisto will allow to collect direct observations of the moon. However, since the spacecraft will encounter the satellite in the same point of Callisto's orbit and since the moon is in synchronous resonance with Jupiter, the explored surface will be limited as shown in Figure 5.5, not allowing to obtain global data of the satellite. Other three flybys of Ganymede and two flybys of Callisto will be the last close approaches to the moons.

Some months after the last flyby of Callisto, JUICE will leave the gas giant to enter in orbit around Ganymede. These last nine months of mission comprehend two phases: GEO/GCO5000, where the spacecraft will pass from an highly elliptic orbit to a central circular phase at 5000 kilometers of altitude and viceversa, and GCO500, where the spacecraft will stay in a circular orbit 500 kilometers from the surface.

It is clear that, because of the small quantity of flybys of Europa and the poor changes in the Callisto's flybys, Ganymede is the satellite for which the scientific return will be greater. This is taken into account in the requirements of the mission and we will follow them in our simulations.

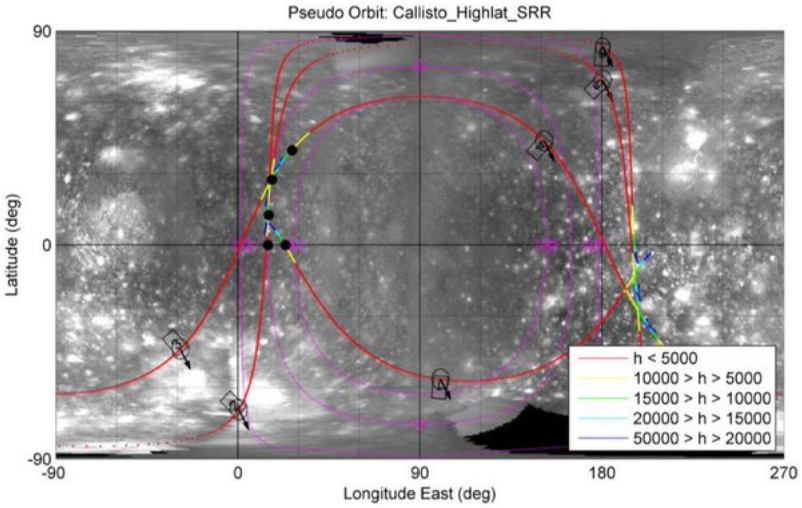

Figure 5.5.: *Tracks of some flybys of Callisto over the moon's surface, taken from [17]. The different colours indicate the altitude from the surface.*

5.2 FLYBYS

When the spacecraft performs a flyby of a moon, it can collect important data for the study of the body. Instruments like the laser altimeter provide data for the reconstruction of the topography, cameras collect pictures of the surface and so on. As we will see, tracking data provide important information for the gravitational model of the satellite and its internal structure, but overall we are interested in the dynamics of the moon. During each flyby, thanks to radioscience and VLBI observations, we get information about the orbit of the satellite the spacecraft is flybying; the collected observations are very important for determining the states of the Galilean satellites and for a future improvement of their ephemerides.

For each flyby we can introduce some parameters that describe its geometry, as shown in Figure 5.6. First, we consider the distance of the pericenter of the hyperbolic orbit from the target body's center of mass; if it is small, the observations will be more sensitive to the dynamical parameters of the Galilean satellite and they will contain more information.

Secondly, we need a parameter that describes how the spacecraft's orbit appears from the Earth; we define $\theta_G \in (0, 180°)$ as the angle between the direction W normal to the orbital plane and the direction passing from the Earth and the spacecraft (line of sight). If θ_G is near 90°, it means that from the Earth we see the spacecraft's orbit as a straight line (edge-on), while if the angle is near 0° or 180°, it means that the orbital plane looks perfectly toward the Earth (face-on). Both these configurations can be a disadvantage for the radioscience observations, but

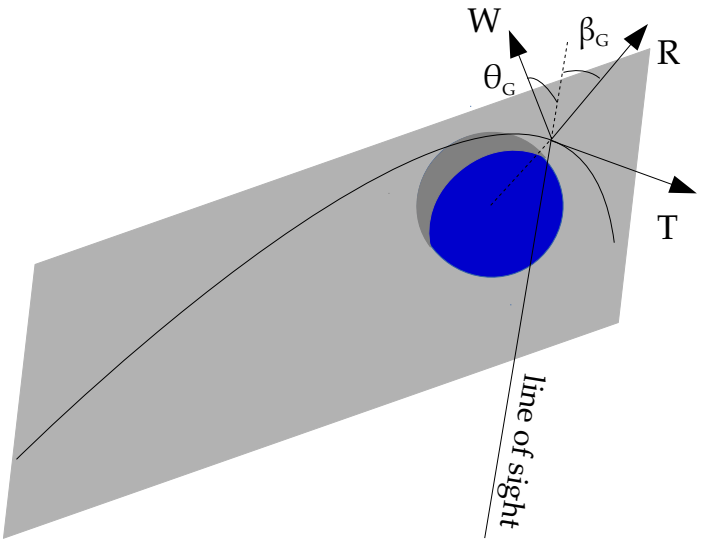

Figure 5.6.: *Representation of a flyby; the orbital plane is coloured by grey and it cuts the target body along the line that the spacecraft flies over. We reported the orbital reference frame* (R, T, W) *for a particular point of the hyperbolic orbit and we draw also the geometric angles formed with the line of sight.*

thanks to VLBI observations also in these cases it will be possible to obtain a good estimation of the parameters.

Another relevant geometric property is the position of the spacecraft with respect to the satellite, as seen from the Earth. In fact, the spacecraft can pass in front of or behind the target body; in the second case, the moon can cover the probe during the flyby (especially closer to the body), leading to a loss of information. We define β_G as the angle between the line of sight and the position vector R of the spacecraft with respect to the moon. If β_G is near $0°$, then the spacecraft passes behind the target moon, with a possible interruption of the tracking, while if it is near $180°$, the spacecraft is in front of the body and it is completely exposed toward the Earth.

In Table 5.1 we reported the values of these parameters, taken at the pericenter of the spacecraft's hyperbolic orbit. Since the radii of the Galilean satellites are between 1500 and 2700 km, we can appreciate how the spacecraft will pass close to their surface.

Looking at the table and at Figure 5.4, we can note that the two flybys of Europa are very similar: the geometric properties are almost equal, although, as we can see from the tracks on the Europa's surface and the values of θ_G, once the spacecraft will fly over the northern hemisphere, and the second time over the southern one.

Flyby	Day	Target Body	Distance (km)	θ_G (°)	β_G (°)
1	10-06-2029	Ganymede	3032	80	105
2	05-09-2030	Ganymede	3032	93	120
3	07-05-2030	Ganymede	4346	98	105
4	08-13-2030	Ganymede	3429	95	44
5	09-03-2030	Ganymede	3914	95	38
6	09-17-2030	Europa	1964	126	123
7	10-01-2030	Europa	1964	56	124
8	10-13-2030	Callisto	2822	92	13
9	11-03-2030	Ganymede	5217	149	101
10	12-13-2030	Callisto	2611	30	70
11	12-30-2030	Callisto	2609	20	74
12	01-15-2031	Callisto	2609	21	70
13	02-01-2031	Callisto	2609	55	35
14	04-25-2031	Callisto	2609	131	138
15	05-12-2031	Callisto	2609	167	103
16	05-29-2031	Callisto	3436	170	100
17	06-14-2031	Callisto	3966	172	97
18	07-01-2031	Callisto	2609	135	134
19	07-20-2031	Ganymede	13553	80	150
20	08-24-2031	Ganymede	12469	80	144
21	09-10-2031	Ganymede	5803	100	11
22	09-27-2031	Callisto	2609	92	41
23	11-25-2031	Callisto	5823	93	75

Table 5.1.: Geometric parameters of the flybys.

5.3 TRACKING AND VLBI DATA

The on-board instruments will allow to collect very different kinds of data. For the simulations we are going to perform, we are interested in two experiments: 3GM (Gravity and Geophysics of Jupiter and Galilean Moons) and PRIDE (Planetary Radio Interferometer and Doppler Experiment).

The first one is the radioscience experiment. Thanks to the transponder mounted on JUICE, it is possible to track the spacecraft from ground based stations. A radio signal in Ka-band (uplink 34.3 GHz) is sent from the station, it arrives at JUICE that remodulates and sends it back to the Earth (downlink 32.5 GHz). The time span between the signal's departure and arrival allow to obtain the distance of the spacecraft from the tracking ground station (range). Instead, the variation of frequency of the signal due to Doppler effect provides the variation of the range (range-rate). The estimated accuracy is 20 centimeters for the range and 3×10^{-4} centimeters per second for the range-rate (considering 2-way measurements).

A first study of the 3GM experiment's performances was presented in [37]. The main objective of the work was the estimation of the gravitational field of Ganymede and the state of the spacecraft. However, the simulations were limited

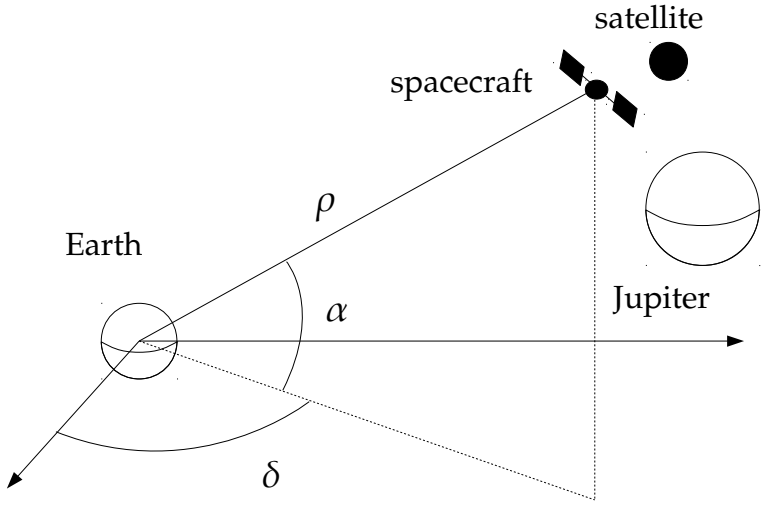

Figure 5.7.: *Representation of tracking and angular measurements. In particular,* $\rho = |\boldsymbol{\rho}|$ *is the range,* $\dot{\rho}$ *the range-rate,* α *the right ascension and* δ *the declination.*

to the Ganymede orbiting phase only. Since we are interested in effects that influence the moons's dynamics, such as the tidal dissipation, we need to take into account the flybys phase and to deal with more challenging aspects of the mission. For this reason we cannot limit our study to tracking data, but we have to include other data sets.

PRIDE experiment will provide VLBI (very-long-baseline interferometry) data. They consist in the measurements of the angular differences between the spacecraft and some known radar sources, such as quasars. In particular, it will be possible to measure the right ascension α and the declination δ of the spacecraft with respect to the Earth, as represented in Figure 5.7. Their accuracy is estimated to be 10^{-9} radians, with the possibility to reach 10^{-10} radians level using the Ka band (see [8]). In the first case, the linear accuracy at the Jovian system distance is few hundreds of meters, while, in the second one, few tens of meters. Considering the large available time for the improvement of the technique before JUICE will arrive at Jupiter, in our study we will consider the best performance for VLBI.

Apart from 3GM and PRIDE, also the cameras can contribute to our experiments. In fact, JANUS experiment comprehends two cameras that, in the windows of time far from their main tasks, can take pictures of the Galilean satellites. In suitable conditions, they can provide astrometric observations of the moons, as done in [47] for the Cassini space mission. They consist in direct angular measurements of the Galilean moons, whose accuracy, following [8], is set to 10^{-5} radians in our experiments. In the range of distances we consider, it corresponds to a linear accuracy of few kilometers.

Moreover, we will consider also direct astrometric observations of the moons from ground based stations. This kind of observations has been taken for centuries and they have been the main data for the study of Galilean satellites's ephemerides. In our experiments, we will consider some sessions of astrometry from the Earth during the four years of the mission. We set their accuracy to 10^{-7} radians, which corresponds to tens of kilometers at the Jovian system's distance.

6 ORBIT DETERMINATION

The motion of a celestial body (like a planet, satellite or asteroid) depends on an infinite number of effects and parameters, thus we cannot hope to have a complete mathematical model of its dynamics. However, we can consider a model that approximates the real motion to the best. The state $\mathbf{y}(t)$ of the body (position and velocity, functions of the time t) is the solution of a differential equation

$$\dot{\mathbf{y}} = \mathbf{f}(\mathbf{y}, t, \boldsymbol{\mu}), \tag{6.1}$$

where $\boldsymbol{\mu}$ is the vector of the dynamical parameters (e.g. the mass of a planet) and $\mathbf{f}$ is the function that describes the model. In order to have a good approximation of the motion, the function $\mathbf{f}$ must contain the main accelerations of the dynamics: to know which are the forces we have to take into account, we must consider the accuracy of the observations. If we have a small force, whose effect over the time span we consider is some orders of magnitude below the observations sensitivity, then we can neglect it in the model.

Given initial conditions $\mathbf{y}_0 = \mathbf{y}(t_0)$, which are the position and the velocity of the body at an initial time t_0, we have a Cauchy problem. We define orbit a solution of the problem, determined by $\mathbf{y}_0$ and $\mathbf{f}$. The integral flow $\Phi_{t_0}^{t}(\mathbf{y}_0)$ is the solution at the time t with initial conditions $(t_0, \mathbf{y}_0)$ and it allows to express all the possible orbits of the problem.

In order to pass to an autonomous system, we introduce $\mathbf{z} = (\mathbf{y}_0, t - t_0, \boldsymbol{\mu})^T$; in this way (6.1) becomes

$$\dot{\mathbf{z}}(t) = \mathbf{g}(\mathbf{z}(t)), \tag{6.2}$$

where $\mathbf{g} = (\mathbf{f}, 1, 0)^T$. From (6.2) we can compute $\mathbf{z}$ at the time we want. Since we will need also partial derivatives with respect to the initial conditions, we introduce the transition matrix

$$A(t, \mathbf{z}_0) = \frac{\partial \mathbf{z}}{\partial \mathbf{z}_0}(t, \mathbf{z}_0), \tag{6.3}$$

which describes the variation of the parameters with respect to a change in the initial values. Differentiating (6.2) with respect to $\mathbf{z}_0$, we obtain the variational equation

$$\frac{\partial}{\partial t} A(t, \mathbf{z}_0) = \frac{\partial \mathbf{g}}{\partial \mathbf{z}}(\mathbf{z}(t, \mathbf{z}_0)) A(t, \mathbf{z}_0), \tag{6.4}$$

where the initial condition is $A_0 = I$, since $\mathbf{z} = \mathbf{z}_0$ at the initial time. In terms of $\mathbf{y}$ and $\boldsymbol{\mu}$ we translate (6.4) as

$$\begin{cases} \dfrac{d}{dt}\dfrac{\partial \mathbf{y}}{\partial \mathbf{y}_0} = \dfrac{\partial \mathbf{f}}{\partial \mathbf{y}}\dfrac{\partial \mathbf{y}}{\partial \mathbf{y}_0} \\ \dfrac{d}{dt}\dfrac{\partial \mathbf{y}}{\partial \boldsymbol{\mu}} = \dfrac{\partial \mathbf{f}}{\partial \mathbf{y}}\dfrac{\partial \mathbf{y}}{\partial \boldsymbol{\mu}} + \dfrac{\partial \mathbf{f}}{\partial \boldsymbol{\mu}} \end{cases}$$

Since the aim of the orbit determination is to estimate the parameters that influence the orbit (or some of them), we need observations that constrain the motion of the body. In this way we have two values of the same quantity: the observed one, obtained by a direct measure, and the calculated one, obtained with our model. Comparing them, we can get information about the parameters. A good number of observations allows to obtain an estimation of the parameters we want to solve for.

In the next sections we will introduce the main elements of the orbit determination's theory, as presented in [32], focusing on the particular setting of the JUICE mission.

6.1 THEORY

An observation is a quantity r_i taken at a certain time t_i. In order to perform an orbit determination experiment, we need a function R for the prediction of that observation; in this way we can compute the same observed quantity, we denote as

$$r(t_i) = R(\mathbf{y}(t_i), t_i, \boldsymbol{\nu}). \tag{6.5}$$

Apart from the time and the state vector, the function R depends also on some parameters $\boldsymbol{\nu}$, called kinematical parameters. In (6.5), the dependence on $\boldsymbol{\mu}$ comes out from $\mathbf{y}(t)$.

From the list of parameters $\mathbf{y}_0$, $\boldsymbol{\mu}$ and $\boldsymbol{\nu}$, we choose a sub-list of N elements we denote with the vector $\mathbf{x}$, which contains all the parameters we want to determine. They are called fit parameters.

Generally, in the case of a space mission, the number of the observations is much larger than the number of fit parameters. Therefore, we have to solve an overdetermined system. However, the observations are not perfect measurements,

in fact they have a nominal accuracy for which we admit a range of possible values. The operation we must perform is a fit to the observations.

6.1.1 *Least squares method*

We define the vector of residuals $\xi = (\xi_i)_{i=1,m}$, where $\xi_i = r_i - r(t_i)$ (observed minus calculated) and m is the number of the observations. As ξ depends on the solution $\mathbf{y}(t)$ and the observation function, we can compute the partial derivatives with respect to the fit parameters. We introduce the design matrix

$$B = \frac{\partial \xi}{\partial \mathbf{x}}. \tag{6.6}$$

The goal is to obtain new values of the fit parameters in such a way that the residuals become as small as possible. We define the target function

$$\Omega(\mathbf{x}) = \frac{1}{m}\xi^T W \xi, \tag{6.7}$$

where W is the weight matrix. This matrix consists of coefficients to assign to the observations, so that all of them have a weight, which allows to compare them together. A weight can be just a change in the units of measure, or a judgement about the goodness of the measurement. The simplest way to define the weight matrix is $W = diag(w_i)$ $(i = 1, m)$, with $w_i = 1/s_i^2$, where s_i is the accuracy of the i-th observation.

In order to avoid writing W in all the following formulas, we rescale the residuals $\xi \to \sqrt{W}\xi$.

Our objective is to minimize the target function, then we search for its stationary points through the derivatives of (6.7)

$$\frac{\partial \Omega(\mathbf{x}^*)}{\partial \mathbf{x}} = 0 \quad \to \quad \frac{2}{m} B^T \xi = 0. \tag{6.8}$$

Generally, (6.8) is non-linear, therefore we apply the Newton-Rhapson method in order to find the solution. The matrix of the second derivatives of Ω is

$$\frac{\partial^2 \Omega(\mathbf{x})}{\partial \mathbf{x}^2} = \frac{2}{m}(B^T B + \xi^T H),$$

where $H = \partial^2 \xi / \partial \mathbf{x}^2$. In a neighbourhood of the nominal solution $\mathbf{x}^*$, we have the following Taylor expansion

$$\mathbf{o} = \frac{\partial \Omega(\mathbf{x}^*)}{\partial \mathbf{x}} = \frac{\partial \Omega(\mathbf{x}_k)}{\partial \mathbf{x}} + \frac{\partial^2 \Omega(\mathbf{x}_k)}{\partial \mathbf{x}^2}(\mathbf{x}^* - \mathbf{x}_k) + ...$$

We introduce the normal matrix $C_{new} = B^T B + \xi^T H$ and we obtain

$$C_{new}(\mathbf{x} - \mathbf{x}^*) = -B^T \xi + ... \tag{6.9}$$

The residuals are small quantities, at least near $\mathbf{x}^*$, then we can approximate C_{new} with its main term $C = B^T B$. Moreover, we neglect the terms of higher order in the expansion, so far indicated with continuation dots. Because of these simplifications, in (6.9) we do not have $\mathbf{x}^*$ anymore, but a new vector that we denote with $\mathbf{x}_{k+1}$

$$C(\mathbf{x}_{k+1} - \mathbf{x}_k) = D, \tag{6.10}$$

where $D = -B^T \xi$ is the constant term. This version of the Newton-Rhapson method is called differential corrections. If the approximation is good enough, then $Q(\mathbf{x}_{k+1}) < Q(\mathbf{x}_k)$ and after few steps we obtain convergence.

We have two choices to decide that the procedure is convergent:

- the norm of the correction $|\mathbf{x}_{k+1} - \mathbf{x}_k|_C = |\Delta\mathbf{x}|_C = \sqrt{\Delta\mathbf{x} \cdot C\Delta\mathbf{x}/N}$ to the fit parameters is smaller than a tolerance ϵ_x;
- the relative change of the target function $|Q_{k+1} - Q_k|$ is smaller than a tolerance ϵ_q for a certain number of iterations n_q.

In order to solve the linear system (6.10), we can adopt different approaches; however, we need to compute $\Gamma = C^{-1}$, called covariance matrix, as it contains the uncertainties and the correlations of the fit parameters. In fact, apart from calculating new values of the fit parameters, we find their probabilistic variation in the main diagonal of Γ, from which we can evaluate the reliability of the estimation.

6.1.2 *Confidence ellipsoids*

In order to estimate the reliability of the determination of the fit parameters, we define the confidence region

$$Z(\sigma) = \{\mathbf{x} : |Q(\mathbf{x}) - Q(\mathbf{x}^*)| \leqslant \sigma^2/m\}. \tag{6.11}$$

It depends on the choice of σ and it measures the accuracy of the solution. Apart from the nominal solution $\mathbf{x}^*$, the region $Z(\sigma)$ contains all the values $\mathbf{x}$ we consider acceptable. It is worth paying attention to the value of σ, in order not to have a region too small (too optimistic uncertainty) or too large (degradation of the result). Generally, the values most used are 1 (confidence 1-σ) and 3 (confidence 3-σ).

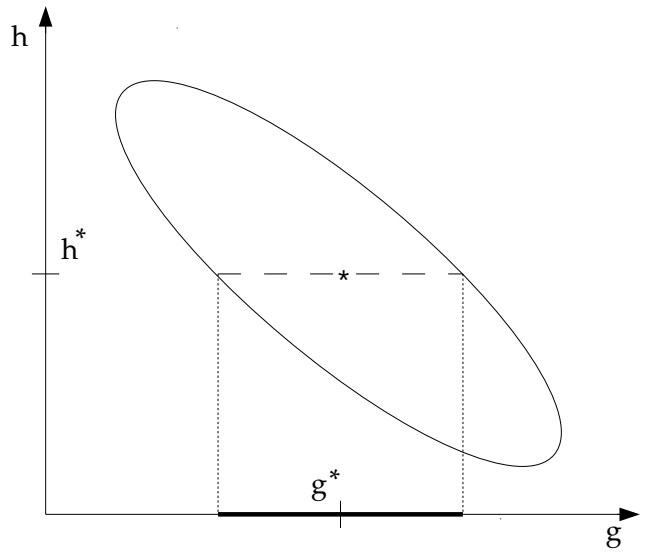

Figure 6.1.: *Representation of a confidential ellipsoid centered in the nominal solution* $[\mathbf{g}^*, \mathbf{h}^*]$. *With the dashed line we indicated the conditional ellipsoid with nominal values* $\mathbf{h} = \mathbf{h}^*$*, while the projection of the ellipsoid on the* $\mathbf{g}$ *space is the marginal one.*

Performing a Taylor expansion of the target function in a neighbourhood of $\mathbf{x}^*$ and keeping only the main term, we can express the penalty $\Delta\Omega = \Omega(\mathbf{x}) - \Omega(\mathbf{x}^*)$ as a quadratic function of $\mathbf{x}$

$$m\Delta\Omega \approx (\mathbf{x} - \mathbf{x}^*) \cdot C(\mathbf{x} - \mathbf{x}^*). \tag{6.12}$$

The confidence region defined in (6.11) becomes an $N-1$ dimensional ellipse, called confidence ellipsoid

$$Z(\sigma) = \{\mathbf{x} : |(\mathbf{x} - \mathbf{x}^*) \cdot C(\mathbf{x} - \mathbf{x}^*)| \leqslant \sigma^2\}. \tag{6.13}$$

Thanks to (6.13), we can give a geometric representation of the uncertainties of the parameters, as shown in Figure 6.1. In fact, the acceptable parameters are contained into the ellipsoid, but according to the direction they lie, they can be closer or further to the nominal solution. The quantities $1/\sqrt{\lambda_i}$, where λ_i are the eigenvalues of C for $i = 1, N$, are the semi-axes of the ellipsoid; therefore, the problem can have weak directions along which the ellipsoid can be very elongated with respect to the other directions.

We can divide the vector of the fit parameters in two sub-vectors $\mathbf{x} = [\mathbf{g}, \mathbf{h}]$. Consequently, we have the following subdivisions for C and Γ

$$C = \begin{bmatrix} C_{gg} & C_{gh} \\ C_{hg} & C_{hh} \end{bmatrix}, \qquad \Gamma = \begin{bmatrix} \Gamma_{gg} & \Gamma_{gh} \\ \Gamma_{hg} & \Gamma_{hh} \end{bmatrix}.$$

The matrix Γ_{gg} is not equal to C_{gg}^{-1}, unless the parameters $\mathbf{g}$ and $\mathbf{h}$ are uncorrelated, i.e. $C_{gh} = 0$.

The expression of the penalty (6.12) becomes

$$\begin{aligned} m\Delta Q \approx &(\mathbf{g}-\mathbf{g}^*)\cdot C_{gg}(\mathbf{g}-\mathbf{g}^*) \\ &+ 2(\mathbf{g}-\mathbf{g}^*)\cdot C_{gh}(\mathbf{h}-\mathbf{h}^*) + (\mathbf{h}-\mathbf{h}^*)\cdot C_{hh}(\mathbf{h}-\mathbf{h}^*). \end{aligned}$$

The uncertainty of the parameters $\mathbf{g}$ depends on the role we choose for the other variables $\mathbf{h}$.

- Conditional ellipsoid for nominal values. We can suppose that the parameters $\mathbf{h}$ are perfectly known $\mathbf{h} = \mathbf{h}^*$. In this case, they do not contribute in the computation of the uncertainty

  $$m\Delta Q \approx (\mathbf{g}-\mathbf{g}^*)\cdot C_{gg}(\mathbf{g}-\mathbf{g}^*).$$

  Since the covariance matrix $\Gamma_g = C_{gg}^{-1}$ is generally different from Γ_{gg}, the confidence ellipsoid is smaller than the case of arbitrary $\mathbf{h}$, as shown in 6.1.

- Marginal ellipsoid. We can consider $\mathbf{h}$ arbitrary and try to compute the covariance matrix for $\mathbf{g}$. Geometrically, we project the ellipsoid on the subspace of $\mathbf{g}$, therefore we calculate the points of the ellipse with a tangent space parallel to $\mathbf{h}$ subspace

  $$\frac{\partial}{\partial \mathbf{h}}(m\Delta Q) \approx 2(\mathbf{g}-\mathbf{g}^*)^T C_{gh} + 2(\mathbf{h}-\mathbf{h}^*)^T C_{hh} = 0.$$

  We explicit the variation of $\mathbf{h}$

  $$(\mathbf{h}-\mathbf{h}^*) = -C_{hh}^{-1} C_{hg}(\mathbf{g}-\mathbf{g}^*)$$

  then we can rewrite the penalty as a function of $\mathbf{g}$

  $$m\Delta Q = (\mathbf{g}-\mathbf{g}^*)\cdot C^{gg}(\mathbf{g}-\mathbf{g}^*),$$

  where $C^{gg} = C_{gg} - C_{gh}C_{hh}^{-1}C_{hg}$. As C_{gg} is non-negative and we have a minus in the formula, the marginal ellipsoid contains the conditional one.

- Conditional ellipsoid for non-nominal values. Another assumption can be to fix $\mathbf{h}$ to a certain $\mathbf{h}_0$, different from the nominal solution. The minimum point becomes

  $$\mathbf{g}_0 = \mathbf{g}^* - C_{gg}^{-1} C_{gh}(\mathbf{h}_0 - \mathbf{h}^*).$$

In this case, the conditional ellipsoid is smaller than the nominal case, because

$$m\Delta Q \approx (\mathbf{g}-\mathbf{g}_0)\cdot C_{gg}(\mathbf{g}-\mathbf{g}_0)+(\mathbf{h}_0-\mathbf{h}^*)\cdot C^{hh}(\mathbf{h}_0-\mathbf{h}^*),$$

where $C^{hh}=C_{gg}^{-1}C_{gh}$.

6.1.3 *Apriori observations*

For some scenarios it can happen that we have a preliminary knowledge of the parameters we want to estimate. Therefore, we can decide to add its contribution into the estimation. Let $\mathbf{x}^P$ be the values already determined for the fit parameters and σ_i $(i=1,N)$ their uncertainties, we can consider them as new observations to be added to the fit.

We define $C^P = diag(\sigma_i^{-2})$ the apriori normal matrix, for which we have the normal equation

$$C^P\mathbf{x}=C^P\mathbf{x}^P.$$

In the case we do not have apriori information for some parameters, we can set to 0 the corresponding weight in C^P.

The new target function is

$$Q(\mathbf{x})=\frac{1}{N+m}\Big((\mathbf{x}-\mathbf{x}^P)\cdot C^P(\mathbf{x}-\mathbf{x}^P)+\xi\cdot\xi\Big)$$

Thanks to the apriori observations, we add information to the normal matrix; the new total normal matrix is

$$C=C_P+B^TB.$$

This operation can help to solve possible inversion problems, arising from rank deficiencies ([32], Chapter 6).

6.1.4 *Multi-arc strategy*

The motion of a body is determined by its equations of motion and initial conditions. In principle, there exists a single initial condition vector for the whole involved time span, that, in the case of a space mission, is its duration. Most of the time a spacecraft is observed only during some sessions of tracking, sometimes distant several days one from each other. Therefore, it is more convenient to divide the mission in different periods of time, called arcs, and to consider single initial conditions for each of them. This is the multi-arc strategy and it is frequently used for the orbit determination of space missions (see [32], Chapter 15). As we

will see in Chapter 7, in the case of a multiple flybys mission, it is unavoidable to choose different initial conditions, because of the chaos that affects the orbit of the spacecraft.

With this formulation, we can divide the vector of the unknown parameters $\mathbf{x}$ in two sub-vectors: $\mathbf{g}$, vector of the global parameters, and $\mathbf{l}$, vector of the local parameters. We call global parameters all the variables that are common to different arcs (for example the gravitational coefficients of Jupiter), and we call local parameters the parameters that intervene only in a single arc (for example the spacecraft's initial conditions of that arc).

The vector $\mathbf{l}$ is composed by the local parameters of each arc $\mathbf{l}_i$ ($i = 1, n$, with n the number of the arcs). We can suppose that the residuals of one arc are independent of the local parameters of the other arcs, so that

$$B^j_{l_i} = \frac{\partial \xi_j}{\partial \mathbf{l}_i} = 0, \qquad i \neq j.$$

With the multi-arc approach, we are considering a bigger dimension of the normal matrix, since we take $6n$ variables as initial conditions, instead of 6. However, the matrix has a simple structure, as the local parameters are independent if they belong to different arcs

$$C_{l_i l_j} = B_{l_i} B_{l_j} = \frac{\partial \xi}{\partial \mathbf{l}_i} \frac{\partial \xi}{\partial \mathbf{l}_j} = 0.$$

As a consequence, the matrix C is block diagonal

$$C = \begin{bmatrix} C_{gg} & C_{gl_1} & C_{gl_2} & \dots & C_{gl_n} \\ C_{l_1 g} & C_{l_1 l_1} & 0 & \dots & 0 \\ C_{l_2 g} & 0 & C_{l_2 l_2} & \ddots & \vdots \\ \vdots & \vdots & \ddots & \ddots & 0 \\ C_{l_n g} & 0 & \dots & 0 & C_{l_n l_n} \end{bmatrix}$$

and in order to solve the differential correction step (6.10), we can adopt a suitable strategy instead of inverting the matrix directly:

$$\begin{cases} C_{gg}\Delta\mathbf{g} + C_{gl}\Delta\mathbf{l} = D_g, \\ C_{lg}\Delta\mathbf{g} + C_{ll}\Delta\mathbf{l} = D_l. \end{cases} \tag{6.14}$$

In (6.14) we indicated $\Delta\mathbf{g}$ the variation $\mathbf{g}_{k+1} - \mathbf{g}_k$ and with $\Delta\mathbf{l}$ that of the $\mathbf{l}$ parameters. Moreover, we separated the constant term D into two parts D_g and D_l. The variation of the local parameters is given by

$$\Delta\mathbf{l}_j = C^{-1}_{l_j l_j}(D_{l_j} - C_{l_j g}\Delta\mathbf{g}).$$

We substitute this expression in the first equation and we explicit the variation of the global parameters

$$\Delta \mathbf{g} = [C_{gg} - \sum_{j=1}^{n} C_{gl_j} C_{l_j l_j}^{-1} C_{l_j g}]^{-1} D_g - \sum_{j=1}^{n} C_{gl_j} C_{l_j l_j}^{-1} D_{l_j}.$$

As we showed in the previous section, $\Gamma_g = C_{gg}^{-1}$ does not contain the total uncertainties of the global parameters, but we have to take into account the contribution of the uncertainty of the local parameters and the various correlations.

Up to now, we have presented the pure multi-arc method. Now we want to introduce a more sophisticated strategy, called constrained multi-arc.

As we consider states of the same body (in particular the spacecraft), we can constrain the initial conditions of one arc with the ones of the subsequent, since they must belong to the same global orbit. Generally, this technique was studied for planetary orbiters, such as the BepiColombo mission around Mercury ([1]), but in the case of flybys distant in time for tens (sometimes hundreds) of days, this can be not straightforward, not only because of the corrective manoeuvres performed outside the sessions of tracking. In fact, as we will explain in Chapter 7, the flybys have a strong impact on the spacecraft's orbit around Jupiter, so that the linking of different arcs must be done carefully.

The idea of the constrained multi-arc strategy is to add a new term to the target function, due to the discrepancy between the propagated states of two arcs (indexes j and $j+1$) at a certain time of conjunction t_c^j

$$\mathbf{d}^{j,j+1} = \Phi_{t_0^{j+1}}^{t_c^j}(\mathbf{y}_0^{j+1}) - \Phi_{t_0^j}^{t_c^j}(\mathbf{y}_0^j), \tag{6.15}$$

where Φ is the integral flow we have already presented. As the arcs are propagated outside the observation sessions for times longer than in the pure multi-arc strategy, we refer to them as extended arcs.

Since we want to minimize the jumps (6.15), the new target function will be

$$Q = \frac{1}{m + 6(n-1)} \xi \cdot \xi + \frac{1}{\mu} \frac{1}{m + 6(n-1)} \sum_{j=1}^{n-1} \mathbf{d}^{j,j+1} \cdot C^{j,j+1} \mathbf{d}^{j,j+1}, \tag{6.16}$$

where μ is called penalty parameter and $C^{j,j+1}$ are the weight matrices for the discrepancy vectors. Their definition depends on the interpretation we adopt; in [1] two approaches are presented: the internally constrained and the apriori multi-arc strategy. In the denominator we have $6(n-1)$, which is the number of constraints if we try to join n arcs. The vectors $\mathbf{d}^{j,j+1}$ depend on global and local parameters of the considered arcs, therefore, when we compute the partial

derivatives (6.8) of the target function, we have to take into account also their contribution.

In this case we do not have a thin arrow shape normal matrix with only diagonal blocks as in the pure multi-arc strategy, since local parameters of subsequent arcs are not independent anymore:

$$C_{l_j l_{j+1}} = B_{l_j} B_{l_{j+1}} \neq 0.$$

If the constraints are between subsequent arcs only, as in the case of the spacecraft, we have a fat arrow shape (represented in [1]), as $C_{l_j l_j}$, $C_{l_j l_{j+1}}$ and $C_{l_j l_{j-1}}$ are different from 0.

Thanks to this added information, we can improve the conditioning of the normal matrix, so that we can reduce the uncertainties of the fit parameters. Moreover, the use of the constrained multi-arc improves the determination of the parameters in the case of a chaotic regime, as shown in [42] and as we will see in Chapter 8.

6.2 FORCES ACTING ON THE SYSTEM

In the first part of the thesis we presented a secular model of the Galilean satellites dynamics. Although it is very useful for the understanding of the main features of the motion, it is not suitable in the context of the modern orbit determination. For a space mission that operates for almost four years and that provides extremely accurate data, we need a very precise model that takes into account several effects. In a full numerical model this is straightforward, since we have just to add the formulas of the accelerations to the right-hand side of the differential equations (6.1).

In this section we introduce the expressions of all the forces we include in the dynamical models. As our task is to study the motion of the Galilean satellites and of the spacecraft, we have to implement a model for both of them. Although the bodies orbit in the same system, the models have important differences, mainly due to two reasons:

- the Galilean satellites have non-negligible masses and we must consider them as extended bodies;
- the ratio area-to-mass of the spacecraft is far from 0, then we have to include non-gravitational forces.

For the Galilean satellites we refer to the dynamical model developed in [21], where a list of perturbations is tested with their effect on the positions over one hundred years of integration. Instead, for the spacecraft, we refer to models already provided for other space missions, such as the NASA mission Juno.

We work on reference systems centered in the main bodies, which can be Jupiter or Ganymede during the orbiting phase, or a Galilean satellite in the case of a flyby.

Since the system is not inertial, as the origin suffers forces that make it accelerate, we have to take into account also the indirect effects.

In the next paragraphs we will present the accelerations acting on a generic body of mass m_s and position $\mathbf{r}_s$, considering a central body with mass m_c. If necessary, we will add some specifications in the case m_s is the spacecraft or one of the satellites.

6.2.1 *Monopole term*

The first force we introduce is the gravitational attraction between the point masses m_s and m_c. From Chapter 2, we know that the expression for its potential is

$$U_0 = \frac{G(m_c + m_s)}{r_s}.$$

In the case of a spacecraft, its mass m_s is so small with respect to m_c, that we can omit it in the formula. In the orbit determination experiments, we introduce a parameter ΔC_{00} that describes the variation of the central body's mass from its standard value $m_c(1 + \Delta C_{00})$.

It is not necessary that m_c is the body that the spacecraft orbits around. For example, during flybys we consider a reference frame with origin in the moon that the probe encounters; if the spacecraft is enough far from the satellite, the main acceleration is the one due to Jupiter and not the one of the monopole term.

6.2.2 *Third-body accelerations*

In the case there are other bodies in the system, we have to take into account also the accelerations due to their gravitational attraction. As we described in Chapter 2, the third-body potential comprehends a direct term (first one in the parenthesis) and an indirect term (second one)

$$U_{3b}(\mathbf{r}_s) = Gm_j\Big(\frac{1}{r_{sj}} - \frac{\mathbf{r}_s \cdot \mathbf{r}_j}{r_j^3}\Big),$$

where j is the index of the new body, $\mathbf{r}_j$ is its position and $\mathbf{r}_{sj} = \mathbf{r}_j - \mathbf{r}_s$.

In our models we consider the third-body accelerations due to the Jovian satellites (including Amalthea and Thebe), the Sun and the planets.

6.2.3 *Expansion of gravitational field*

When m_s is close to an extended body m_c, the approximation of a point mass for the gravitational field is not enough accurate for the determination of its motion.

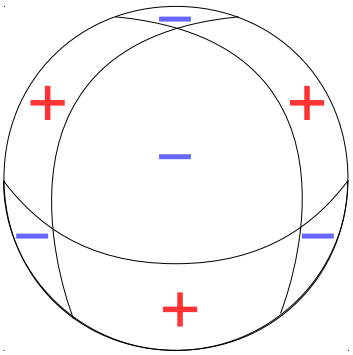

Figure 6.2.: *Schematic representation of the gravitational harmonic with* $l = 4$ *and* $m = 3$*: we have 1 parallel and 4 meridians where the value of the function is 0. The sphere is divided in 8 sectors with different signs which describe the signature of the harmonic. The combination of all the harmonics give a global description of the field.*

In Chapter 3, we presented an expansion in zonal harmonics (3.1), which assumes a symmetry of the field with respect to the z axis. If we want a more realistic model, we have to consider the general case without symmetries. From [32], Chapter 12, we have the new expansion in spherical harmonics

$$U_J(\mathbf{r}_s) = \frac{Gm_c}{r_s}\sum_{l=2}^{\infty}\left(\frac{R_c}{r_s}\right)^l \sum_{m=0}^{l} P_{lm}(\sin(\phi_s))[C_{lm}\cos(m\theta_s) + S_{lm}\sin(m\theta_s)], \tag{6.17}$$

where R_c is the mean radius of the central body, while ϕ_s and θ_s are the latitude and longitude of m_s in a body fixed equatorial reference frame. P_{lm} are the associated Legendre functions of the expansion and the parameters C_{lm} and S_{lm} are the coefficients that characterize the field ($C_{l0} = -J_l$).

In order to compute the accelerations due to the gravitational harmonics, we need to follow the rotation of the body m_c. In fact, the gravitational field is defined in a body-fixed reference frame: if we have a massive mountain or depression on the surface, it must follow the rotation of the celestial body. Therefore, we pass to the body-fixed reference frame through a rotation, we compute the acceleration relative to (6.17) and then we apply the inverse transformation, in order to return to the starting system. In Appendix B we describe the rotational models we implemented for Jupiter and the Galilean satellites.

The gravitational expansion (6.17) is valid both for Jupiter and the Galilean satellites' fields; in Table 6.1 we reported their nominal values. Apart from the direct action of the field, we have to take into account also indirect and secondary effects. The gravitational field of Jupiter acts on the Galilean satellites, but for the third principle of dynamics, the planet must suffer the same force with opposite direction. Since its mass is bigger than the ones of the satellites, the resulting ac-

Parameter	Jupiter	Io	Europa	Ganymede	Callisto
C_{20}	-14735.0	-1845.9	-435.5	-127.8	-32.7
C_{22}	-0.03	553.7	131.0	38.3	10.2
S_{22}	-0.04				
C_{30}	0.2				
C_{40}	588.8				
C_{60}	-27.8				

Table 6.1.: Nominal values of the harmonic coefficients of Jupiter and the Galilean satellites, taken from the L3 ephemerides of the IMCCE.

celeration is much smaller, but not negligible. This acceleration, whose main term is the indirect oblateness, must be included both in the Jupiter-centric dynamical models of the spacecraft and the moons as an indirect term, then with a minus sign

$$U_{Ji}(\mathbf{r}_s) = -\sum_{i=1}^{4} U_J(\mathbf{r}_i)\frac{m_i}{m_0}.$$

The expansion of the Galilean satellites' gravitational field is surely necessary for the spacecraft motion, when it is flybying or orbiting around one of the moon, but it is important also for the satellites' dynamics. In fact, as shown in [21], we must consider additional accelerations on the moons due to their gravitational anomalies. In particular, the effect of Jupiter as point mass on the oblate part of the moons is a non-negligible perturbation; the potential associated is minus (6.17), where C_{lm} and S_{lm} are the satellite's gravitational coefficients, R_c is its radius and $\mathbf{r}_s$ is the Jupiter's position in the moon's body fixed reference system. Since it describes the effect of Jupiter on the satellites, m_c is the mass of the planet. Note that this is not an inertial effect, even if we compute it in the inverse way: the effect of the oblateness of the moons on the planet. In our model we omit the effects of the satellites' oblateness on the other satellites, as they are very small perturbations (some hundreds of meters over 100 years, as shown in [21]).

6.2.4 *Tides*

We introduced the tides in the last section of the first part of the thesis. Briefly, an extended body is deformed by the gravitational force due to an external point mass, as its points suffer a force that is different both in direction and modulus.

Parameter	Jupiter	Io	Europa	Ganymede	Callisto
k_2	0.37	0.45	0.3	0.3	0.3
k_3	0.7	0.3	0.3	0.3	0.3
k_4	0.7	0.3	0.3	0.3	0.3

Table 6.2.: Nominal values of the Love numbers of Jupiter and the Galilean satellites.

This displacement of mass generates an induced field around the deformed body (see [19]) with potential

$$U_T(\mathbf{r}_s) = \frac{Gm_j}{r_j} \sum_{l=2}^{+\infty} k_l \left(\frac{R_c}{r_s}\right)^{l+1} \left(\frac{R_c}{r_j}\right)^{l} P_l(\cos\theta),$$

where $\mathbf{r}_j$ is the position of the body that raises the tides and θ is the angle between $\mathbf{r}_s$ and $\mathbf{r}_j$.

For the Galilean satellites we know that the tidal interaction with Jupiter dissipates energy. In our model we take into account this effect adding the acceleration (4.6), which is proportional to the dissipative parameter k_2/Q, but only for the couple Io-Jupiter. However, for future works, it is worth noting that the dissipative parameter of Jupiter cannot be taken as a constant parameter. In fact, the anelastic tides we described in Chapter 4 are based on an simplified model of the internal structure of the planet: for more realistic models it is necessary to consider the different layers (solid and fluid) of the body. In [13] the authors assumed a solid core covered by a fluid envelope and showed that both layers contribute to the tidal dissipation in the body. This is very important, since it is possible that in the fluid envelope tidal waves are in resonance with the orbital motion of some moons; as presented in [11], this mechanism can increase the effect of the planet's tidal dissipation and speed up the tidal migration of the satellite locked in resonance. In the investigation of the dissipative effects in the Saturn system performed in [25] using data from the Cassini space mission, the authors found a dissipative parameter of Saturn in the frequency of the Rhea's orbit one order of magnitude greater than the ones of the other satellites involved in the study. The reason can be the proximity of Rhea to a resonance with the tidal waves in the upper layers of Saturn.

6.2.5 *Relativistic effects*

When we consider masses in the space, the Newtonian formulation can be not enough to reach the accuracy we desire. In the case of the Jovian system, the mass of Jupiter is so big that the relativistic effects on the near bodies are not negligible.

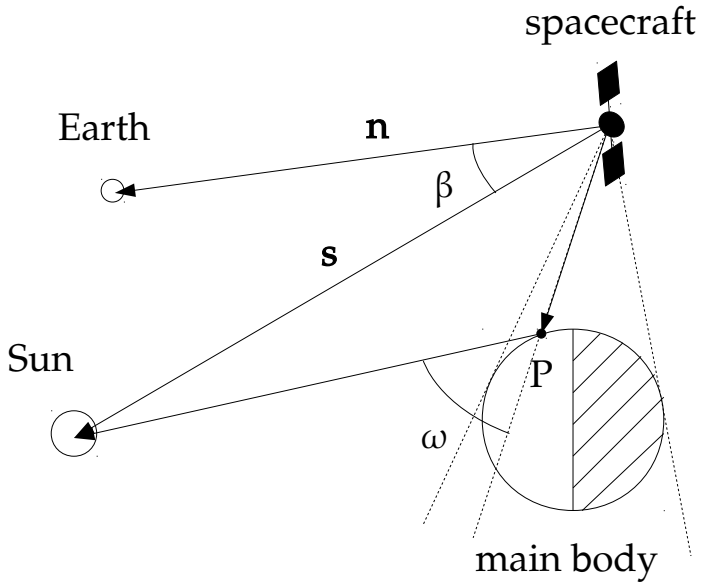

Figure 6.3.: *Representation of the non-gravitational forces' setting. The spacecraft looks toward the Earth (direction $\hat{\mathbf{n}}$), while the photons arrive from the Sun, direction $-\hat{\mathbf{s}}$. Moreover, there are indirect effects due to the proximity to the main body: the point P of the surface is illuminated by the Sun, then it reflects the radiation of the Sun (albedo), and it releases infrared radiation.*

Therefore, in our model we add an acceleration that takes into account the general relativity correction to the motion

$$\mathbf{F}_{GR}(\mathbf{r}_s, \mathbf{v}_s) = \frac{Gm_c}{c^2 r_s^3}\Big((2(\gamma+\beta)\frac{Gm_c}{r_s} - v_s^2)\mathbf{r}_s + 2(1+\gamma)(\mathbf{r}_s \cdot \mathbf{v}_s)\mathbf{v}_s\Big),$$

where γ and β are two post-Newtonian parameters (see [49]). Since we do not perform test on the violation of the general relativity theory, we fix them to their conventional value, which is 1.

6.2.6 *Non-gravitational forces*

There are some effects in the space that do not have gravitational nature. They are important when the ratio between area and mass of the object is far from 0; generally this is not the case of celestial bodies of great dimensions, which are very massive. However, for asteroids and spacecraft the area-to-mass A/m_s is an important parameter.

We assume a very simple model of the spacecraft: we consider a flat structure composed by two solar arrays of 50 m^2 and a central body of 10 m^2, as represented in Figure 5.1. Since the antenna is pointed toward the Earth, the spacecraft

is orthogonal to the direction spacecraft-Earth; we indicate this direction with $\hat{\mathbf{n}}$. Instead, for the direction spacecraft-Sun we use $\hat{\mathbf{s}}$; the position of the Sun is essential to describe non-gravitational forces, being their main source. In Figure 6.3, we have a representation of the considered configuration.

The first force we take into account is the direct solar radiation pressure, due to the photons that hit the spacecraft,

$$\mathbf{F}_{srp} = -\frac{\Phi_{\odot}}{c} A \cos\beta \hat{\mathbf{s}},$$

where β is the angle between the two directions $\hat{\mathbf{n}}$ and $\hat{\mathbf{s}}$. It describes the inclination of the photons with which they arrive at the flat surface ($A\cos(\beta)$ is called the effective area). The other parameters are $\Phi_{\odot}$, which is the Sun's radiation flux at the distance of the Jovian system (almost 5×10^4 $erg/(cm^2 s)$), and the light speed c.

Moreover, we consider also indirect effects:

- if the spacecraft is near the central body, part of the radiation that arrives at the surface is reflected and hits the probe. If we indicate with α_P the coefficient of absorption, then the fraction of bounced light is $\overline{\alpha} = (1 - \alpha_P)$, which is called albedo coefficient. This effect must be considered only if the spacecraft is exposed to points of the surface that are illuminated; the formula for the force is

  $$\mathbf{F}_{\overline{\alpha}} = -\frac{\Phi_{\odot}}{c} \overline{\alpha} A \cos\omega \frac{\mathbf{x} - \mathbf{P}}{|\mathbf{x} - \mathbf{P}|},$$

  where ω is the angle between the direction $\mathbf{x} - \mathbf{P}$ and $\hat{\mathbf{n}}$.

- Moreover, the central body itself has a thermal emission, detectable as infrared radiation. In this case, it is not important that the point P is illuminated, as it releases radiation that cumulates during its rotation. In this case, the formula of the force is

  $$\mathbf{F}_{IR} = -\frac{\Phi_{IR}}{c} A \cos\omega \frac{\mathbf{x} - \mathbf{P}}{|\mathbf{x} - \mathbf{P}|},$$

  where Φ_{IR} is the thermal flux of the central body.

In order to compute the indirect effects, we perform an integration over the visible (from the spacecraft) surface of the planet.

Finally, since we will propagate the spacecraft also outside the tracking sessions, we must consider manoeuvres performed using the on-board fuel. In first approximation, they can be studied as instantaneous change in the velocity; their contributions is very important in order to allow corrections to the orbit and not to miss the flybys during the tour.

For modelling these manoeuvres, we follow [1]. We consider a total variation in velocity of $\Delta\mathbf{v} = (\Delta v_R, \Delta v_T, \Delta v_W)$, expressed in the orbital reference frame (R, T, W). In order to have a smooth formulation, we consider a piecewise acceleration composed by two 5 degrees polynomials and a constant acceleration

$$a = \begin{cases} b_4 t^4 + b_5 t^5 & \text{if} \quad t \leqslant \Delta s \\ b_4 \Delta s^4 + b_5 \Delta s^5 & \text{if} \quad \Delta s < t < \Delta h - \Delta s \\ b_4 (\Delta h - t)^4 + b_5 (\Delta h - t)^5 & \text{if} \quad t \geqslant \Delta h - \Delta s \end{cases}$$

and whose integration over the time Δh of the manoeuvre gives the requested $\Delta\mathbf{v}$.

Some manoeuvres are already scheduled in the mission plan reported in the Spice Kernel: the biggest one is the JOI manoeuvre we already presented. However, we added small manoeuvres between each flyby, in order to recover a whole pseudo-orbit of the spacecraft tour, as we will describe in Chapter 7.

6.3 OBSERVATION MODELS

In (6.5) we introduced the prediction function for the computation of the observations. Since we use different kinds of observations, we need a prediction function for each of them. In Figure 5.7 we have a schematic representation of the range, range-rate and angular observations; in this section we want to formalize their computation.

As we will explain in Chapter 7, during the tracking sessions, we will consider the state of the spacecraft with respect to the satellite that the probe is flybying or orbiting around. We call this moon as the primary Galilean satellite and we use its state in order to define the prediction functions.

6.3.1 *Range and range-rate*

The range is the distance from a ground based station to the spacecraft. In order not to limit the visibility conditions, we assume that the observations are taken from the center of the Earth. In Figure 6.4 we drew the position vectors we use to define the range vector:

$$\boldsymbol{\rho} = (\mathbf{x}_{bjs} + \mathbf{x}_{jup} + \mathbf{x}_{gs} + \mathbf{x}_{sc}) - \mathbf{x}_{ea}. \tag{6.18}$$

In particular, $\mathbf{x}_{bjs}$ and $\mathbf{x}_{ea}$ are respectively the position of the BJS (Barycenter of the Jovian System) and the Earth with respect to the SSB (Solar System Barycenter), $\mathbf{x}_{jup}$ is the position of the center of mass of Jupiter with respect to the BJS, $\mathbf{x}_{gs}$ is the position of the primary Galilean satellite with respect to Jupiter and $\mathbf{x}_{sc}$ is the position of the spacecraft with respect to the primary moon.

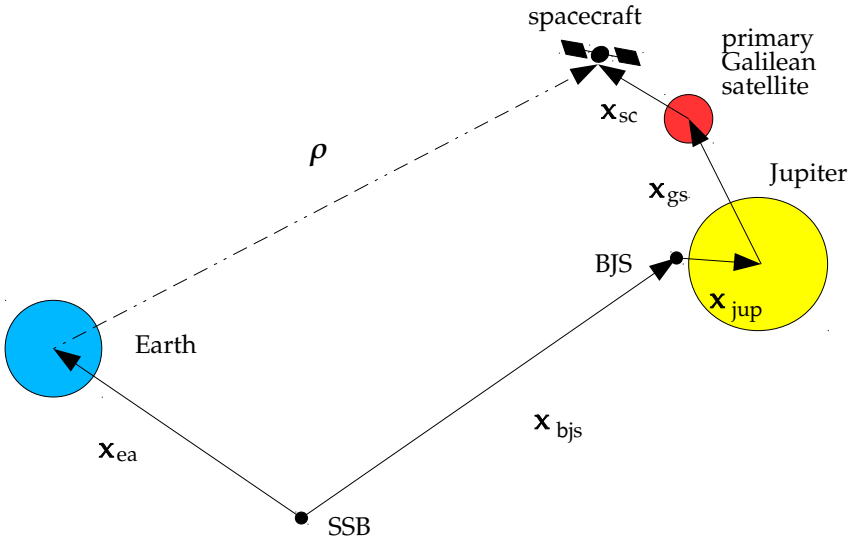

Figure 6.4.: *Range measurements are computed from the sum of various vectors, which are the positions of the different bodies involved in the problem.*

In the previous section we introduced the accelerations we use to propagate $\mathbf{x}_{gs}$ and $\mathbf{x}_{sc}$ at the requested times. However, we need also the other vectors present in (6.19). The vector $\mathbf{x}_{bjs}$ is computed propagating a relativistic N-body problem, implementing the EIH equations ([49]) and taking into account the Sun and all the planets different from Jupiter. The vector $\mathbf{x}_{jup}$ is derived from the positions of all the Galilean satellites, assuming that their sum, weighted with the masses, must give the barycenter of the system; in fact, all the other satellites contribute poorly to the determination of the barycenter. Instead, the vector from SSB to the Earth is taken from the JPL ephemerides. The choice not to propagate the Earth is due to the fact we are not interested in improving the Earth's orbit using JUICE data.

Since the range measurement is a scalar quantity, the expression of the prediction function is

$$\rho = |(\mathbf{x}_{bjs} + \mathbf{x}_{jup} + \mathbf{x}_{gs} + \mathbf{x}_{sc}) - \mathbf{x}_{ea}| + S(\gamma), \tag{6.19}$$

where the function $S(\gamma)$ represents the Shapiro effect, which describes the delay of the radio signal for the deformation of the space-time due to the presence of massive bodies. For the setting of the JUICE mission, we have to consider the deformation due to the Sun and Jupiter. From [48], the function S at the 1-PN (Post-Newtonian) level is

$$S(\gamma) = \frac{(1+\gamma)Gm_c}{c^2} \ln\left(\frac{r_t + r_r + r}{r_t + r_r - r}\right), \tag{6.20}$$

where r_t and r_r are the distances of the transmitter and the receiver from the body m_c that generates the space-time deformation, and r is their mutual distance. The contribution of the Shapiro effect of the Sun on the range measurements is of the order of tens of kilometers and the one of Jupiter tens of meters. Since they are greater than the accuracy of the radioscience observations, they must be taken into account. Actually, for the processing of real data we should also consider the expansion (6.20) up to the 2-PN order and the Shapiro effect due to the J_2 of Jupiter, which becomes non-negligible when the signal pass very close to the planet.

In order to predict real observations, we need to take the various vectors in (6.19) at the right times. In fact, the radio signal has a finite velocity, which is the light speed c, and it reaches the Jovian system after a certain travel time after its departure. If we consider that the distance of the Earth from the Sun is almost 1 au and the distance of Jupiter is almost 5.2 au, we find that the order of this time gap is 40 minutes.

Therefore, we have to consider three different times when we compute the range measurements. There is a time of transmission t_t, at which the signal leaves the Earth; it arrives in the Jovian system at a time t_b, called of bouncing, as it is immediately redirected to the Earth; finally it returns to our planet at a time of receiving t_r. Therefore, for tracking data, we have to consider the 2-way trip, go and return.

We know the time of receiving, as the station captures the signal, then we have to recover the other two involved times. We have a downlink trip

$$\rho_{down} = |(\mathbf{x}_{bjs}(t_b) + \mathbf{x}_{jup}(t_b) + \mathbf{x}_{gs}(t_b) + \mathbf{x}_{sc}(t_b)) - \mathbf{x}_{ea}(t_r)| + S_{down}(\gamma),$$

where the vectors in the brackets are computed at the time of bouncing, while the position of the Earth at the time of receiving. The quantity S_{down} is the Shapiro effect on the down path of the signal; also for its computation we have to consider r_r and r_t in (6.20) at the right times.

In order to obtain t_b we perform an iterative process. We have a first guess for t_b given by the rough estimation we performed with a default distance between the Earth and Jupiter; then we compute the vectors in the brackets at that time. We obtain a first estimation of the downlink range, from which we have a new value for the travel time of the signal and for t_b. At the following iteration we use the new value and we replicate the computation, and we continue until the variation in t_b is below 10^{-12} seconds. More details of the procedure can be found in [48].

Successively, we consider the uplink trip

$$\rho_{up} = |(\mathbf{x}_{bjs}(t_b) + \mathbf{x}_{jup}(t_b) + \mathbf{x}_{gs}(t_b) + \mathbf{x}_{sc}(t_b)) - \mathbf{x}_{ea}(t_t)| + S_{up}(\gamma),$$

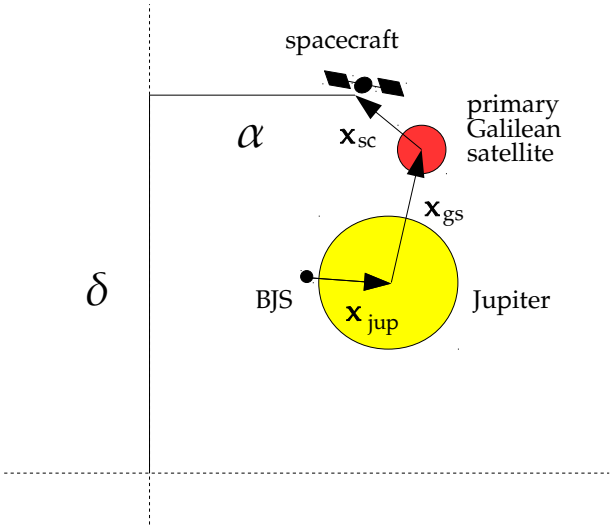

Figure 6.5.: *VLBI measurements are computed from goniometric functions applied to the range vector coordinates.*

where the position of the Earth is taken at the time of transmission. In order to compute t_t, we have to perform the same iterative process used for t_b.

The final formulation we use for the range measurement is

$$\rho = \frac{\rho_{down} + \rho_{up}}{2},$$

in this way 2ρ provide the whole travel time of the signal.

For the range-rate the approach is equivalent: we consider its expression in function of the velocity vectors of the bodies

$$\dot{\rho} = |(\dot{\mathbf{x}}_{bjs} + \dot{\mathbf{x}}_{jup} + \dot{\mathbf{x}}_{gs} + \dot{\mathbf{x}}_{sc}) - \dot{\mathbf{x}}_{ea}| + \dot{S}(\gamma), \tag{6.21}$$

and we compute them at the right times. The function $\dot{S}(\gamma)$ is the time derivative of the function (6.20) and represents the Shapiro effect on the range-rate (see [48]).

6.3.2 *VLBI*

VLBI data provide the angular positions of the spacecraft with respect to a certain ground based station; also in this case we consider geocentric observations.

The vectors that are involved in the computation are the same of the radioscience data, then we express the angles using the same quantities

$$\begin{aligned} \alpha &= \arctan\left(\frac{\sqrt{\rho_x^2 + \rho_y^2}}{\rho}\right), \\ \delta &= \arcsin\left(\frac{\rho_z}{\rho}\right); \end{aligned} \tag{6.22}$$

where $\boldsymbol{\rho}$ is the vector defined in (6.18) and the subscript indicates a particular component.

Differently from the range and range-rate, in this case we consider a 1-way downlink trip. Therefore, we must consider just the time of receiving t_r and the time t_b of departure of the signal from the spacecraft (we continue to use b as subscript, even if the signal is not really bounced).

6.3.3 *Astrometry and camera*

Earth based astrometry and JANUS experiments provide the same kind of observations of VLBI (right ascension and declination), which we can model following (6.22). However, in the case of the camera mounted on the spacecraft, the vector $\boldsymbol{\rho}$ in (6.22) is not the same of ground based observations.

In fact, the spacecraft is orbiting in the Jovian system: the Earth, the BJS and Jupiter's positions are not involved in the computation. We assume that JANUS will take astrometric pictures of the moons outside the tracking sessions and then when the probe will be far from the satellites. For this reason, the vector $\boldsymbol{\rho}$ is simply

$$\boldsymbol{\rho} = \mathbf{x}_{gs} - \mathbf{x}_{sc}^{J},$$

where $\mathbf{x}_{gs}$ is the target moon the camera is observing and $\mathbf{x}_{sc}^{J}$ is the Jupiter-centric position of the spacecraft.

Both for astrometry and camera we use the prediction functions defined in (6.22). As showed in [8], these kinds of observations will be very important to stabilize the inversion of the normal matrix, being the only occasion to get direct measurements of Io during the mission.

7 METHODS

In this chapter we describe the code we implemented and the strategy we adopted within ORBIT14 for the orbit determination experiments in the JUICE mission' scenario. ORBIT14 is an orbit determination software developed by the Celestial Mechanics Group of the University of Pisa. It is a mission designed code, it means that the software has specific and separated parts in order to deal with different space missions. The standard version of ORBIT14 contains orbit determination tests for the BepiColombo mission to Mercury, the Juno mission to Jupiter and Super Conjunction Events for a spacecraft in cruise behind the Sun. In this work of thesis we developed a new branch of the code in order to add the new project regarding the JUICE mission.

For all the missions there is a common core that deals with the basic elements of propagation and orbit determination. However, the software is developed having in mind that each space mission is different from the other, both for its tour and its purposes. A strategy for an orbiter is not suitable for a multiple flybys mission, just like a mission to Jupiter can be very different from a mission to Mercury. For example, the code already written for the Juno mission lacks important aspects for processing JUICE mission's data. Moreover, it is very complicated to design a software that can deal with all the possible scenarios; therefore, we prefer to develop the software around the tasks of the current mission we are studying.

ORBIT14 counts more than 100000 rows of Fortran code: it comprehends modules and subroutines for the integration of differential equations, for reading planetary ephemerides, simulating the rotation of the bodies and so on. The most of the work for this thesis has been done on the modules that define the dynamical models and the prediction functions. For example, before the JUICE project, in ORBIT14 it was not present a module for the propagation of the Galilean satellites' motion or for the computation of VLBI observations.

The project is structured in two main programs, a simulator and a corrector. The first one is necessary when real observations are not available, as in the case of the JUICE mission, that will begin to provide data only from 2029. It consists in a simulation of the observables, performed with the dynamical and observational models introduced in Chapter 6. We add a Gaussian noise to the observed data with a standard deviation equal to the precision of the observations, in order to take into account the limits of accuracy of the measurements. Moreover, we can

choose to add systematic errors to the observations introducing bias or changing the value of some dynamical parameters between simulation and correction. In this way, the residuals will be different from zero and we will begin with a non-trivial value for the target function.

In the corrector we generate the calculated data and we perform the differential corrections, in order to find the minimum of the target function, function of the fit parameters. In the next sections we will show which parameters we are interested in determining and the strategy we adopt for dealing with the critical issues arising from treating a mission like JUICE.

7.1 REQUIREMENTS OF THE MISSION

In the description of the radioscience experiment presented in [17], the JUICE Science Team listed the parameters that JUICE is going to determine. They are mainly gravitational and tidal parameters, but with the adding of VLBI data it is possible to obtain also results on the states of the Galilean satellites and the dissipative parameters. The basic results that are required are

- determination of the gravitational field of Ganymede up to order 10;
- determination of the gravitational field of Callisto up to order 3;
- improvement of the gravitational field's parameters C_{20} and C_{22} of Europa;
- determination of the time-dependence of gravity at degree 2 arising from the eccentricity tide for Ganymede and Callisto;
- improvement of the ephemerides of the Solar System and the Jovian satellites;
- improvement of the dissipative parameters.

In the orbit determination experiments we are going to perform, we will take into account this list for the choice of the fit parameters. As we noted in Chapter 5 and it is clear from the mission's requirements, Ganymede will be the moon whose properties JUICE will investigate more deeply. In the analysis of the results of our experiments, we will focus on the last two points, which are the main objectives of investigation of this thesis.

It is worth noting that we are going to present a first analysis of the orbit determination for JUICE, for which we are interested in preliminary results on the uncertainties recovered in the covariance matrix. Dealing with real data is a more complicated challenge and there are different adjustments of the software we need to develop yet. However, with the current version of the code, we can perform a first complete inversion of the JUICE data.

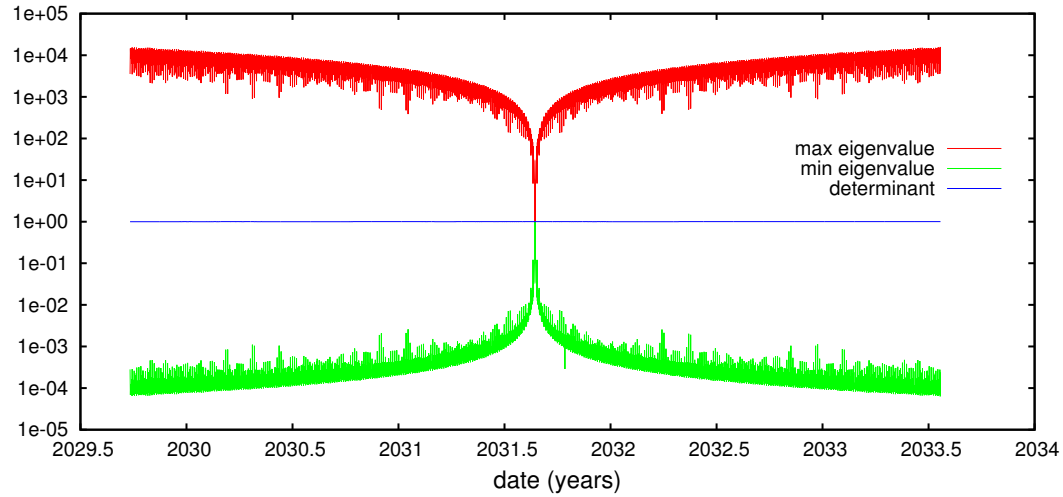

Figure 7.1.: *Spectral properties of the transition matrix (dimension 24 × 24) of the Galilean satellites: in red we reported the absolute value of the greatest eigenvalue, in green the absolute value of the smallest eigenvalue and in blue the determinant.*

7.2 CRITICAL ISSUES

The JUICE mission has several complications, in particular due to its multiple flybys phase. As we described in Chapter 5, during its tour around Jupiter, the spacecraft will encounter the moons 23 times. For each flybys, the spacecraft will fly over a predetermined region of the target moon, in order to fulfill the requirements of the different experiments of the mission. It means that the orbit must be accurately calculated and it must be possible to correct the trajectory through space manoeuvres. In this section we will show the impossibility to compute a single global orbit for the spacecraft, because of the chaos.

Moreover, for the orbit determination, we are demanding a very strong capability: we want a strict control on a 4 years propagation, where with control we mean that we are able to modify the initial conditions in order to change the propagated body's states of an amount of the requested order. For JUICE we would be able to correct the initial conditions of the Galilean satellites without having uncontrolled changes of the residuals. Actually, as we will see, this control is not perfect. This will have repercussions especially for the jumps of the extended arcs and the convergence of the differential corrections.

7.2.1 *Convergence control*

In order to improve the moons' ephemerides and to determine the tidal dissipation parameters, we have to propagate the Galilean satellites for the whole length of

Flyby	Target Body	$\partial x/\partial \dot{x}_0$	$\partial y/\partial \dot{y}_0$
1	Ganymede	-50.0	108.0
2	Ganymede	-35.7	72.1
3	Ganymede	-30.7	64.6
4	Ganymede	-4.1	-84.6
5	Ganymede	-3.9	-79.9
6	Europa	-17.8	5.2
7	Europa	-17.3	0.5
8	Callisto	-49.9	-11.2
9	Ganymede	-9.5	63.1
10	Callisto	-18.7	11.2
11	Callisto	-17.4	10.5
12	Callisto	-15.9	9.8
13	Callisto	-14.5	9.0
14	Callisto	-8.1	5.5
15	Callisto	-6.8	4.7
16	Callisto	-5.5	4.0
17	Callisto	-4.3	3.3
18	Callisto	-2.9	2.6
19	Ganymede	-2.0	4.7
20	Ganymede	0.7	-1.1
21	Ganymede	1.4	5.1
22	Callisto	10.4	0.4
23	Callisto	-21.4	-2.4

Table 7.1.: Values (to be multiplied by 10^6) of some elements of the transition matrix of the primary satellite at the times of the flybys. In particular, x and y are two coordinates of the primary moon's position at the time of the corresponding flyby, while $\dot{x}_0$ and $\dot{y}_0$ are the initial conditions of the primary moon's velocity.

the mission. We choose the initial time t_0 in the middle of the time span and we propagate forward and backward. The distance of the first flyby from t_0 is almost 2 years.

The problems arise when we consider a change of the initial conditions of the order of the machine error: since we use double precision, we refer to a change in the sixteenth decimal digit. In order to study the variation of the state at a certain time t, we can look at the transition matrix (6.3); in Figure 7.1 we plotted the maximum and minimum eigenvalues of the moons' transition matrix. The value of the maximum at the end of the propagation is almost 10^4, which is quite limited. However, if we look at single components of the matrix, we can find greater values. In Table 7.1, we reported two elements, relative to the primary moons, of the transition matrix at the time of the flybys. For the first flyby, we have that a change δ in $\dot{y}_0$ of Ganymede leads to a variation in $y(t)$ greater than $10^8\delta$. This means that a change at the level of $10^{-15}\dot{y}_0 \approx 10^{-9}cm/s$ implies an uncontrolled change of 10^{-1} cm in the state of Ganymede in the first flyby.

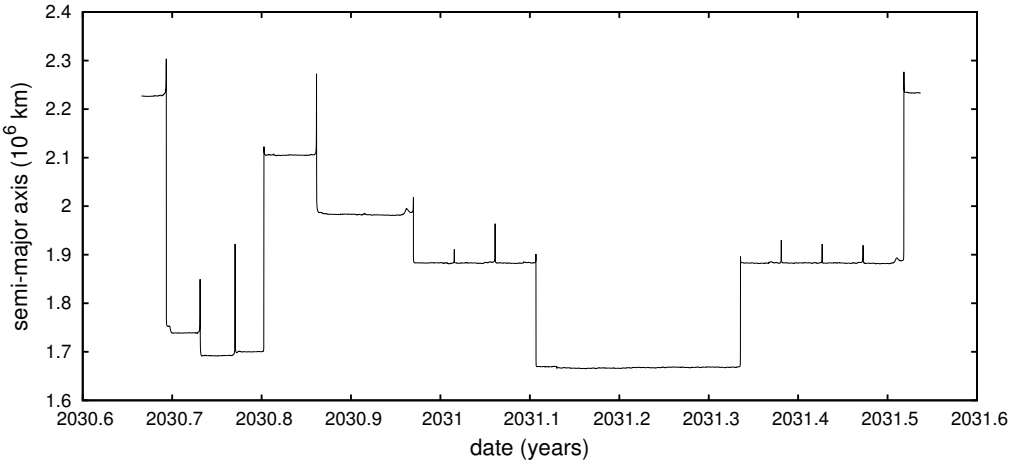

Figure 7.2.: *Semi-major axis of the spacecraft orbit during the flybys phase. Each jump or pulse is due to a close encounters with one of the moons.*

Since the range observations have an accuracy of the order of 10 centimeters, when the residuals reach the level of the noise, the differential corrections have some difficulties to change the parameters in order to control the value of the target function at the order of $\Delta\xi^2/w \approx 10^{-2}/10 = 10^{-3}$. This does not occur just for the first flybys, but also for the furthest arcs of the Ganymede orbiting phase. Therefore, instead of a perfect convergence, the parameters move around a minimum point and the target function begins to oscillate around its minimum value. The same computations and the same table can be done for the velocities and the range-rate observations. In light of this behaviour, we will define suitable convergence criteria.

It is worth noting that, as evidenced by Figure 7.1, this effect is linear with time; therefore, it could be easily solved using quadruple precision, instead of double. However, for a software like ORBIT14, which uses also external Fortran libraries and a great number of modules developed during a wide time span, it is not straightforward to pass to quadruple precision. Moreover, the time of execution would increase dramatically.

7.2.2 *Chaos in the JUICE orbit*

The most challenging aspect of the mission regards the spacecraft's orbit during the flybys phase. As shown in Figure 7.2, at each flyby the probe suffers a sort of kick that can change abruptly its orbit around Jupiter. For some flybys the semi-major axis changes more than 4×10^5 km, it means a change of the order of the Io's orbit. Near the close encounters a small change in the state of the spacecraft can generate a completely different orbit: this is the phenomenon known as chaos.

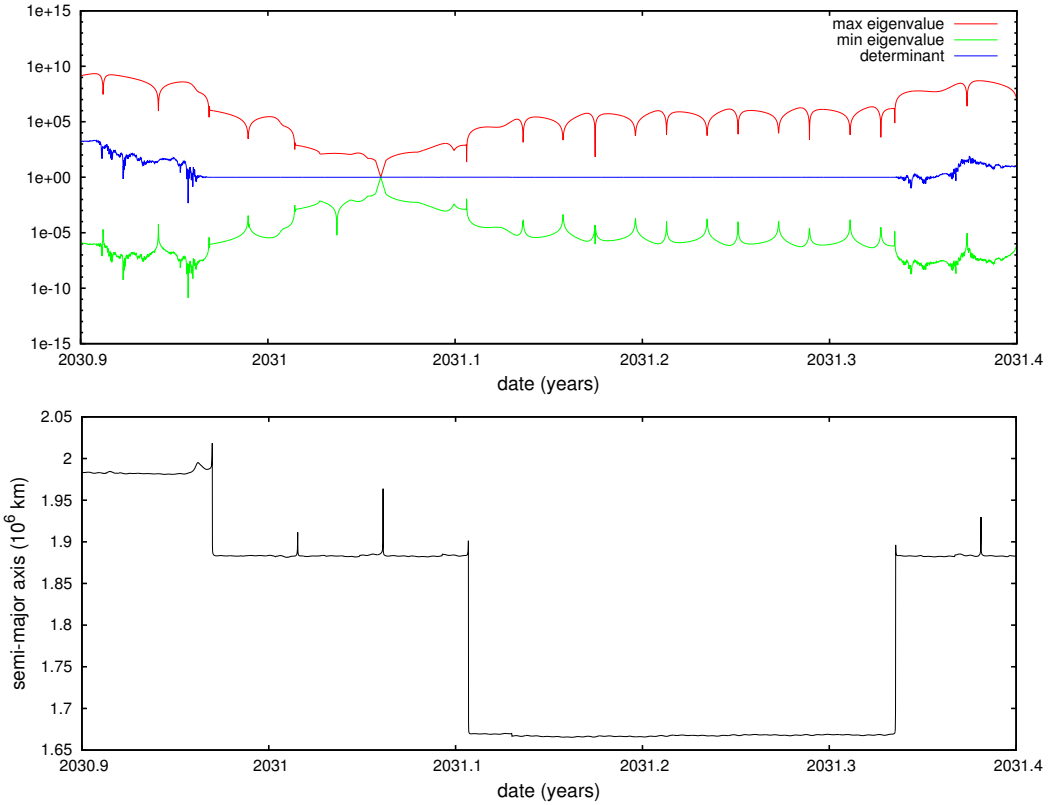

Figure 7.3.: *On the top, spectral properties of the transition matrix of the spacecraft, taking the initial condition at the 12th flyby: in red we reported the absolute value of the greatest eigenvalue, in green the absolute value of the smallest eigenvalue and in blue the absolute value of the determinant. On the bottom we show a piece of the spacecraft's orbit once again, in order to compare the divergence of the matrix with the occurrence of the flybys.*

Therefore, if the tour foresees a series of flybys accurately scheduled, any small change can be catastrophic. Actually, it is possible to adjust the orbit thanks to space manoeuvres, but the real problem is numerical.

In fact, it is over the machine's capability to compute a whole orbit for the spacecraft starting from a single initial condition; this is a limitation due to the finite representation of the numbers: after some flybys the divergence of the machine error is propagated to thousands of kilometers, missing the following flyby. Differently from the divergence of the moons' transition matrix, this effect is not linear, but exponential; therefore, passing to quadruple precision would allow to catch twice the flybys, but not to solve the problem. In order to show the effect of the chaos, we refer to Figure 7.3. In the top picture we plotted the maximum and the minimum eigenvalue of the transition matrix (6.3) of the spacecraft's orbit, starting from an initial condition taken at the 12th flyby. By comparison with the bottom

picture, we can note the abrupt increment of the matrix's divergence each time that a flyby occurs: after the third flyby (both forward and backward, counting also the flyby at the initial condition of the spacecraft) we find that the absolute value of the maximum eigenvalue is greater than 10^8 and the absolute value of the minimum eigenvalue is smaller than 10^{-8}. Since the ratio is 10^{16}, which is the order of the machine error, the transition matrix becomes bad conditioned, and from the value of the determinant, which should be 1 since the matrix is symplectic (less than for small terms), we have a prove of the effects of the numerical instability. In the next section, we will present an attempt to recover the whole orbit and we verify the empirical computation horizon we found.

Although this could seem a problem only for the design of the mission, it affects also the orbit determination. In [46], the authors studied a relatively simple chaotic problem: they considered the dynamical model of a pendulum and they discretized it with the standard map. They took the initial condition in a chaotic region and they generated a chaotic orbit from which they obtained simulated observations. During the correction operation they tried to estimate the initial conditions and a dynamical parameter present in their formulation. They found that the computation became unstable after a certain number of iterations of the map, showing the existence of a computation horizon. Moreover, they proved that the determination of the dynamical parameter produces a sharp degradation of the initial conditions' estimation. In fact, in the case of no determination of the dynamical parameter, the uncertainty of the initial conditions decreased exponentially with the number of map's iterations, while when they added the parameter to the fit parameters, the same uncertainty decreased just as a polynomial, because of the correlations.

In [42], the authors tried to solve these limitations using a multi-arc approach. This technique has been proved to break down the barrier of the computation horizon; moreover, they showed that the constrained multi-arc strategy improves the determination of the parameters in the case of a chaotic orbit. However, they found that they could not demand too strict constraints for the jumps of the extended arcs; in fact, this request is almost the same of searching for a single orbit, which leads to the same problem described in [46].

Although in the cited articles the authors studied a simple model, its relation with JUICE is deep. In fact, we consider a spacecraft in a chaotic orbit and we want to determine dissipative coefficients, that are dynamical parameters for which we need the whole time span of the mission for obtaining a good estimation.

In light of these two papers, we give up the hope to find a global orbit and we use the constrained multi-arc method in order to find new local initial conditions for the spacecraft in such a way that the jumps (6.15) at the connection times are smaller than the accuracy of the observations. Moreover, we will use the constrained multi-arc strategy in the orbit determination experiments, but only

for the flybys phase. In fact, as shown in [42], this strategy is advantageous in the case of chaotic orbits, but in the ordered case, such as the Ganymede orbiting phase, it does not really improve the estimation of the dynamical parameters.

7.3 SWITCH OF THE DYNAMICS

In Chapter 6, we described the accelerations that act on the spacecraft and the Galilean satellites. In this section, we present the different dynamics we implemented and the way we use them.

First, we have a dynamics for the Galilean satellites that we propagate for the whole length of the mission. Instead, for the spacecraft, we abandoned the hope to do the same, because of the chaos. During the flybys we choose to use a satellite-centric dynamics, i.e. a dynamics defined in a reference system centered in the primary moon, since we want that the satellite's state is included in the prediction functions (as presented in Chapter 6); while, far from the flybys, we prefer a Jupiter-centric dynamics, i.e. defined in a reference system centered in Jupiter.

The definition of two dynamics has two main reasons: first, involving the states of the moons in the prediction functions allows to obtain more information about their orbits, while it has no sense to propagate the spacecraft's state in a satellite-centric reference system when JUICE is very distant from the moon. Moreover, since we want to use a constrained multi-arc strategy and we have to calculate the jumps (6.15), we need the spacecraft' states in the same system.

For each arc of the flybys phase, we take the initial conditions at the pericenter of the hyperbolic orbit and we propagate forward and backward with the satellite-centric dynamics. After 12 hours, when the spacecraft is enough far from the primary moon, we switch to a Jupiter-centric reference frame, as represented in Figure 7.4. This switch is done using the transformation

$$\begin{cases} \mathbf{X}^{J}_{sc}(t_s) = \mathbf{X}_{sc}(t_s) + \mathbf{X}_{gs}(t_s), \\ \dfrac{\partial \mathbf{X}^{J}_{sc}}{\partial c_i}(t_s) = \dfrac{\partial \mathbf{X}_{sc}}{\partial c_i}(t_s) + \dfrac{\partial \mathbf{X}_{gs}}{\partial c_i}(t_s), \qquad i = 1, N \end{cases} \tag{7.1}$$

where t_s is the time we perform the switch and c_i ($i = 1, N$) are the fit parameters. The vectors $\mathbf{X}$ represent the states of the bodies: $\mathbf{X}^{J}_{sc}$ is the state of the spacecraft in the Jupiter-centric system, $\mathbf{X}_{sc}$ in the satellite-centric system and $\mathbf{X}_{gs}$ the state of the primary Galilean moon with respect to Jupiter. The formulas (7.1) define a Newtonian change of coordinates; for a more accurate transformation we should use a relativistic formulation, as presented in [48], which involves also the times of the different reference systems. Although in the simulations the use of (7.1) or more sophisticated equations does not affect the results we are going to show, the second ones will be necessary in the processing of real data.

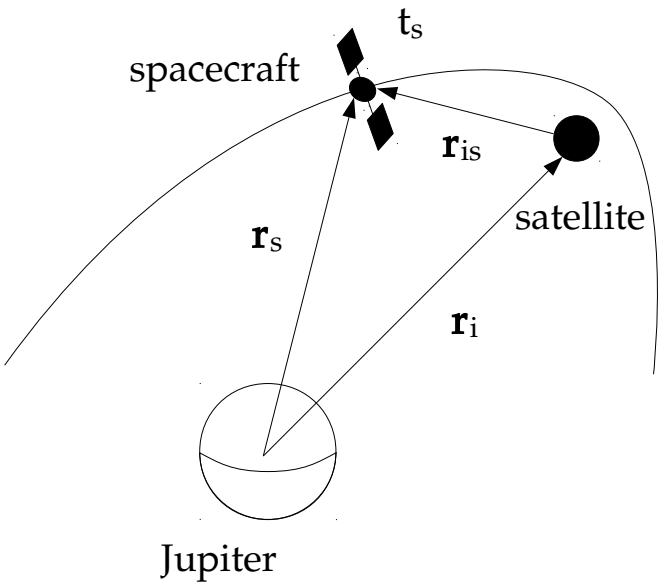

Figure 7.4.: *Scheme of the switch of the dynamics: the vector $\mathbf{r}_{is}$ is computed from the satellite-centric dynamics* `dyn11x`*, while the vectors $\mathbf{r}_i$ and $\mathbf{r}_s$ from the Jupiter-centric dynamics* `dyn10` *and* `dyn11` *respectively.*

In the code we implemented three different modules:

- `dyn10` is the Jupiter-centric dynamics of the Galilean satellites; the four moons are propagated all together, therefore the total state vector has dimension 24 (6 coordinates per satellite).
- `dyn11` is the Jupiter-centric dynamics of the spacecraft; it is used when the spacecraft is far from all the Galilean satellites, and their local perturbations are small.
- `dyn11x` ($x = 1, 4$) is the satellite-centric dynamics of the spacecraft; it is used when the spacecraft is close to the x-th Galilean satellite, and the local perturbations become important.

In Table 7.2 we reported a scheme of the accelerations we take into account in the different dynamics. Apart from implementing a precise dynamical model, we want that the switching between a Jupiter-centric dynamics of the spacecraft to a satellite-centric dynamics is as smooth as possible.

The accelerations that are considered only locally (i.e. only when the spacecraft is propagated in the satellite-centric frame) are: the harmonic expansion of the satellite's field, the satellite's tidal field, relativistic and non-gravitational effects due to the presence of the satellite. Apart from them, the motion of the spacecraft around Jupiter determined by `dyn11` is perfectly the same of the sum of `dyn11x` and

Effect	Parameter	dyn11	dyn10	dyn11x
Monopole	Gm_c	$\times$	$\times$	$\otimes$
Third-body direct	Gm_j	$\times$	$\times$	$\times$
Third-body indirect	Gm_j	$\bigcirc$	$\bigcirc$	$\bigcirc$
Jup gravitational field	C_{lm}, S_{lm}	$\times$	$\times$	$\otimes$
Gal gravitational field	C_{lm}, S_{lm}			$\times$
Indirect oblateness	C_{lm}, S_{lm}	$\bigcirc$	$\bigcirc$	
Jup point - Gal oblated	C_{lm}, S_{lm}		$\times$	$\bigcirc$
Jup tides	k_2	$\times$	$\times$	$\otimes$
Gal tides	k_2			$\times$
Tidal dissipation (*)	k_2/Q		$\times$	$\bigcirc$
Jup Relativity	Gm_0	$\times$	$\times$	$\otimes$
Gal Relativity	Gm_i			$\times$
Solar radiation	$\Phi_\odot, A$	$\times$		$\times$
Jup albedo	$\Phi_\odot, A, \overline{\alpha}$	$\times$		$\times$
Gal albedo	$\Phi_\odot, A, \overline{\alpha}$			$\times$
Jup thermal emission	Φ_{IR}, A	$\times$		$\times$
Gal thermal emission	Φ_{IR}, A			$\times$

Table 7.2.: Forces added in the models; Jup and Gal (abbreviation for Jupiter and Galilean satellite respectively) indicate the body which produces the effect. With $\times$ we indicate that the effect is direct, with $\bigcirc$ indirect, with $\otimes$ direct and indirect. (*) As we consider tidal dissipation on Io only, and we do not have flybys of Io, we did not added the indirect effect in dyn11x.

dyn10. We prove this statement taking the main terms of the dynamics: monopole, third-body perturbations and Jupiter's gravitational field.

Let be $\mathbf{r}_s$ the spacecraft's position in the Jupiter-centric frame, $\mathbf{r}_{is}$ in the satellite-centric frame and $\mathbf{r}_i$ the satellite's position in the Jupiter-centric frame, we want to prove that

$$\ddot{\mathbf{r}}_s = \ddot{\mathbf{r}}_{is} + \ddot{\mathbf{r}}_i. \tag{7.2}$$

We explicit the accelerations considering the mentioned forces. For $\mathbf{r}_s$ we have

$$\begin{aligned}\ddot{\mathbf{r}}_s &= -\frac{Gm_0\mathbf{r}_s}{r_s^3} + \sum_{j\neq 0}^{N} Gm_j\left(\frac{\mathbf{r}_{sj}}{r_{sj}^3} - \frac{\mathbf{r}_j}{r_j^3}\right)\\ &= -\frac{Gm_0\mathbf{r}_s}{r_s^3} + \frac{Gm_i\mathbf{r}_{si}}{r_{si}^3} - \frac{Gm_i\mathbf{r}_i}{r_i^3} + \sum_{j\neq 0,i}^{N} Gm_j\left(\frac{\mathbf{r}_{sj}}{r_{sj}^3} - \frac{\mathbf{r}_j}{r_j^3}\right).\end{aligned}$$

In the case of the satellite-centric frame

$$\begin{aligned}\ddot{\mathbf{r}}_{is} &= -\frac{Gm_i\mathbf{r}_{is}}{r_{is}^3} + \sum_{j\neq i}^{N} Gm_j\left(\frac{\mathbf{r}_{sj}}{r_{sj}^3} - \frac{\mathbf{r}_{ij}}{r_{ij}^3}\right)\\ &= -\frac{Gm_i\mathbf{r}_{is}}{r_{is}^3} - \frac{Gm_0\mathbf{r}_s}{r_s^3} + \frac{Gm_0\mathbf{r}_i}{r_i^3} + \sum_{j\neq 0,i}^{N} Gm_j\left(\frac{\mathbf{r}_{sj}}{r_{sj}^3} - \frac{\mathbf{r}_{ij}}{r_{ij}^3}\right).\end{aligned}$$

Finally, for the Galilean satellite

$$\ddot{\mathbf{r}}_i = -\frac{G(m_0+m_i)\mathbf{r}_i}{r_i^3} + \sum_{j\neq 0,i}^{N} Gm_j\left(\frac{\mathbf{r}_{ij}}{r_{ij}^3} - \frac{\mathbf{r}_j}{r_j^3}\right).$$

It is easy to see that, summing the last two equations, we obtain

$$\begin{aligned}\ddot{\mathbf{r}}_i + \ddot{\mathbf{r}}_{is} &= -\frac{G(m_0+m_i)\mathbf{r}_i}{r_i^3} + \sum_{j\neq 0,i}^{N} Gm_j\left(\frac{\mathbf{r}_{ij}}{r_{ij}^3} - \frac{\mathbf{r}_j}{r_j^3}\right)\\ &\quad - \frac{Gm_i\mathbf{r}_{is}}{r_{is}^3} - \frac{Gm_0\mathbf{r}_s}{r_s^3} + \frac{Gm_0\mathbf{r}_i}{r_i^3} + \sum_{j\neq 0,i}^{N} Gm_j\left(\frac{\mathbf{r}_{sj}}{r_{sj}^3} - \frac{\mathbf{r}_{ij}}{r_{ij}^3}\right)\\ &= -\frac{Gm_0\mathbf{r}_s}{r_s^3} + \frac{Gm_i\mathbf{r}_{si}}{r_{si}^3} - \frac{Gm_i\mathbf{r}_i}{r_i^3} + \sum_{j\neq 0,i}^{N} Gm_j\left(\frac{\mathbf{r}_{sj}}{r_{sj}^3} - \frac{\mathbf{r}_j}{r_j^3}\right),\end{aligned}$$

which proves (7.2). Therefore, the accelerations are equal and we can pass from a formulation to the other without any change in the motion.

For the gravitational field of Jupiter we have

$$\nabla_{r_s} U(\mathbf{r}_s) = \nabla_{r_i} U(\mathbf{r}_i) + \nabla_{r_s} U(\mathbf{r}_s) - \nabla_{r_i} U(\mathbf{r}_i),$$

where for the satellite-centric acceleration we have two components: the first is the direct term, acting on the spacecraft, while the second is the indirect term, due to the fact we are using a non-inertial frame.

For the other forces we have similar equalities, apart from the local forces that we consider in `dyn11x` only. The advantage of this approach is to consider these forces only when their contribution has a real impact on the orbit, i.e. when the spacecraft is close to the Galilean satellites (during the flybys for example), while we omit them when the probe is orbiting around Jupiter and is far from the moons.

The choice to switch the dynamics is suitable in the code for another reason: we can easily associate a different time step for each dynamics, so that for `dyn11x` (i.e. during the flybys) we will use a very short integration step, while during the orbiting phase we can relax it.

7.3.1 *Pseudo-orbit of the spacecraft*

Since we gave up the hope to obtain a whole orbit of the spacecraft during the flybys phase, for limitations in the computation, we have to make a different choice. If a whole orbit, given by the propagation of a single initial condition, is out of reach, then we can build something that seems it, whose difference from a real orbit is invisible to the observations' accuracy we are considering.

For this task, we take advantage of the theory presented in [46]. First we introduce the notion of pseudotrajectory: a δ-pseudotrajectory of a dynamical system Φ, is a sequence of points $\zeta = \{x_k\}_k$ such that it holds

$$d(\Phi(x_k), x_{k+1}) < \delta,$$

where d is the distance function of the space where Φ is defined. It means that a point of the pseudotrajectory is mapped by Φ in a neighbourhood of the following point of the sequence.

Generally, a pseudotrajectory is the result of numerical methods applied to obtain orbits of the dynamical system Φ. It is said that a point x ϵ-shadows a pseudotrajectory ζ if for every k it holds

$$d(\Phi(x)^k, x_k) < \epsilon.$$

Given the previous definitions, we have the following result:

Shadowing Lemma. *Let be Λ a hyperbolic set for a diffeomorphism Φ, then there exists a neighbourhood W of Λ such that for all $\epsilon > 0$ there exists $\delta > 0$ such that for any δ-pseudotrajectory with initial conditions $\zeta \in W$ there is a point x that ϵ-shadows ζ.*

In light of this theory, we can try to generate a pseudotrajectory for JUICE, instead of a real orbit. It is not straightforward to prove that the spacecraft's orbit belongs to a hyperbolic set; moreover, it is not even simple to compute the value of δ and ϵ. However, what is really important is that operatively this pseudotrajectory, called pseudo-orbit since we are in the context of celestial mechanics, is not something different from a real orbit, being the discrepancy much smaller than the accuracy of the observations.

For generating the pseudo-orbit, we can patch single arcs at the conjunction times between the flybys. The dynamical models we use are very elaborated, therefore, we cannot just perform a patch of conic curves, as for example hyperboles and ellipses in the case of simplified models. This is useful for the initial design of the mission, but we need something more sophisticated.

We want to link the arcs of the flybys phase (23 in total, therefore 22 connections), at a level that the observations cannot see the jumps between them; for example at a level of almost 2 order of magnitude smaller than the accuracy of range and

Linked arcs	Distance (days)	$\|\mathbf{d}\|$ position (10^{-1} cm)	$\|\mathbf{d}\|$ velocity (10^{-6} cm/s)
1-2	214.68	4.06	0.16
2-3	57.21	0.20	0.01
3-4	38.30	0.38	0.09
4-5	21.46	0.12	0.06
5-6	13.82	0.03	0.02
6-7	14.24	0.12	0.33
7-8	11.75	0.06	0.04
8-9	21.50	0.29	0.07
9-10	39.54	1.45	1.13
10-11	16.69	0.10	0.05
11-12	16.68	0.02	0.01
12-13	16.68	0.11	0.05
13-14	83.44	0.24	1.12
14-15	16.68	0.20	0.09
15-16	16.68	0.05	0.01
16-17	16.68	0.08	0.04
17-18	16.66	0.13	0.05
18-19	18.38	0.02	0.01
19-20	35.76	0.70	0.58
20-21	16.36	0.04	0.01
21-22	17.02	0.05	0.01
22-23	59.24	0.47	0.19

Table 7.3.: Jumps in the flybys' extended arcs with the computed pseudo-orbit.

range-rate observations. This means a jump of 10^{-1} cm in position and 10^{-6} cm/s in velocity. For this task, we apply the constrained multi-arc strategy. Our objective is to find new values for the local initial conditions in such a way that the jumps are reduced to the mentioned level.

In fact, we cannot use initial conditions from the SPICE kernel, propagate them and hope to find a perfect linkage. Actually, the difference can be also some hundreds of kilometers for the couples of flybys more distant. Moreover, as described in Chapter 6, we have to take into account the manoeuvres, both the ones present in the mission plan and the ones we added. Therefore, in this preliminary step, we start with 23 initial conditions (one per flyby), taken from the SPICE kernel, and to default values for the manoeuvres. Then we perform the differential corrections in order to reach jumps at the connection times smaller than the level we fixed.

The result of this procedure is presented in Table 7.3 and 7.4. In the first table we can appreciate how the jumps are very below the order we demanded, with only few cases of the order of 10^{-1} cm and 10^{-6} cm/s. In the second table we reported the differences between positions and velocities of the new initial conditions and the SPICE kernel. In most of the cases the change is smaller than 10 km, sometimes smaller than 1 km; in just two flybys we find a variation greater than 10 km (23 and 36 km respectively), which compared to the distance of thousands of kilometers

Flyby	Target Body	Position (cm)	Velocity (cm/s)
1	Ganymede	536	1
2	Ganymede	432766	124
3	Ganymede	225071	79
4	Ganymede	2381474	409
5	Ganymede	3656631	399
6	Europa	38592	39
7	Europa	80533	28
8	Callisto	124652	24
9	Ganymede	252149	110
10	Callisto	167594	50
11	Callisto	286078	29
12	Callisto	35018	13
13	Callisto	71560	23
14	Callisto	33580	66
15	Callisto	23275	54
16	Callisto	73337	41
17	Callisto	611216	88
18	Callisto	53520	23
19	Ganymede	200866	27
20	Ganymede	386355	29
21	Ganymede	17162	23
22	Callisto	133052	72
23	Callisto	262786	97

Table 7.4.: Changes in the initial conditions with respect to the SPICE kernel. For the first flyby we have a very small shift, since the JOI manoeuvre is just few hours later and the correction affects mainly the manoeuvre.

to the moon's center of mass or hundreds to the moon's surface, does not disrupt the plan of the mission.

Unfortunately, this step must be performed each time we modify the dynamical models, as any small change brings to jumps greater than the level we demand. However, we do not need to start from the SPICE kernel's initial conditions every time, but, as the modification is generally small, we can take as first guesses the previously calculated initial conditions.

We can try to pass from the computed pseudo-orbit to a whole single orbit, in light of the small jumps presented in Table 7.3. In Figure 7.5 we show an attempt to generate the whole orbit of the spacecraft, starting with one of the new initial conditions we found with the described method. We can see that, even if the difference in the first jump is below the level of the centimeter, after four flybys (both forward and backward, counting also the flyby at the initial condition of the spacecraft) the spacecraft misses the other close encounters of the moons and its orbit becomes completely different from the planned tour. The divergence we found is in agreement with the computation horizon we presented in Figure 7.3.

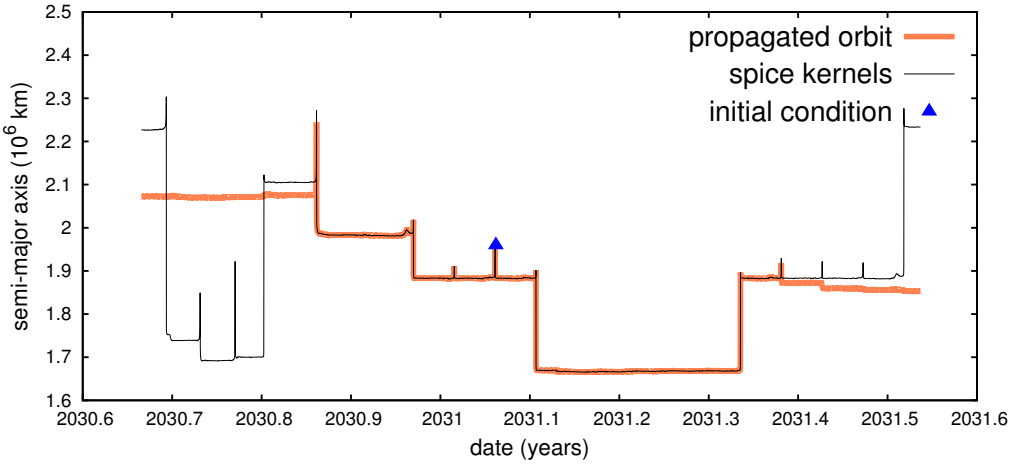

Figure 7.5.: *Orbit of JUICE during the flybys phase: with the black line as given by the SPICE kernel, with the coral line as computer in the attempt to recover the whole orbit from a single propagation. The accordance with the mission's plan lasts for few flybys, then the orbit changes completely.*

7.4 DESCRIPTION OF THE MAIN PROGRAMS

Once we obtain the new local initial conditions $\mathbf{X}_{sc}^{(k)}$ $(k = 1, n)$ that provide the pseudo-orbit of the JUICE mission, we have all the elements we need to perform the orbit determination experiments. In this section we give the details about the main programs `js_sim` and `js_cor` we implemented for the processing of the JUICE mission data.

In the simulator `js_sim` we take the initial conditions of the spacecraft for each arc; for the flybys they are the new computed states, while for the arcs of the Ganymede orbiting phase we can take the states from the SPICE kernel. From the time of the first arc to the time of the final one, we have approximately the time span of the mission. For this interval of almost 4 years, we need the positions of the planets and the Jovian satellites, which intervene in the propagation of the probe. Apart from the Galilean satellites, we propagate also the BJS, Saturn, Uranus and Neptune. All the other bodies are taken from the corresponding ephemerides.

The task of the simulator is to generate the observations, therefore, we can integrate the spacecraft's motion just during the tracking sessions. The duration of the tracking is almost 8 hours, therefore, we integrate JUICE for 4 hours forward and 4 hours backward from the initial time, taken at the pericenters of the flybys or at an arbitrary time for the other arcs.

From the numerical propagation and the ephemerides we get all the state vectors we need for the computation of the observations, using the mathematical models defined in the prediction functions (6.19), (6.21) and (6.22). We create

a list of observations' times: for the range-rate we consider an interval of 30 s between one observation and the other, with a consequent 2-way accuracy of $\sqrt{1000/30} \times 3 \times 10^{-4} \approx 1.7 \times 10^{-3}$ cm/s, while for range and VLBI 300 s, with an accuracy of $\sqrt{1000/300} \times 20 \approx 36$ cm and 10^{-10} radians respectively. This makes 1076 observations per arc, if there is not any interruption of visibility: 827 range-rate observations, 83 range and 166 VLBI (right ascension and declination). Since we want to simulate realistic data, we add a Gaussian noise to the simulated observables, with mean 0 and standard deviation equal to the accuracy of the measurements.

Finally, we prepare output files that will be handled by the corrector. We store the simulated observations, the values of the parameters and the initial conditions of the different bodies, in order to have suitable input files for the second program.

The corrector `js_cor` takes all these information and prepare the setting up for the differential corrections. First, we choose the fit parameters $\mathbf{x}$ and we save the values we used in the simulator in the vector of the true parameters $\mathbf{x}_T$. For the iterative process we need a first guess $\mathbf{x}_0$ for the values of the fit parameters. We can decide to begin directly from the true values $\mathbf{x}_0 = \mathbf{x}_T$ or we can decide to add systematic errors in the correction, starting with different values.

Just like in the simulator, we have to propagate the planets, the Galilean satellites and the spacecraft, in order to have their states for the computation of the observations. Moreover, since we need the values of the various partial derivatives $\partial\mathbf{X}/\partial c$, we have to integrate the variational equation (6.4). It is worth noting that, if c is an unknown parameter that intervene both in the spacecraft and Galilean satellites' dynamics, the derivative of the target function R is

$$\frac{\partial R}{\partial c} = \frac{\partial R}{\partial \mathbf{X}_{sc}} \frac{\partial \mathbf{X}_{sc}(t)}{\partial c} + \frac{\partial R}{\partial \mathbf{X}_{gs}} \frac{\partial \mathbf{X}_{gs}(t)}{\partial c}.$$

Moreover, since the spacecraft dynamics depends on the Galilean satellites' states, for the partial derivatives of the spacecraft's acceleration we have to consider two terms:

$$\frac{\partial \dot{\mathbf{X}}_{sc}}{\partial c} = \frac{\partial \dot{\mathbf{X}}_{sc}(t)}{\partial c} + \frac{\partial \dot{\mathbf{X}}_{sc}}{\partial \mathbf{X}_{gs}} \frac{\partial \mathbf{X}_{gs}(t)}{\partial c}.$$

Therefore, if we propagate the spacecraft also outside the tracking sessions, we need to store the values of the partial derivatives of the moons for the whole length of the mission, with a hard occupation of computer memory. In fact, the number of the variables is not just the sum of the dimension of the states, but it must be multiplied by the number of the fit parameters. In the case of JUICE, the number of the fit parameters is quite large, therefore, the orbit determination problem has a very big dimension.

Since we use a constrained multi-arc strategy, we propagate the spacecraft for very long times, at least during the flybys phase. The propagation must be con-

tinued until the conjunction time between the arcs: for this reason, though in the simulator the arcs' length was just few hours, in the corrector we have extended arcs that can be longer than 100 days.

Once we have the simulated and calculated observables, we can make the difference and obtain the residuals. The target function (6.16) is the sum of the normalized residuals, divided by the number of the observations, plus the part due to the jumps.

Following the theory presented in Chapter 6, we apply the differential corrections for the least squares method. We compute the design matrix B, the normal matrix C and we invert it in order to solve the correction step (6.10). In this way, we obtain the covariance matrix Γ, with the uncertainties and the correlations between the fit parameters, and new values for $\mathbf{x}$, that will be used in the following iteration of the method.

We stop the iterative method at convergence and we save the last values obtained. In Chapter 8, we will present an analysis of the orbit determination's results.

7.5 SETTING UP OF THE EXPERIMENTS

Each flyby is a great occasion to obtain information about the Galilean satellites; moreover, their extension in time allows to investigate effects whose contribution increases most with time, such as the tidal dissipation. For these reasons, in order to get as much information as possible, in the following experiments we consider both radioscience and VLBI data for all the flybys.

Apart from these first 23 arcs, we must define a observations' plan during the Ganymede orbiting phase. In [17], the radioscience experiment is scheduled each day of the mission. This means almost other 280 8-hours tracking arcs; not for all of them we can consider VLBI observations, since this technique is much more expensive than the tracking. Following [8], we fix a VLBI session a day every ten.

In this section we define all the necessary elements for running the experiments.

7.5.1 *Fit parameters*

Following the requirements of the mission we presented at the beginning of this chapter, and taking into account the effects introduced into the dynamics, we consider the following fit parameters:

- initial conditions of the spacecraft for each arc (6 coordinates per 300 arcs);
- manoeuvres (3 coordinates per 23 manoeuvres);
- initial conditions of the BJS (6);

- initial conditions of the Galilean satellites (24);
- masses of Europa, Ganymede and Callisto (3);
- gravitational field of Europa, only $C_{20}^{(2)}$, $C_{22}^{(2)}$ (2);
- gravitational field of Callisto up to degree 3 (13);
- gravitational field of Ganymede up to degree 10 (117);
- mass of Jupiter (1);
- gravitational field's parameter J_l ($l = 2, 6$) of Jupiter (5);
- k_2 of Europa, Ganymede and Callisto, k_3 and k_4 of Ganymede (5);
- dissipative parameters k_2/Q of Jupiter and Io (2).

Considering one set of initial conditions and one manoeuvre, the total dimension of the vector $\mathbf{x}$ of the fit parameters is 187, where the first two points of the list refer to local parameters, while the others to global parameters. For some of them we will consider apriori observations which will help the inversion of the normal matrix. Actually, we are not interested in all the parameters of the list. For example, the gravitational field of Jupiter will be studied extensively by the Juno mission and it is not an objective of JUICE. However, we want to consider their contribution to the uncertainties of the other parameters.

Also the mass of Io and its gravitational coefficients $C_{20}^{(1)}$ and $C_{22}^{(1)}$ should be included in the list, because of their important role in the Galilean dynamics. However, due to the fact that the spacecraft will not perform any flyby of the moon, in this first preliminary study we decided not to add them in the fit parameters. Differently from the same coefficients of the other satellites, the most of the information of these parameters we can obtain with JUICE data comes from their effect on the orbits of the other moons. For this reason, we choose not to solve for any physical parameters of Io (except k_2/Q) and to leave for a future analysis a more complete study including them, as well as the parameters describing the rotation of the moons (such as the pole direction).

Moreover, another important task will be to introduce the dissipative effects for all the Galilean satellites. In this way we could try to estimate the dissipative parameters of the other moons and the one of Jupiter for each of their orbital frequencies, as done in [25] for the Saturn system. However, since the tidal dissipation in the couple Io-Jupiter is far greater than for the other moons and it is also spread to Europa and Ganymede, it could be not easy to separate the various similar effects, with a consequent presence of rank deficiencies in the orbit determination.

Parameter	Body	Uncertainty	Reference
ΔC_{00}	Europa	6.2×10^{-6}	Galileo mission and others [15]
C_{20}	Europa	8.2×10^{-6}	Galileo mission [41]
C_{22}	Europa	2.5×10^{-6}	Galileo mission [41]
ΔC_{00}	Ganymede	3.0×10^{-6}	Galileo mission and others [15]
C_{20}	Ganymede	2.9×10^{-6}	Galileo mission [41]
C_{22}	Ganymede	0.9×10^{-6}	Galileo mission [41]
ΔC_{00}	Callisto	1.4×10^{-6}	Galileo mission and others [15]
C_{20}	Callisto	0.8×10^{-6}	Galileo mission [41]
C_{22}	Callisto	0.3×10^{-6}	Galileo mission [41]
ΔC_{00}	Jupiter	1.6×10^{-8}	Juno mission [14]
J_2	Jupiter	1.4×10^{-8}	Juno mission [14]
J_3	Jupiter	1.0×10^{-8}	Juno mission [14]
J_4	Jupiter	0.4×10^{-8}	Juno mission [14]
J_5	Jupiter	0.8×10^{-8}	Juno mission [14]
J_6	Jupiter	0.9×10^{-8}	Juno mission [14]
$\mathbf{x}_{gs}$	Galilean satellite	100 km	L3 Ephemerides
$\dot{\mathbf{x}}_{gs}$	Galilean satellite	10 m/s	L3 Ephemerides

Table 7.5.: Apriori uncertainty of some fit parameters.

It is worth noting that the simplest way to proceed would be to estimate the gravitational field of Ganymede, considering just the orbiting phase around the moon. Then we can use its coefficients as known quantities and we omit them in the fit parameters once we process the data of the whole mission. However, since we want to show that a complete inversion of the data is possible, we consider all the parameters together.

7.5.2 *Apriori knowledge*

The Jupiter's system has been widely explored during the last century, both thanks to astrometric observations and previous space missions. The Galileo mission had the opportunity to perform some flybys of the moons, from which it was determined the masses of the moons and their gravitational coefficients C_{20} and C_{22}. The uncertainties for these parameters are taken from [15] and [41]. Their values and the ones of the other parameters we consider in this paragraph are reported in Table 7.5.

Moreover, Juno mission is already providing extraordinary results about the gravitational field of Jupiter, as presented in [14]. The current estimation for the zonal coefficients is of the order of 10^{-8}. We add these information to the normal matrix.

Finally, from past observations moons' ephemerides were computed, with a nominal accuracy of tens of kilometers for the satellites as stated in L3 ephemerides.

Obs.	Time	Target body	Distance (km)
1	11-23-2030	Io	9.7×10^5
2	01-29-2031	Io	9.1×10^5
3	03-24-2031	Io	8.7×10^5
4	06-10-2031	Io	8.7×10^5
5	08-06-2031	Io	8.2×10^5
6	09-19-2031	Io	4.9×10^5
7	12-16-2031	Io	8.8×10^5
8	02-07-2032	Io	9.6×10^5
9	04-07-2032	Io	9.0×10^5
10	06-26-2032	Io	8.1×10^5

Table 7.6.: Selected JANUS observations.

This apriori uncertainty is greater than the formal uncertainties we will obtain for the Galilean satellites' initial conditions with JUICE, but, although they will contribute poorly to the estimation, they will anchor these states at their true values once we add systematic errors.

7.5.3 *Scheduling of camera and astrometry observations*

Since we do not have direct observations of Io, but the information about its state is contained just in the orbits of the other moons, we have to deal with a weak determination. This lack of information brings to inversion problems, which, following [8], can be solved with the addition of new observations. In Chapter 5 and Chapter 6 we presented camera and astrometric observations: their main motivation and contribution is to stabilize the estimation of Io's orbit.

For ground based astrometry we consider two observations session every year; each session corresponds to two days where right ascension and declination of all the four moons are captured, for a total of 16 observations (2 couples per moon). Their contribution is quite limited, due to their poor linear accuracy, at least with respect to the other kinds of observations.

For JANUS observations we take a list of 10 observations times for which Io is in a suitable position for the acquisition of astrometric picture with the camera. No one of the considered times is contained in the time span of the Ganymede orbiting phase, since it is supposed that JANUS will observe the icy moon. In particular, 6 observations are taken during the flybys phase, far from the close encounters, and the other 4 during the empty period between the two main phases of the mission. In Table 7.6 we reported the ten observations, with the related time and the distance from the target body. As the nominal precision of the camera is set to 10^{-5} radians, the linear accuracy is between 5 and 10 kilometers. Although it is

Linked arcs	$\partial x_l/\partial \dot{x}_0$	$\partial y_l/\partial \dot{y}_0$	$\partial x_r/\partial \dot{x}_0$	$\partial y_r/\partial \dot{y}_0$
1-2	-6999.3	-36623.3	5392.4	-20266.6
2-3	-1004.9	-4285.2	1483.6	-2876.1
3-4	-542.3	-2496.5	-996.9	960.1
4-5	266.7	1108.1	-480.6	438.2
5-6	205.1	489.9	34.3	4.4
6-7	14.5	-69.2	34.6	-1.9
7-8	14.7	-63.8	-115.7	30.8
8-9	381.1	-6.4	152.5	-774.4
9-10	1111.0	1592.0	-945.8	-102.7
10-11	-149.2	-39.2	188.3	-2.6
11-12	-124.8	-36.9	162.7	1.0
12-13	-93.9	-34.3	124.8	3.7
13-14	31.4	106.1	-35.7	-55.6
14-15	-49.6	-18.9	61.6	1.9
15-16	-52.1	-16.3	60.6	0.3
16-17	-46.9	-13.6	51.1	-0.7
17-18	-38.4	-11.0	39.0	-1.0
18-19	-29.6	-8.4	18.1	-29.1
19-20	86.7	-108.9	28.6	-25.7
20-21	4.3	6.4	15.6	-12.9
21-22	7.9	-70.4	-0.9	3.5
22-23	-32.1	5.8	-53.6	27.1

Table 7.7.: Values (to be multiplied by 10^6) of some partial derivatives of the spacecraft's state at the time of the jumps. In particular, x_l and y_l(respectively x_r and y_r) are two coordinates of the spacecraft at the conjunction time obtained from the initial conditions of the left arc (respectively right), while $\dot{x}_0$ and $\dot{y}_0$ are two initial conditions' components of the primary moon.

larger than in the case of range measurements, the camera's observations will be of great value in the orbit determination.

7.5.4 *Control on the jumps*

As we showed in the critical issues of the JUICE mission, the uniform accuracy required for 4 years of the mission is very small, and some problems arise from the limitations of machine computation. An example is the control on the moons' states for times far from the initial conditions: we showed that a change of the order of the machine error in the initial state of the moons leads to a non-negligible variation in the residuals.

The same issue affects the jumps of the spacecraft's orbit. As presented in the previous sections, we computed an initial pseudo-orbit in such a way that the jumps between the extended arcs are at the level of 10^{-1} cm and 10^{-6} cm/s. In the target function we would add a constraint to the jumps of the level of the

radioscience observations' accuracy, i.e. 10 cm and of 10^{-3} cm/s. In this way at the end of the correction we would find again a pseudo-orbit with a uniform and strict bound, at least smaller than the nominal accuracy of the observations. However, this is not straightforward; in fact, in the case we solve for parameters involved in the Galilean satellites' dynamics (such as their initial conditions or the dissipative parameters), we do not have the control on the jumps we desire. As shown in Table 7.7, for the flybys furthest from the moons' initial conditions, a change of δ in the velocity of the primary moon's initial conditions can lead to a change of more than $10^{10}\delta$ in the position of the spacecraft at the time of conjunction. This means a control on the jumps of the order of 10 cm for the furthest flybys. The same computation can be done for the velocities. The requested level of control is too strict and it undermines the convergence of the differential corrections, therefore we have to relax it.

This divergence of some partial derivatives of the spacecraft state occurs when we estimate simultaneously the initial conditions of the spacecraft and of the Galilean satellites. In this case, the chaotic effects on the spacecraft are amplified by a change in the state of the primary satellite at the time of the flyby. In fact, moving the position of the moon during the flyby, is like shifting the spacecraft itself. This change of position is not just at the level of machine error, but far greater, since it is propagated from the time of the moons' initial conditions (see Figure 7.1). For this reason the jumps associated to flybys further from the initial state of the satellites are the ones with the larger divergence, as clear from the values of Table 7.7.

We adopt the apriori constrained multi-arc approach presented in [1] with a small modification: we choose a fixed weight matrix

$$C^{j,j+1} = \begin{bmatrix} 1 & 0 & 0 & 0 & 0 & 0 \\ 0 & 1 & 0 & 0 & 0 & 0 \\ 0 & 0 & 1 & 0 & 0 & 0 \\ 0 & 0 & 0 & 10^8 & 0 & 0 \\ 0 & 0 & 0 & 0 & 10^8 & 0 \\ 0 & 0 & 0 & 0 & 0 & 10^8 \end{bmatrix},$$

while we define the penalty parameter μ in such a way that it depends on the number of the iteration and on the flybys we are considering. In the case $\mu = 1$, since in (6.16) $C^{j,j+1}$ defines a quadratic form in the jumps, it would follow that we demand jumps of the order of 1 cm and 10^{-4} cm/s, a bound too strong as we explained. For the first iterations we define softer weight matrices, in order not to demand a too strict constraint abruptly, while for the following iterations we increase the contribution of the jumps in the target function. In light of the values reported in Table 7.7, we implement an empirical non-uniform constraint of the jumps. We divide them in three groups: the first one comprehends just the first

jump, the second group is composed by the jumps number 2, 3, 4, 5, 8 and 9, while the others form the last group. For the first group, which is the furthest from the initial conditions' time of the Galilean satellites, we define μ equal to 10^{10} for the first iteration, 10^8 for the second iteration, and 10^6 for the following iterations. For the jumps of the second group, following the same strategy, we fix μ equal to 10^8, 10^6 and 10^4, while for the others 10^6, 10^4 and 10^2. Finally, we are demanding jumps in position of the order of ten meters (first group), 1 meter (second) and 10 centimeters (third).

Unfortunately, these values take us away from the concept of pseudo-orbit we defined in the previous sections. In fact, if in simulation we have jumps invisible from the observations, in correction we demand and we find jumps greater than the range and range-rate accuracy. This is done to ensure the convergence of the differential corrections. What we obtain at the end of the correction is not a pseudo-orbit, because of the lack of a small uniform bound on all the jumps, but 23 arcs whose differences at the conjunction times increase when we move away from the initial time. However, although this is a theoretic issue which shows the limitation of the procedure for a complicated scenario like the one of JUICE, it does not have a dramatic impact in the orbit determination experiments. Apart from the first jump, which is very distant both in space (from Jupiter, because of the very eccentric initial orbit) and in time (from the two involved flybys), we have a uniform bound on the other jumps at least of the order of the meter, which is not so different from the initially requested values. Moreover, for what concerns the observations and the residuals, this non-uniform treatment of the jumps does not have repercussions. In fact, as we will show in the next chapter, we manage to fit the data at the level of the noise for all the flybys, meaning that also with a weaker constraint on the jumps we obtain good results.

As we already mentioned, in [42] the authors showed that the constrained multi-arc do not improve the estimation of the dynamical parameters when we are in ordered regions; therefore, for the arcs of the Ganymede orbiting phase, we do not apply the constrained multi-arc, or equivalently $C^{j,j+1} = 0$ for $j > 23$.

7.5.5 *Systematic errors*

As we noted in the previous section, if we start with $\mathbf{x}_0 = \mathbf{x}_T$, the residuals will contain only the Gaussian noise added to the simulated observables. In this case, the target function would start close to 1 and the differential corrections will bring to a minimum whose value is generally slightly below the initial one.

It is interesting to see the response of the differential corrections when we add some sources of errors. Apart from the Gaussian noise on the simulated observables, for our experiments we choose to consider systematic errors, taking first guesses such that $\mathbf{x}_0 \neq \mathbf{x}_T$. This is the case of real experiments, where we do

not know which are the true values of the parameters and we start from the best approximation we have.

Since we are mostly interested in the determination of the Galilean satellites' states and the dissipative parameters, we perform tests for which only the initial guesses of these parameters are different from their true values. For the Galilean satellites' positions we will add to each component a random quantity with standard deviation equal to 100 meters, while for their velocity 10^{-1} cm/s. They seem very small changes, and in fact they are, but we must remember that the accuracy of the measurements is 10^2-10^3 times smaller and that we propagate these states for almost 2 years. From Table 7.1 we know that a change of 10^{-1} cm/s in $\dot{y}_0$ of Ganymede leads to an initial error in $y(t)$ of 100 kilometers in the first flyby, and we can verify that the same happens for a change of 100 meters in position.

Instead, for the dissipative parameters, we start from a first guess equal to 0, and we want to see if the method converge to their true values, set to 0.015 and $1.1 \cdot 10^{-5}$ respectively.

Because of these systematic errors, the target function will have an initial value of the order of 10^{10}-10^{11}. In Chapter 8, we will see how the differential corrections bring Q at the level of the observations' precision.

7.5.6 *Convergence criteria*

As we mentioned in the previous sections, the convergence of the differential corrections suffer the strict control we demand for the whole length of the mission. From the simulations, we find that once we arrive at the level of the noise, the order of the fit parameters' variation $|\Delta \mathbf{x}|_C$ does not change and they move around the minimum of Q.

For this reason we relax the convergence criteria, also in light of the systematic errors which makes the target function begin from a value very distant from 1. Following the notation of Chapter 6, in our experiments we consider the differential corrections convergent if one of the two following conditions occurs:

- the norm of the change in the fit parameters is less than $\epsilon_x = 5 \times 10^{-1}$;
- the target function changes less than $\epsilon_q = 3 \times 10^{-3}$ for $n_q = 2$ consecutive iterations.

In Chapter 8, we will show the value of the target function for all the iterations, in order study the convergence speed.

8 RESULTS

In this chapter we present the results we obtain with the orbit determination experiments we described in Chapter 7, in particular we report the formal uncertainties (1-σ) and the true errors of the fit parameters we find at the convergence of the differential corrections. We perform ten experiments (Ei, $i = 1, 10$), using all the times different random seeds both for simulation and correction, in order to verify that the differential corrections converge for various systematic errors of the order we fixed.

In Table 8.1 we reported the random quantities added to the true values of the Galilean satellites' initial conditions, in order to start with a non-trivial first guess $\mathbf{x}_0$. For the same reason, as we already mentioned, we take 0 as first guess for the dissipative parameters.

Because of the wide time span we consider, the number of the arcs and the great number of fit parameters we solve for, the computation time is very large: the corrector takes some hours per iteration. In particular, the propagation of the moons for the time of the whole mission and the propagation of the spacecraft outside the tracking sessions, especially for the furthest flybys, are the parts of the processing that require more time. Moreover, since we store the Galilean satellites' states and partial derivatives for each step of their integration, the occupation of the RAM is an issue we have to pay attention to. For the future, it will be necessary to change some strategies in the code, starting with a parallelized computation for different arcs.

From Table 8.2 we can appreciate how, after the first iteration of the differential corrections, the target function decreases abruptly. It means that the iterative process moves rapidly the parameters toward a minimum of Ω. We note that in the third iteration the value of Ω can increase: this is due to the change of the jumps' weight matrices, whose values are greater than in previous iterations. Starting with an initial value of Ω of the order of 10^{10}-10^{11}, we need between 8 and 10 iterations to arrive at convergence, apart from E1 which is more rapid. For all the experiments the final value of the target function is below the level of the noise, which is almost 1, meaning that we arrived near the nominal minimum of the problem. Apart from experiments E3 and E8, the convergence is determined by the small correction of the parameters in the last iteration, below the tolerance's value 0.5. It is worth noting that, because of the convergence issues we presented

Coord.	E1	E2	E3	E4	E5	E6	E7	E8	E9	E10
x_1	0.19	-0.07	-1.19	1.61	1.72	-1.09	-0.65	-0.10	-0.27	-0.22
y_1	-0.86	0.00	0.19	-0.58	1.72	-1.33	0.81	0.24	-0.10	-0.80
z_1	0.05	-0.08	-0.91	0.81	0.69	0.64	-0.51	0.22	1.16	-1.39
x_2	-0.24	-0.44	1.81	-0.03	-1.39	0.06	-0.22	-0.01	-0.99	-0.32
y_2	-0.30	0.97	-0.80	1.43	1.40	-0.96	-0.34	-0.95	-0.00	-0.49
z_2	2.28	-0.39	-0.71	2.19	-0.95	-2.19	0.78	-0.16	1.17	-0.24
x_3	-0.40	-1.67	0.91	0.25	-0.89	-0.79	-1.05	0.20	1.21	-2.12
y_3	-0.80	0.98	1.68	-0.03	1.35	-0.25	0.25	0.09	-2.97	0.77
z_3	-0.57	-0.33	-1.18	0.65	-0.32	-0.91	-0.21	1.58	-0.20	-0.04
x_4	0.61	-0.68	0.12	0.25	1.92	-0.15	-0.05	-0.22	1.11	-0.75
y_4	0.58	-0.11	-0.72	-1.63	-1.86	-0.75	-0.55	0.66	-0.47	0.69
z_4	1.11	0.51	-1.24	-1.52	-0.25	0.80	-0.82	0.49	0.37	1.91
$\dot{x}_1$	0.76	-0.02	0.67	0.65	-2.15	-1.33	-0.96	0.95	0.92	0.58
$\dot{y}_1$	0.03	0.03	0.65	0.31	0.00	0.49	0.21	-1.73	-0.70	1.75
$\dot{z}_1$	0.75	-0.55	0.85	1.76	1.58	1.42	-1.11	-0.70	-0.46	-0.67
$\dot{x}_2$	-0.81	0.01	-0.93	-0.89	0.99	-1.72	0.53	-0.21	1.62	0.14
$\dot{y}_2$	1.08	0.89	0.07	-0.32	0.63	-0.19	1.51	-0.19	2.81	-0.55
$\dot{z}_2$	0.68	0.92	-0.52	-0.74	0.12	-2.26	-0.35	-0.99	0.38	1.87
$\dot{x}_3$	1.53	-0.91	-1.12	0.20	0.75	-1.17	1.17	0.50	0.58	0.68
$\dot{y}_3$	-1.39	-1.73	-1.31	-0.96	-2.24	-0.09	0.40	-1.23	1.58	-0.05
$\dot{z}_3$	0.50	0.86	-0.21	0.82	-0.22	-0.19	-1.38	0.25	-0.88	-1.46
$\dot{x}_4$	1.30	-0.70	0.14	0.03	1.09	-0.81	1.44	-0.51	-0.85	0.69
$\dot{y}_4$	-0.29	-0.47	0.29	0.16	2.04	-0.58	-1.42	-0.55	0.37	-0.76
$\dot{z}_4$	2.16	-1.05	-1.27	1.65	-1.97	2.09	-0.28	-0.18	0.32	0.86

Table 8.1.: Systematic errors for each component of the initial vector state of the Galilean satellites (units of measure 100 meters for the position and 10^{-1} cm/s for the velocity). For every experiment Ei ($i = 1, 10$) we have different values.

in Chapter 7, if we continued the iterative process, the value of the target function would begin to oscillate around its minimum value and $\mathbf{x}$ would move around the nominal solution. A hint of this behaviour can be found in experiments E3 and E8, for which the convergence is given by the stabilization of the value of Q.

It is interesting to compare Table 8.1 and 8.2, in order to verify the effect of the systematic errors on the different simulations. The experiments with a bigger initial value of Q are the ones with a greater error in the initial conditions of Ganymede, in particular for the components x, y, $\dot{x}$ and $\dot{y}$. This is due to the fact that Ganymede's state is involved in most of the arcs and that the motion takes place mainly on the xy plane and a change in these components is amplified quickly.

Although we use non-uniform constraints on the jumps between the flybys, we manage to obtain uniform results on the residuals of all the arcs. In Figure 8.1, 8.2 and 8.3 we reported the residuals obtained at convergence; in order to compare together the residuals of the different kinds of observations, we normalized them dividing for their weight. All the points are at the level of the noise, meaning

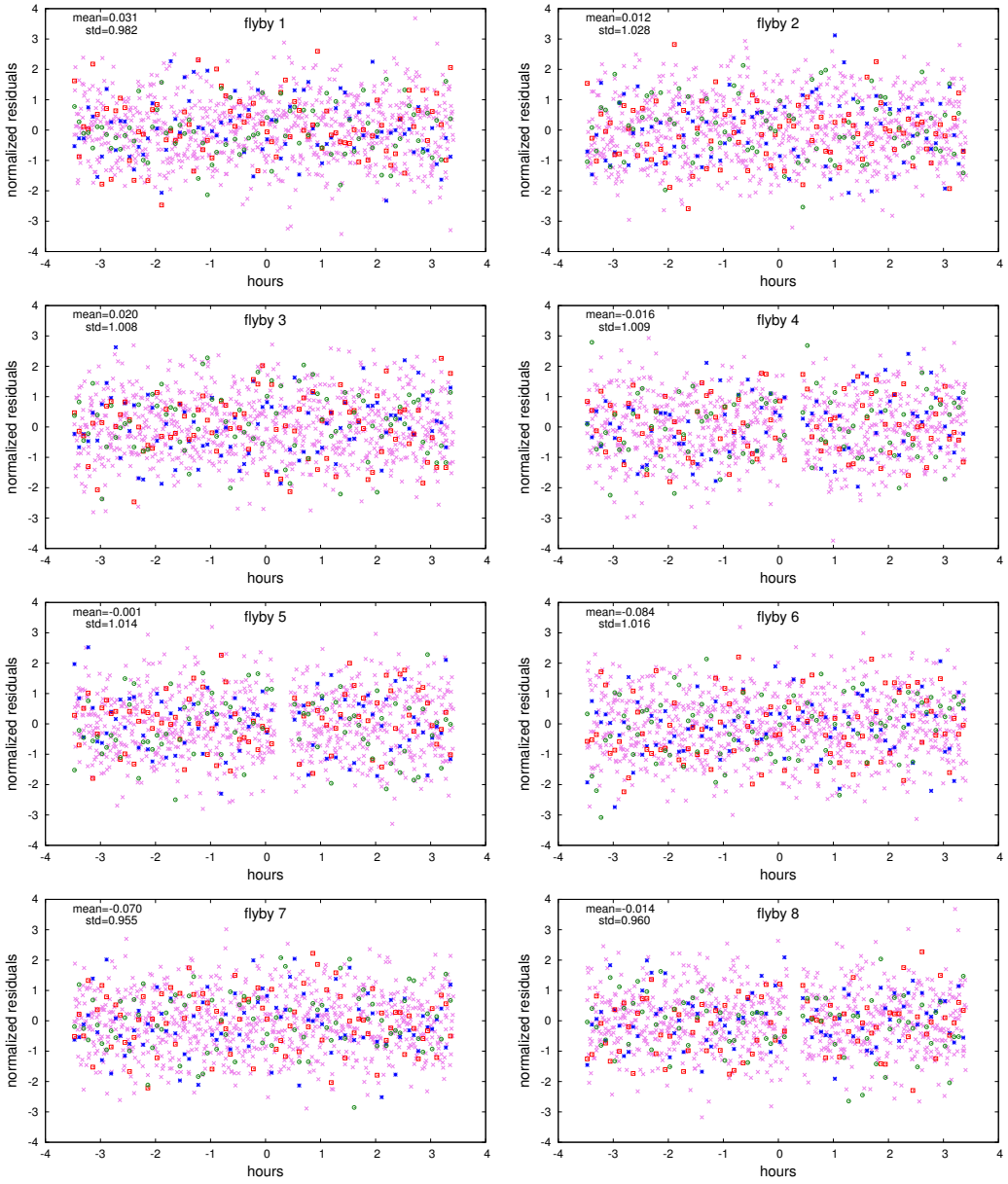

Figure 8.1.: *Normalized residuals of the first eight flybys. The violet crosses are the residuals of range-rate observations, blue asterisks for range, red squares and green circles for VLBI (right ascension and declination respectively). The residuals are taken at the last iteration of the differential corrections of the experiment E5 reported in the tables.*

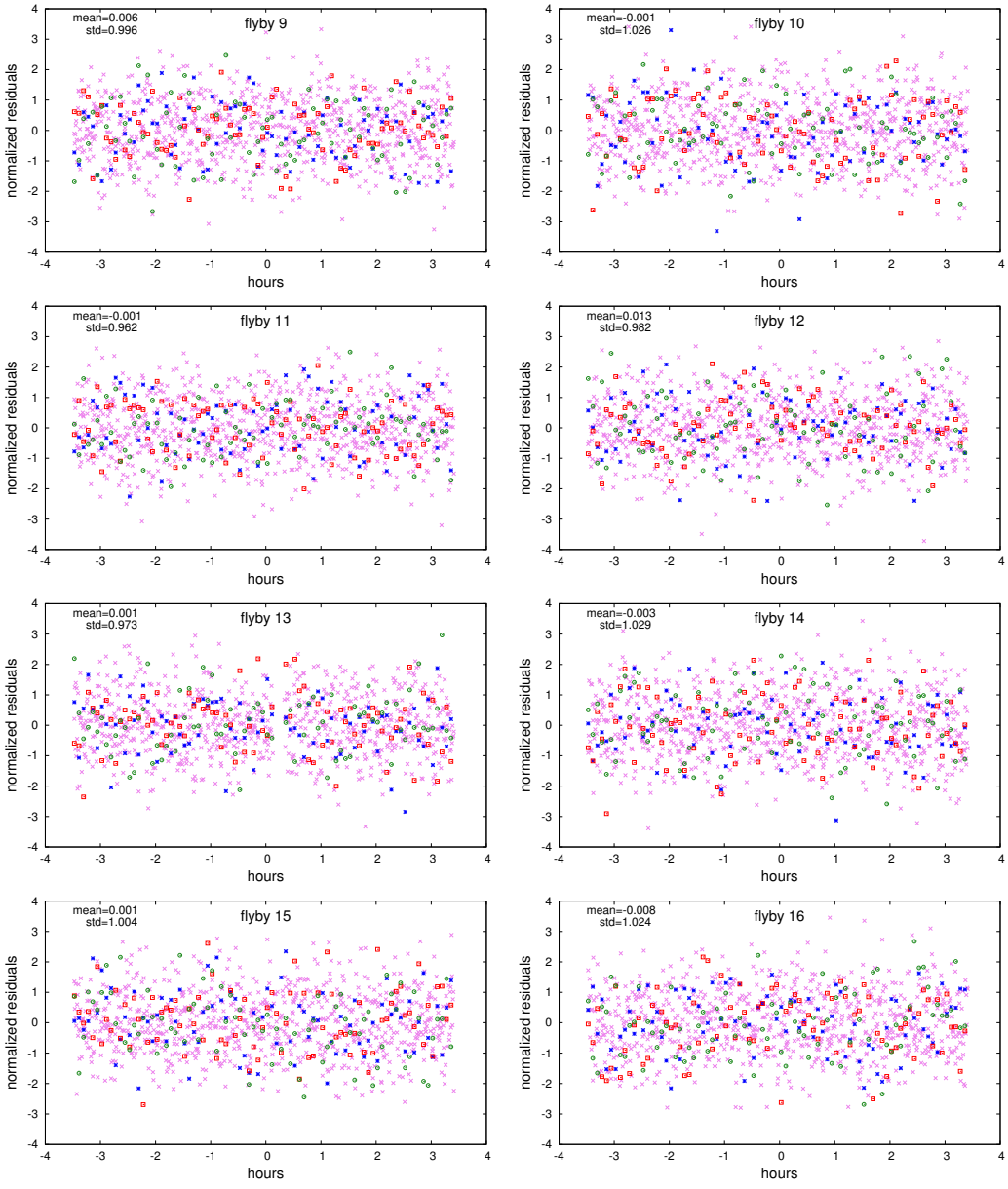

Figure 8.2.: *Normalized residuals of the eight flybys in the middle of the phase. The violet crosses are the residuals of range-rate observations, blue asterisks for range, red squares and green circles for VLBI (right ascension and declination respectively). The residuals are taken at the last iteration of the differential corrections of the experiment E5 reported in the tables.*

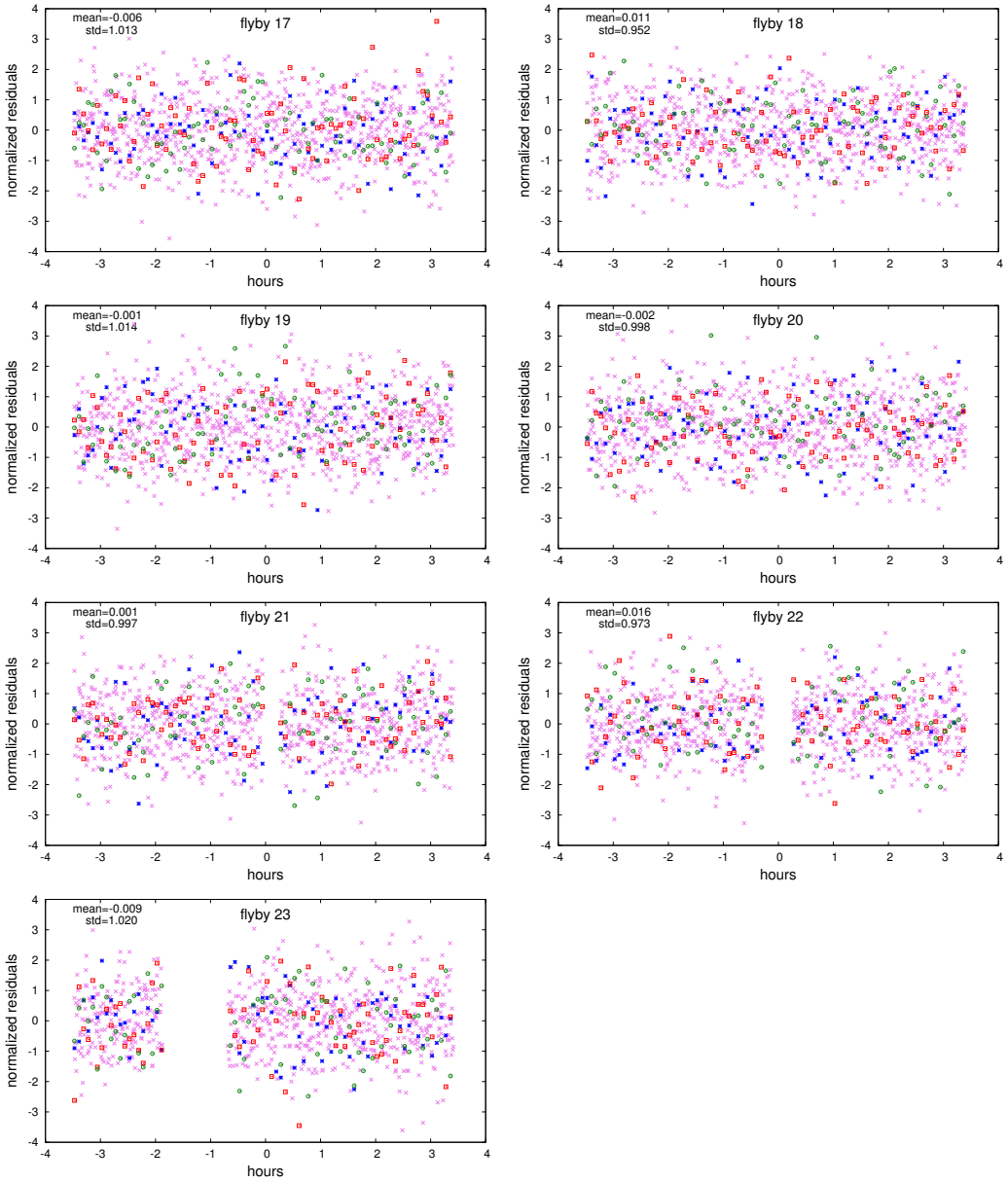

Figure 8.3.: *Normalized residuals of the last seven flybys. The violet crosses are the residuals of range-rate observations, blue asterisks for range, red squares and green circles for VLBI (right ascension and declination respectively). The residuals are taken at the last iteration of the differential corrections of the experiment E5 reported in the tables.*

It.	E1	E2	E3	E4	E5	E6	E7	E8	E9	E10
1	1.4d10	5.2d11	7.1d10	7.2d9	3.3d11	5.7d10	3.2d9	2.2d10	5.5d11	1.6d11
2	1.3d3	6.2d5	1.4d6	2.7d6	9.7d6	1.4d6	9.1d4	1.2d5	2.8d7	1.7d4
3	2.1d3	2.8d5	1.2d7	1.4d7	4.3d7	7.0d6	6.4d5	7.4d5	5.4d7	1.9d3
4	1.0d2	5.0d4	7.3d5	4.6d5	1.1d6	1.7d5	1.4d4	9.9d3	1.4d5	4.9d2
5	1.10	1.2d2	4.8d3	7.9d3	4.4d4	2.2d3	7.7d1	9.5d1	1.9d2	1.77
6	.996	6.53	1.5d2	9.0d1	2.7d2	3.4d1	3.98	2.89	7.16	1.03
7		1.00	1.86	1.85	5.30	1.22	1.01	1.03	.992	.994
8		.995	.999	.994	1.05	1.02	.997	1.00		.992
9			1.00		.997	.990	.994	1.00		
10			1.00		.992			1.00		

It.	E1	E2	E3	E4	E5	E6	E7	E8	E9	E10
1	1.4d6	8.4d6	3.1d6	9.9d5	6.7d6	2.8d6	6.6d5	1.7d6	8.6d6	4.6d6
2	4.2d2	9.1d3	1.4d4	1.9d4	3.6d4	1.4d4	3.5d3	4.0d3	6.1d4	1.5d3
3	5.3d2	6.1d3	4.1d4	4.3d4	7.6d4	3.1d4	9.3d3	1.0d4	8.5d4	5.1d2
4	1.2d2	2.6d3	9.9d3	7.9d3	1.2d4	4.9d3	1.4d3	1.2d3	4.3d3	2.6d2
5	3.80	1.3d2	8.1d2	1.0d3	2.4d3	5.4d2	1.0d2	1.1d2	3.2d3	1.0d1
6	.416	2.7d1	1.4d2	1.1d2	1.9d2	6.7d1	2.0d1	1.6d1	1.6d2	2.17
7		1.21	1.1d1	1.1d1	2.4d1	5.58	1.52	2.27	2.9d1	.663
8		.401	.697	.355	2.80	2.14	.722	.782	.330	.478
9			.845		.927	.372	.433	.938		
10			.952		.319			1.12		

Table 8.2.: On the top, values of the target function Ω for all the iterations of the ten experiments. On the bottom, the norm of the correction $\Delta\mathbf{x}$.

that the fit worked well: the mean of the residuals is close to 0 and the standard deviation is close to 1 for all the arcs. Just few points have absolute value greater than 3 and none of them exceeds 4. It is worth noting that there are not clear differences between the flybys, so that we do not have worse or better results for further or closer arcs.

In the following sections we will give the details about the formal uncertainties σ, obtained from the covariance matrix, and the true errors ϵ, calculated as components of $\mathbf{x} - \mathbf{x}_T$, with $\mathbf{x}$ vector of the fit parameters at convergence. While the formal uncertainties are almost identical for all the experiments, the true errors depend on the first guess of the fit parameters and the Gaussian noise added to the simulated observables. The results we will show are the averages of the ten experiment we performed; in particular, we consider the absolute value of ϵ. Because of the operation of mean, we will find values for ϵ close to σ, and generally smaller.

8.1 GRAVITATIONAL AND TIDAL PARAMETERS

Gravitational anomalies and Love numbers are essential to understand the internal structure and the geological history of the bodies, therefore their knowledge is a point we cannot omit in our investigation. Since we consider a large number of fit parameters, we compress the information of the moons' gravitational fields in a single value per each degree l. In this way, instead of presenting more than 100 values for the coefficients of the Ganymede's gravitational field, we summarize the results in just 10 more significant numbers. Given a degree l, we compute

$$\sigma_l = \frac{\sqrt{\sum_{m=0}^{l}(\sigma_{l,m,0}^2 + \sigma_{l,m,1}^2)}}{2l+1},$$

where $\sigma_{l,m,0}$ is the formal uncertainty of the coefficient S_{lm}, while $\sigma_{l,m,1}$ the one of C_{lm}. We use an analogous formula for the true error ϵ_l. Since for Europa we estimate just two parameters, we have 2 at the denominator instead of $2l+1$.

As shown in Figure 8.4, the true errors are not distant from the formal uncertainty, meaning that the differential corrections converged to acceptable values. Moreover, apart from the number of degrees determined for Ganymede, the differences in the estimation between the three moons are clear from the height of the points plotted in the figure. The lower harmonics of Ganymede are determined with an uncertainty one order of magnitude better than the ones of Callisto and two orders than the ones of Europa. This is evident also from Table 8.3, where we reported the main coefficients of the gravitational fields: ΔC_{00}, C_{20} and C_{22}. For all the moons we find an important improvement with respect to the estimation of the Galileo mission (see Table 7.5); moreover, the number of estimated harmonic coefficients is far greater and the true errors should be smaller.

In Table 8.3 we present also the results on the gravitational parameters of Jupiter and the moons' Love numbers. The nominal values we used in simulation can be found in Table 6.1 and Table 6.2.

The formal uncertainty of the higher harmonics of Jupiter is completely determined by the apriori constraints we added, since the orbits we consider are higher than the pericenters of the Juno mission and then JUICE data do not contribute to the parameters' estimation. However, for J_2 and J_3 we find a slight improvement, due to the wide time span we are considering. With the acquisition of new data, the level of knowledge that the Juno mission will reach for these harmonics will allow to omit them in our estimation. Surprisingly, we obtain an extraordinary result on the mass of Jupiter, improving its uncertainty of more than two orders of magnitude; this is probably due to the length of the mission and the fact we can check its effect not just on the spacecraft's orbit but also on the orbits of the moons.

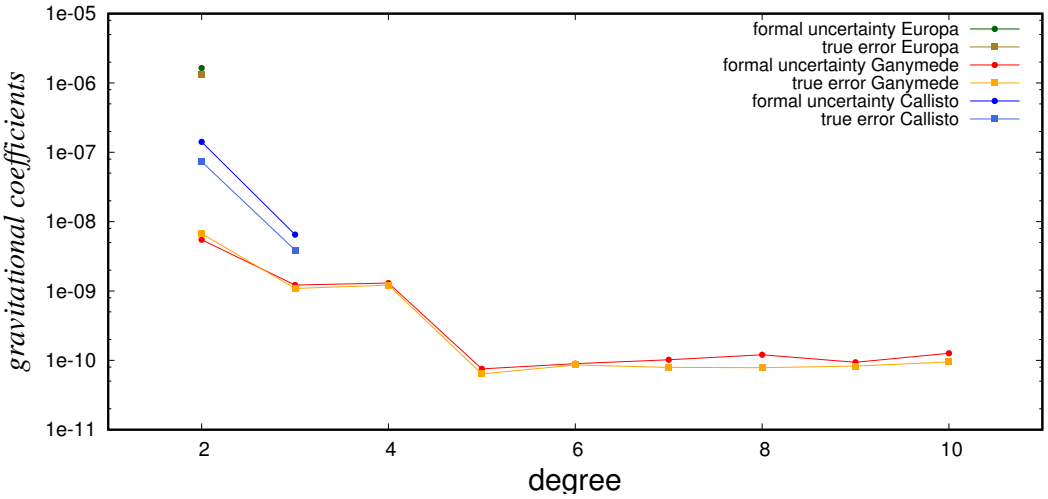

Figure 8.4.: *Formal uncertainties σ_l and true errors ϵ_l of the gravitational field's coefficients of Europa, Ganymede and Callisto.*

Finally, with the JUICE mission data we manage to determine with a good accuracy the k_2 parameters of all the moons and we obtain a discrete estimation of k_3 of Ganymede. Instead, the uncertainty of k_4 is well over its true value, meaning that we are not able to constrain it with the data considered in the orbit determination.

8.2 EPHEMERIDES AND DISSIPATIVE PARAMETERS

As we mentioned in Chapter 7, one of the objective of the JUICE mission is to improve the planetary and Galilean satellites' ephemerides. In our experiments we take into account these requirements estimating their initial conditions, expressed in an Ecliptic coordinate system.

The BJS initial conditions intervene mainly as kinematical parameter in the prediction functions of the observables. Since it is present in almost all the observations, it is very important to add it in the fit parameters in order to include its contribution in the formal uncertainties of the other parameters. From Table 8.4 we can appreciate how the level of the estimation is extremely good, reaching the order of few centimeters in position (x and y coordinates) and 10^{-7} cm/s in velocity ($\dot{x}$ and $\dot{y}$). The reason why the x and y coordinates are determined better than z is due to the fact the radioscience experiments capture better these components, while VLBI experiment is more sensitive to the last one. In fact the orbital motion of the BJS and the Galilean satellites takes place mainly on the plane xy, being in an Ecliptic system. The result on the BJS will allow to improve the ephemerides of all the planets, since a better knowledge on the position of the Jovian System will

	Eu			Ga			Ca		
	ΔC_{00}	C_{20}	C_{22}	ΔC_{00}	C_{20}	C_{22}	ΔC_{00}	C_{20}	C_{22}
σ	1.3d-8	2.1d-6	1.0d-6	4.5d-9	1.1d-8	5.5d-9	5.9d-9	2.8d-7	1.4d-7
$\lvert\epsilon\rvert$	7.1d-9	1.7d-6	8.6d-7	3.1d-9	1.3d-8	6.7d-9	5.3d-9	1.5d-7	7.2d-8

	Eu		Ga		Ca
	k_2	k_2	k_3	k_4	k_2
σ	8.4d-3	1.2d-4	2.7d-2	8.9	1.5d-2
$\lvert\epsilon\rvert$	7.1d-3	1.4d-4	2.4d-2	8.4	8.1d-3

	Jup					
	ΔC_{00}	J_2	J_3	J_4	J_5	J_6
σ	3.3d-11	4.9d-9	9.0d-9	4.0d-9	8.0d-9	9.0d-9
$\lvert\epsilon\rvert$	2.1d-11	3.2d-9	3.1d-9	1.0d-11	7.6d-11	7.6d-13

Table 8.3.: Formal uncertainties and true errors of the dynamical parameters. In the top table we reported the results for the main coefficients of the moons' gravitational fields; in the middle table the results for the tidal coefficients; in the bottom table the results for the spherical harmonics of Jupiter.

imply a better determination of the other bodies' states. In this context, it would be interesting to try to obtain direct estimation of the other planets' orbits and parameters using JUICE data; obviously, to do this, it will be necessary to consider past observations of these bodies. This is a point we will take up for the Galilean satellites.

The accuracy of the moons' ephemerides is of the order of tens of kilometers in positions. The results we obtain on the initial conditions of the Galilean satellites is several orders of magnitude smaller, as shown in Table 8.4. In particular for Io we obtain a total formal uncertainty of tens of meters, for Europa some meters, for Ganymede few tens of centimeters and for Callisto few meters. This is due to the extremely accurate data we are considering and the intensive plan of observations scheduled for JUICE. It is worth noting that, in case of real data, the order of the true error is probably too optimistic, especially for Ganymede, whose formal uncertainty in the x and y components is just few centimeters. However, despite of the systematic errors on the first guess, in our experiments we find that all the true errors are inside the 3-σ interval.

The formal uncertainties we reported in the Table 8.4 are not a global estimation of the moons' orbits accuracy, but the formal uncertainties we obtained on the initial conditions chosen for the JUICE mission. An objective for the future will be to include JUICE data to a wider set of observations, in order to quantify their

	BJS					
	x	y	z	$\dot{x}$	$\dot{y}$	$\dot{z}$
σ	1.4d1	5.8d0	1.8d2	1.6d-7	2.7d-7	3.7d-6
$\lvert\epsilon\rvert$	9.8d0	4.3d0	1.6d2	1.0d-7	2.2d-7	3.5d-6

	Io			Eu		
	x	y	z	x	y	z
σ	2.5d2	1.9d3	8.8d3	3.4d2	1.3d3	7.5d2
$\lvert\epsilon\rvert$	1.6d2	8.7d2	6.0d3	1.9d2	7.1d2	6.0d2
	$\dot{x}$	$\dot{y}$	$\dot{z}$	$\dot{x}$	$\dot{y}$	$\dot{z}$
σ	7.8d-2	1.8d-2	4.9d-1	2.7d-2	6.7d-3	8.0d-3
$\lvert\epsilon\rvert$	3.2d-2	1.0d-2	2.8d-1	1.4d-2	3.5d-3	4.3d-3

	Ga			Ca		
	x	y	z	x	y	z
σ	5.2d0	1.1d1	9.9d1	9.8d1	1.4d1	3.6d2
$\lvert\epsilon\rvert$	3.5d0	5.9d0	7.2d1	9.8d1	1.1d1	2.0d2
	$\dot{x}$	$\dot{y}$	$\dot{z}$	$\dot{x}$	$\dot{y}$	$\dot{z}$
σ	1.1d-4	4.9d-5	8.8d-4	1.5d-4	2.6d-4	1.4d-3
$\lvert\epsilon\rvert$	8.5d-5	2.7d-5	6.2d-4	1.4d-4	2.6d-4	9.2d-4

Table 8.4.: Formal uncertainties and true errors of the initial conditions parameters (units of measure cm for the position and cm/s for the velocity). On the top we reported the results relative to the BJS state, while on the bottom the values relative to the moons' initial positions and velocities.

real contribution on the determination of the moon's orbits, with the generation of more accurate ephemerides.

Finally, in Table 8.5, we reported the formal uncertainties of the dissipative parameters, compared with the values published in [24]. They are the most important results of the estimation and the main objective of this part of the thesis: for k_2/Q of Io we obtain $\sigma = 4.7 \times 10^{-4}$, while for k_2/Q of Jupiter 2.1×10^{-6}. The correlation between the two parameters is 0.9549, due to the similar (and opposite) effect they have on the orbit of Io. For the dissipative parameters we obtain true errors inside the 1-σ value for every experiment and a mean value for $|\epsilon|$ three times smaller than σ, which shows that the estimation works very well for these parameters.

The result we achieved is significant, since the formal uncertainty for k_2/Q of Io is almost one order of magnitude better than the one published in [24] and k_2/Q of Jupiter is determined at the same level of the paper. This shows that the total inversion we performed, using the constrained multi-arc strategy in the

	Io	Jup
	k_2/Q	k_2/Q
σ [24]	3.0d-3	2.0d-6
σ	4.7d-4	2.1d-6
$\lvert\epsilon\rvert$	1.6d-4	7.5d-7

Table 8.5.: Formal uncertainties and true errors of the dissipative parameters. In the first row we reported the formal uncertainties obtained in [24], in order to make a comparison.

flybys phase, allows to obtain results better than the ones already presented in [8] for JUICE. Therefore, we found that the potential total information of the JUICE mission data is equivalent or greater than the one contained in more than 100 years of astrometric observations. It means that JUICE could provide an independent estimation of the same level of [24] and that we could compare the results obtained with the two different data sets. Moreover, as mentioned for the ephemerides, it will be important to combine all the available observations of the Galilean satellites, in order to obtain a new and more precise estimation.

8.3 CONTRIBUTION OF THE CONSTRAINED MULTI-ARC METHOD

In order to assess the actual advantage due to the inclusion of the jumps in the target function, we performed a covariance analysis, adding constraints one by one and looking at the improvement of the formal uncertainty of the dissipative parameters. We do not perform complete orbit determination experiments, but we stop the simulations once we invert the normal matrix.

Since we consider constraints only between some flybys and not all of them, it is worth noting that we cannot solve for all the manoeuvres. For example, if we constrain just the last two fybys, we must solve for the manoeuvre between them, while the others are invisible to our simulation.

We start to consider jumps from the last flybys, until to reach the first one. In Figure 8.5 we show the formal uncertainty of Io's k_2/Q (the behaviour of the Jupiter's dissipative parameter is identical) as we add constraints between the flybys: on the left we reported the result in case we use the constraints' values adopted in the thesis, while on the right the case of ideal stricter constraints, set to 1 cm in position and 10^{-4} cm/s in velocity for all the flybys.

As represented in the figure, the uncertainty decreases in a significant way, until to reach half its initial value in the more convenient set up (ideal constraints and no estimation of the manoeuvres). Unfortunately, in a realistic estimation we cannot avoid to consider the manoeuvres as fit parameters and we must take into

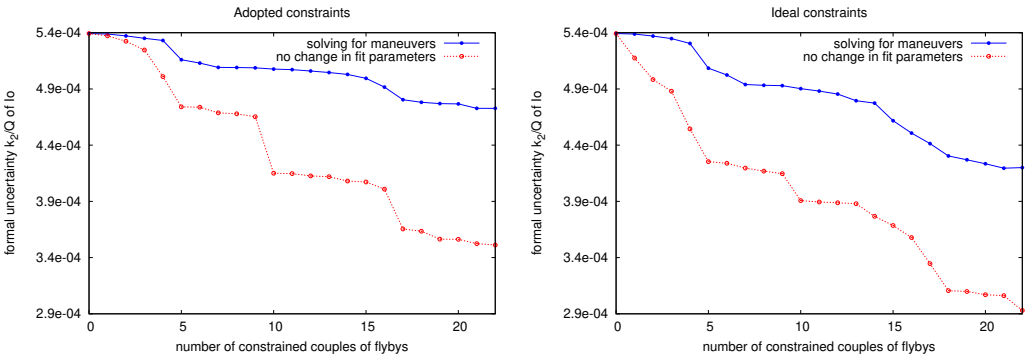

Figure 8.5.: *Formal uncertainty of the dissipative parameter* (k_2/Q) *of Io as function of the number of constrained couples of flybys. In* 0 *we put the value in the non-constrained case, while from* 1 *to* 22 *the values obtained constraining from arcs* $23° - 22°$ *to* $23° - 1°$*. In the figure on the left we showed the result with the constraints we adopted in the thesis, while on the right we used ideal values. In each figure we reported the case we solve for manoeuvres between constrained flybys (blue line) and the case we do not solve for them (red line), in order to better understand the contribution of the constrained multi-arc strategy.*

a account the critical issues arising from using too strict constraints for the jumps. In the set up chosen for the experiments of the thesis we pass from 5.4×10^{-4} to 4.7×10^{-4}, which is the final value we reported in the results. Although in this case the gain can seem quite limited, looking at the other simulations there is room for increasing it.

It is interesting to see for which flybys we obtain larger decreases of the formal uncertainty of the dissipative parameters. In the case we solve for manoeuvres, we find that the estimation improves more when flybys of Ganymede and Europa are involved, while during the long series of flybys of Callisto it reduces its descent. This is due to the fact that the energy dissipation of Io affects mostly the other two moons in resonance. However, in the case we do not consider manoeuvres in the fit parameters, we obtain an important improvement also constraining one of the jumps located between the close encounters of Callisto. This conjunction is different from the others of the same phase, since it is in the middle of two very distant flybys (almost 100 days). In this case the information contained in the jump manages to give a greater contribution to the determination of k_2/Q.

It is also possible that the scheduled times of the manoeuvres can affect the contribution of the constrained multi-arc to the orbit determination and that other configurations can provide better estimation of the parameters. A more suitable disposition of the manoeuvres, or the elimination of them during some flybys, is worth being investigated in the future.

8.4 CONCLUSION

In this thesis we presented a preliminary study of orbit determination experiments with JUICE mission data. Although the project is at its initial stage, for the first time it has been performed a global inversion of the data, estimating both dynamical parameters, recovered from the spacecraft's motion, and the satellites' orbits. We investigated the contribution of the JUICE mission data to the improvement of the knowledge of the Galilean satellites' structure and dynamics, using all the different data provided by the mission and fitting a large number of parameters. Since one of the main objective of JUICE is to reconstruct a gravitational model of the moons, especially for Ganymede, we included the coefficients C_{lm} and S_{lm} of the satellites in the fit parameters, considering also high degrees parameters for fulfilling the requirements of the mission. We estimated the Ganymede's field up to degree ten, but it is easy to prove that better resolutions can be achieved, especially if an extension of the mission at lower altitudes will be approved. Moreover, we showed that, thanks to the flybys, JUICE can improve the knowledge of the low harmonics of Europa and Callisto.

However, considering also the first part of the thesis, we focused our study on the dissipative parameters and the moons' orbits. From the values presented in the previous section, we found that thanks to JUICE we could reach an independent estimation of the dissipative parameters, which could be used for a validation of the past theories (see Table in the Introduction). In particular, the JUICE observations alone can provide an independent result that can be compared with the ones presented in [16] and [24], solving the riddle about the amount of dissipation in the system.

Although this is a very promising result, in the future we cannot limit the estimation of the dissipative effects considering just the JUICE data, but we have to include all the past observations of the Galilean satellites. In fact, we must aim to a solution of the motion that fits also the past astrometric data. In this way, we can relate this work to the ones we cited, as [24], and we can verify the result with a larger time span, and not limited to a small portion of time. Therefore, one of the objectives for the next future will be to perform new simulations not limited just to the JUICE observations, but adding other data sets. Moreover, also the planets could be involved in this general improvement of the ephemerides.

Since the astrometric data accuracy is some orders of magnitude larger than the one of radioscience experiments (almost some tens of kilometers), the linear divergence of the Galilean satellites' transition matrix, shown in Figure 7.1, should not cause problems in the combined estimation. In fact, small changes in the moons' initial conditions of the order of the machine error will be propagated to few meters maximum, a variation almost negligible for astrometric data. Instead, considering also Galileo mission data could be more challenging, being the time

between the two missions greater than 40 years; in this case the control on the residuals of the two data sets is more problematic. The same issue arises for Europa Clipper data, the future NASA mission to Europa. Moreover, since the number of the scheduled flybys of Europa is 45, the numerical instability arising from the chaos in the spacecraft's orbit, well represented in Figure 7.3, will be even more amplified with respect to JUICE.

Finally, a lot of work still misses for improving our simulations and for processing the future real data of JUICE; amongst them we cite:

- improvement of the dynamical models. Regarding the dissipation, it will be important to add the dissipative effects of the other moons, taking into account the different values of k_2/Q of Jupiter at the satellites' orbital frequencies. For the spacecraft, we will need more sophisticated non-gravitational models, which take into account the actual shape of the probe. Since we propagate the spacecraft for tens of days outside the tracking sessions, these forces are not negligible. Moreover, we must implement a model for the atmospheric drag during the low altitude phase around Ganymede.

- Addition of aberration effects on the prediction functions. In the range and range-rate functions we added the Shapiro time delay of the radio signal, due to the deformation of the space near Jupiter and the Sun. However, we did not studied aberration effects on VLBI and astrometric data, whose contribution on the observables must be taken into account.

- Verification of the setting we used for the experiments. Although it is very improbable that the tour of the mission will change at this stage of the plan, it is possible that the scheduling of the observations can suffer some modifications. For example, as VLBI observations are more expensive than radioscience experiments because they must involve a network of ground-based stations, their sessions could be reduced in number. Moreover, the availability of astrometric observations of the JANUS camera must be confirmed officially yet.

Despite of some critical issues we had to deal with, we managed to carry out a first study of the complete performances of the radioscience experiment for the JUICE mission. It is important to quantify which is the reliability of the formal uncertainties we obtained, especially for the determination of the moons' initial conditions. However, the preliminary results are more than satisfying. Since the results depend strongly on the scheduling of the observations, as witnessed by the necessity of camera's observations of Io, it is very important to encourage a synergy between the various experiments of the mission. In fact, the results we showed are a combination of efforts between different experiments and instruments, all of them essential to reach the positive parameters estimation we obtained in the numerical simulations.

A COMPLETE SEMI-ANALYTICAL MODEL

In the first part of the thesis we presented a semi-analytical model of the Galilean satellites' dynamics. Because of the length of the Hamiltonian, we avoided reporting its whole expression in Chapter 3, but we chose to give the details in this appendix. In particular, in the next sections we present all the coefficients and all the terms we added to the model.

A.1 LAPLACE COEFFICIENTS

In Chapter 2 we showed the expansion of the third-body perturbation (2.11) and we indicated with c_j the coefficients of the terms. Each term is a combination of other objects, called Laplace coefficients. Their general expression is

$$b_s^j(\alpha) = \frac{1}{\pi}\int_0^{2\pi} [1 - 2\alpha\cos\psi + \alpha^2]^{-s}\cos(j\psi)\,d\psi,$$

where j is an integer, s a real number and α is the ratio of the semi-major axes of the two satellites and it is a number between 0 and 1 (in the case of a $2:1$ resonance, α is near 0.63).

We can get a new formula using a Taylor expansion in α

$$\begin{aligned}\frac{1}{2}b_s^j(\alpha) =& \frac{s(s+1)\dots(s+j-1)}{1\cdot 2\cdot 3\dots j}\alpha^j \\ &\times\left[1 + \frac{s(s+j)}{1(j+1)}\alpha^2 + \frac{s(s+1)(s+j)(s+j+1)}{1\cdot 2(j+1)(j+2)}\alpha^4 + \dots\right].\end{aligned}$$

The coefficients c_j contain also the derivatives of the Laplace coefficients; because of the simple structure of the Taylor expansion, we can use a recursive formula

$$D^n b_s^j = s\left(D^{n-1}b_{s+1}^{j-1} - 2\alpha D^{n-1}b_{s+1}^j + D^{n-1}b_{s+1}^{j+1} - 2(n-1)D^{n-2}b_{s+1}^j\right)$$

where D is the derivative with respect to α and n is the order of the derivation.

From [34], Appendix B, we have the formulas for all the coefficients we need in the model. Following the cited book, we use the notation $A_j = b_{1/2}^{(j)}$ and $B_j = b_{3/2}^{(j)}$.

- For the mutual perturbation between satellites (up to the second order)

$$
\begin{aligned}
c_{(0,0,0,0,0,0)} &= (1/2)A_0 \\
c^1_{(0,0,0,0,0,0)} &= (1/8)(2\alpha D + \alpha^2 D^2)A_0 \\
c^2_{(0,0,0,0,0,0)} &= -(1/2)\alpha B_1 \\
c_{(0,0,-1,1,0,0)} &= (1/4)(2 - 2\alpha D - \alpha^2 D^2)A_1 \\
c_{(0,0,0,0,-1,1)} &= \alpha B_1 \\
c_{(-1,2,-1,0,0,0)} &= (1/2)(-4 - \alpha D)A_2 \\
c_{(-1,2,0,-1,0,0)} &= (1/2)(3 + \alpha D)A_1 - (1/2)(1/\alpha^2) \\
c_{(-2,4,-2,0,0,0)} &= (1/8)(44 + 14\alpha D + \alpha^2 D^2)A_4 \\
c_{(-2,4,0,-2,0,0)} &= (1/8)(38 + 14\alpha D + \alpha^2 D^2)A_2 \\
c_{(-2,4,-1,-1,0,0)} &= (1/4)(-42 - 14\alpha D - \alpha^2 D^2)A_3 \\
c_{(-2,4,0,0,-2,0)} &= (1/2)\alpha B_3 \\
c_{(-2,4,0,0,0,-2)} &= (1/2)\alpha B_3 \\
c_{(-2,4,0,0,-1,-1)} &= -\alpha B_3
\end{aligned}
$$

- For the mutual perturbation between satellites (third order)

$$
\begin{aligned}
c^1_{(-1,2,-1,0,0,0)} &= (1/16)(28 + 5\alpha D - 6\alpha^2 D^2 - \alpha^3 D^3)A_2 \\
c^2_{(-1,2,-1,0,0,0)} &= (1/8)(64 + 6\alpha D - 8\alpha^2 D^2 - \alpha^3 D^3)A_2 \\
c^3_{(-1,2,-1,0,0,0)} &= (1/4)(5\alpha + \alpha^2 D)(B_1 + B_3) \\
c^1_{(-1,2,0,-1,0,0)} &= (1/8)(-12 + 4\alpha D + 7\alpha^2 D^2 + \alpha^3 D^3)A_1 + \alpha \\
c^2_{(-1,2,0,-1,0,0)} &= (1/16)(-28 + 4\alpha D + 9\alpha^2 D^2 + \alpha^3 D^3)A_1 + (3/2)\alpha \\
c^3_{(-1,2,0,-1,0,0)} &= (1/4)(-4\alpha - \alpha^2 D)(B_0 + B_2) + 2\alpha \\
c_{(-3,6,-3,0,0,0)} &= (1/48)(-804 - 279\alpha D - 30\alpha^2 D^2 - \alpha^3 D^3)A_6 \\
c_{(-3,6,-2,-1,0,0)} &= (1/16)(825 + 291\alpha D + 31\alpha^2 D^2 + \alpha^3 D^3)A_5 \\
c_{(-3,6,-1,-2,0,0)} &= (1/16)(-832 - 302\alpha D - 32\alpha^2 D^2 - \alpha^3 D^3)A_4 \\
c_{(-3,6,0,-3,0,0)} &= (1/48)(816 + 312\alpha D + 33\alpha^2 D^2 + \alpha^3 D^3)A_3 \\
c_{(-3,6,-1,0,-2,0)} &= (1/4)(-9\alpha - \alpha^2 D)B_5 \\
c_{(-3,6,-1,0,0,-2)} &= (1/4)(-9\alpha - \alpha^2 D)B_5 \\
c_{(-3,6,0,-1,-2,0)} &= (1/4)(12\alpha + \alpha^2 D)B_4 \\
c_{(-3,6,0,-1,0,-2)} &= (1/4)(12\alpha + \alpha^2 D)B_4 \\
c_{(-3,6,-1,0,-1,-1)} &= (1/2)(9\alpha + \alpha^2 D)B_5 \\
c_{(-3,6,0,-1,-1,-1)} &= (1/2)(-12\alpha - \alpha^2 D)B_4 \\
c_{(-1,4,-3,0,0,0)} &= (1/48)(-136 - 93\alpha D - 18\alpha^2 D^2 - \alpha^3 D^3)A_4 \\
c_{(-1,4,-2,-1,0,0)} &= (1/16)(147 + 101\alpha D + 19\alpha^2 D^2 + \alpha^3 D^3)A_3 \\
c_{(-1,4,-1,-2,0,0)} &= (1/16)(-152 - 108\alpha D - 20\alpha^2 D^2 - \alpha^3 D^3)A_2 \\
c_{(-1,4,0,-3,0,0)} &= (1/48)(142 + 114\alpha D + 21\alpha^2 D^2 + \alpha^3 D^3)A_1 - (16/3)\alpha
\end{aligned}
$$

$$
\begin{aligned}
c_{(-1,4,-1,0,-2,0)} &= (1/4)(-5\alpha - \alpha^2 D)B_3 \\
c_{(-1,4,-1,0,0,-2)} &= (1/4)(-5\alpha - \alpha^2 D)B_3 \\
c_{(-1,4,0,-1,-2,0)} &= (1/4)(8\alpha + \alpha^2 D)B_2 \\
c_{(-1,4,0,-1,0,-2)} &= (1/4)(8\alpha + \alpha^2 D)B_2 \\
c_{(-1,4,-1,0,-1,-1)} &= (1/2)(5\alpha + \alpha^2 D)B_3 \\
c_{(-1,4,0,-1,-1,-1)} &= (1/2)(-8\alpha - \alpha^2 D)B_2 \\
c_{(-1,2,-2,1,0,0)} &= (1/16)(-105 - 19\alpha D + 7\alpha^2 D^2 + \alpha^3 D^3)A_3 \\
c_{(-1,2,1,-2,0,0)} &= (1/16)(-10\alpha D - 8\alpha^2 D^2 - \alpha^3 D^3)A_0 \\
c_{(-1,2,1,0,-2,0)} &= (1/4)(-\alpha - \alpha^2 D)B_1 \\
c_{(-1,2,1,0,0,-2)} &= (1/4)(-\alpha - \alpha^2 D)B_1 \\
c_{(-1,2,0,1,-2,0)} &= (1/4)(-4\alpha + \alpha^2 D)B_2 \\
c_{(-1,2,0,1,0,-2)} &= (1/4)(-4\alpha + \alpha^2 D)B_2 \\
c_{(-1,2,-1,0,1,-1)} &= (1/2)(-5\alpha - \alpha^2 D)B_1 \\
c_{(-1,2,-1,0,-1,1)} &= (1/2)(-5\alpha - \alpha^2 D)B_3 \\
c_{(-1,2,1,0,-1,-1)} &= (1/2)(\alpha + \alpha^2 D)B_1 \\
c_{(-1,2,0,-1,1,-1)} &= (1/2)(4\alpha + \alpha^2 D)B_0 - 4\alpha \\
c_{(-1,2,0,-1,-1,1)} &= (1/2)(4\alpha + \alpha^2 D)B_2 \\
c_{(-1,2,0,1,-1,-1)} &= (1/2)(4\alpha - \alpha^2 D)B_2
\end{aligned}
$$

- For the perturbation of the Sun (additional terms)

$$
\begin{aligned}
c_{(0,1,-1,0,0,0))} &= (1/2)(-2 - \alpha D)A_1 + (3/2)\alpha \\
c_{(0,2,-2,0,0,0))} &= (1/8)(6 + 6\alpha D + \alpha^2 D^2)A_2 \\
c_{(0,2,-1,-1,0,0))} &= (1/4)(-6 - 6\alpha D - \alpha^2 D^2)A_1 + 3\alpha \\
c_{(0,2,0,0,-2,0))} &= (1/2)\alpha B_1 \\
c_{(0,2,0,0,0,-2))} &= (1/2)\alpha B_1 \\
c_{(0,2,0,0,-1,-1))} &= -\alpha B_1
\end{aligned}
$$

It is worth noting that, generally, these coefficients are calculated at the beginning of the propagation and they are left constant, since their variation does not change in a significant way the dynamics. In the case of the Galilean satellites, in order to obtain a very good approximation of the resonant motion, we consider the dependence of $c_{(0,0,0,0,0,0)}$, $c_{(-1,2,-1,0,0,0)}$ and $c_{(-1,2,0,-1,0,0)}$ on the semi-major axes and we compute their contribution into the Hamilton's equations. Another important point to be clarified is the indirect term that we find in some c_j: it is the part which does not involve the Laplace coefficients. Generally its expression depends on whether we are considering a perturbation due to an outer or inner body. For example, for $c_{(-1,2,0,-1,0,0)}$ the first version is -2α, while the second

is $-1/(2\alpha^2)$. Fortunately, for a $2:1$ resonance, all the indirect terms we consider have almost the same value, because of the particular α of the resonance. However, since for $c_{(-1,2,0,-1,0,0)}$ we must compute the derivative with respect to the semi-major axes, the two choices are not equivalent. In the model, we considered the expression given considering an inner perturber, since the corresponding term of the Hamiltonian is more related to the evolution of the outer body, containing ϖ_2 in the argument of the cosine.

A.2 HAMILTONIAN

In Chapter 3 we presented the various elements of the Hamiltonian that defines the semi-analytical model of the Galilean satellites' dynamics. In this section we collect all the terms in five main parts.

(1) Keplerian term

$$\mathcal{H}_0 = -\mu_1^2\beta_1^3/(2L_1^2) - \mu_2^2\beta_2^3/(2L_2^2) - \mu_3^2\beta_3^3/(2L_3^2) + n_s L_s$$

For the sake of simplicity we use L_i instead of their expressions in terms of the new variables. The last addendum describes the dynamics of the Sun: n_s is its mean motion, which is constant, and L_s is the momentum relative to its longitude.

(2) Jupiter's gravitational field

$$\begin{aligned}
\mathcal{H}_{obl} &= j_{1;1}/L_1^6 + j_{2;1}/L_2^6 + j_{3;1}/L_3^6 \\
&+ j_{1;2}(x_1^2 + y_1^2 - u_1^2 - v_1^2) + j_{2;2}(x_2^2 + y_2^2 - u_2^2 - v_2^2) \\
&+ j_{3;2}(x_3^2 + y_3^2 - u_3^2 - v_3^2) + j_{4;2}(x_4^2 + y_4^2 - u_4^2 - v_4^2) \\
&+ j_{1;3}/L_1^{10} + j_{2;3}/L_2^{10} + j_{3;3}/L_3^{10} \\
&+ j_{1;4}(x_1^2 + y_1^2 - u_1^2 - v_1^2) + j_{2;4}(x_2^2 + y_2^2 - u_2^2 - v_2^2) \\
&+ j_{3;4}(x_3^2 + y_3^2 - u_3^2 - v_3^2) + j_{4;4}(x_4^2 + y_4^2 - u_4^2 - v_4^2)
\end{aligned}$$

In the coefficients $j_{i;l}$, i indicates the involved Galilean satellite and l is the number of the coefficient.

(3) Mutual perturbation satellites (up to the second order)

$$\begin{aligned}
\mathcal{H}_{mut} &= a_{1,2;1} \\
&+ a_{1,2;2}(x_1^2 + y_1^2) + a_{1,2;3}(x_2^2 + y_2^2) + a_{1,2;4}(x_1x_2 + y_1y_2) \\
&+ a_{1,2;5}(u_1^2 + v_1^2) + a_{1,2;6}(u_2^2 + v_2^2) + a_{1,2;7}(u_1u_2 + v_1v_2) \\
&+ a_{1,2;8}x_1/\sqrt{L_1} + a_{1,2;9}x_2/\sqrt{L_2} \\
&+ a_{1,2;10}(x_1^2 - y_1^2) + a_{1,2;11}(x_2^2 - y_2^2) + a_{1,2;12}(x_1x_2 - y_1y_2) \\
&+ a_{1,2;13}(u_1^2 - v_1^2) + a_{1,2;14}(u_2^2 - v_2^2) + a_{1,2;15}(u_1u_2 - v_1v_2) \\
&+ a_{2,3;1}(L_2/L_3) \\
&+ a_{2,3;2}(x_2^2 + y_2^2) + a_{2,3;3}(x_3^2 + y_3^2) + a_{2,3;4}[(x_2x_3 + y_2y_3)\cos(\gamma_1) - (x_3y_2 - x_2y_3)\sin(\gamma_1)] \\
&+ a_{2,3;5}(u_3^2 + v_3^2) + a_{2,3;6}(u_2^2 + v_2^2) + a_{2,3;7}[(u_2u_3 + v_2v_3)\cos(\gamma_1) - (u_3v_2 - u_2v_3)\sin(\gamma_1)] \\
&+ a_{2,3;8}[x_2\cos(\gamma_1) - y_2\sin(\gamma_1)]/\sqrt{L_2} + a_{2,3;9}x_3/\sqrt{L_3}
\end{aligned}$$

$$
\begin{aligned}
&+ a_{2,3;10}[(x_2^2-y_2^2)\cos(2\gamma_1)-2x_2y_2\sin(2\gamma_1)]+a_{2,3;11}(x_3^2-y_3^2)\\
&+ a_{2,3;12}[(x_2x_3-y_2y_3)\cos(\gamma_1)-(x_3y_2+x_2y_3)\sin(\gamma_1)]\\
&+ a_{2,3;13}[(u_2^2-v_2^2)\cos(2\gamma_1)-2u_2v_2\sin(2\gamma_1)]+a_{2,3;14}(u_3^2-v_3^2)\\
&+ a_{2,3;15}[(u_2u_3-v_2v_3)\cos(\gamma_1)-(u_3v_2+u_2v_3)\sin(\gamma_1)]\\
&+ a_{1,3;1}(L_1/L_3)\\
&+ a_{1,3;2}(x_1^2+y_1^2)+a_{1,3;3}(x_3^2+y_3^2)+a_{1,3;4}[(x_1x_3+y_1y_3)\cos(\gamma_1)-(x_3y_1-x_1y_3)\sin(\gamma_1)]\\
&+ a_{1,3;5}(u_1^2+v_1^2)+a_{1,3;6}(u_3^2+v_3^2)+a_{1,3;7}[(u_1u_3+v_1v_3)\cos(\gamma_1)-(u_3v_1-u_1v_3)\sin(\gamma_1)]\\
&+ a_{1,4;1}(L_1/L_4)\\
&+ a_{1,4;2}(x_1^2+y_1^2)+a_{1,4;3}(x_4^2+y_4^2)+a_{1,4;4}[(x_1x_4+y_1y_4)\cos(\gamma_1+\gamma_2)-(x_4y_1-x_1y_4)\sin(\gamma_1+\gamma_2)]\\
&+ a_{1,4;5}(u_1^2+v_1^2)+a_{1,4;6}(u_4^2+v_4^2)+a_{1,4;7}[(u_1u_4+v_1v_4)\cos(\gamma_1+\gamma_2)-(u_4v_1-u_1v_4)\sin(\gamma_1+\gamma_2)]\\
&+ a_{2,4;1}(L_2/L_4)\\
&+ a_{2,4;2}(x_2^2+y_2^2)+a_{2,4;3}(x_4^2+y_4^2)+a_{2,4;4}[(x_2x_4+y_2y_4)\cos(\gamma_1+\gamma_2)-(x_4y_2-x_2y_4)\sin(\gamma_1+\gamma_2)]\\
&+ a_{2,4;5}(u_2^2+v_2^2)+a_{2,4;6}(u_4^2+v_4^2)+a_{2,4;7}[(u_2u_4+v_2v_4)\cos(\gamma_1+\gamma_2)-(u_4v_2-u_2v_4)\sin(\gamma_1+\gamma_2)]\\
&+ a_{3,4;1}(L_3/L_4)\\
&+ a_{3,4;2}(x_3^2+y_3^2)+a_{3,4;3}(x_4^2+y_4^2)+a_{3,4;4}[(x_3x_4+y_3y_4)\cos(\gamma_2)-(x_4y_3-x_3y_4)\sin(\gamma_2)]\\
&+ a_{3,4;5}(u_3^2+v_3^2)+a_{3,4;6}(u_4^2+v_4^2)+a_{3,4;7}[(u_3u_4+v_3v_4)\cos(\gamma_2)-(u_4v_3-u_3v_4)\sin(\gamma_2)]
\end{aligned}
$$

In the coefficients $a_{i,k;l}$, i and k indicate the involved Galilean satellites and l is the number of the coefficient. The coefficients with $l = 1, 8, 9$ are not constant, but we consider their dependence on the variables L_i.

(4) Mutual perturbation satellites (third order)

$$
\begin{aligned}
\mathcal{H}_{mut3} &= a3_{1,2;1}(x_1^2+y_1^2)x_1+a3_{1,2;2}(x_2^2+y_2^2)x_1+a3_{1,2;3}(u_1^2+v_1^2)x_1+a3_{1,2;4}(u_2^2+v_2^2)x_1\\
&+ a3_{1,2;5}(x_1^2+y_1^2)x_2+a3_{1,2;6}(x_2^2+y_2^2)x_2+a3_{1,2;7}(u_1^2+v_1^2)x_2+a3_{1,2;8}(u_2^2+v_2^2)x_2\\
&+ b_{1,2;1}(x_1^3-3x_1y_1^2)+b_{1,2;2}[(x_1^2-y_1^2)x_2-2x_1y_1y_2]\\
&+ b_{1,2;3}[(x_2^2-y_2^2)x_1-2x_2y_2y_1]+b_{1,2;4}(x_2^3-3x_2y_2^2)\\
&+ b_{1,2;5}[(u_1^2-v_1^2)x_1-2u_1v_1y_1]+b_{1,2;6}[(u_1^2-v_1^2)x_2-2u_1v_1y_2]\\
&+ b_{1,2;7}[(u_1u_2-v_1v_2)x_1-(v_1u_2+u_1v_2)y_1]+b_{1,2;8}[(u_1u_2-v_1v_2)x_2-(v_1u_2+u_1v_2)y_2]\\
&+ b_{1,2;9}[(u_2^2-v_2^2)x_1-2u_2v_2y_1]+b_{1,2;10}[(u_2^2-v_2^2)x_2-2u_2v_2y_2]\\
&+ b_{1,2;11}[(x_1^2-y_1^2)x_2+2x_1y_1y_2]+b_{1,2;12}[(x_2^2-y_2^2)x_1+2x_2y_2y_1]\\
&+ b_{1,2;13}[(u_1^2-v_1^2)x_1+2u_1v_1y_1]+b_{1,2;14}[(u_1^2-v_1^2)x_2+2u_1v_1y_2]\\
&+ b_{1,2;15}[(x_1u_2-y_1v_2)u_1+(y_1u_2+x_1v_2)v_1]+b_{1,2;16}[(x_1u_1-y_1v_1)u_2+(y_1u_1+x_1v_1)v_2]\\
&+ b_{1,2;17}[(u_1u_2-v_1v_2)x_1+(v_1u_2+u_1v_2)y_1]+b_{1,2;18}[(x_2u_2-y_2v_2)u_1+(y_2u_2+x_2v_2)v_1]\\
&+ b_{1,2;19}[(x_2u_1-y_2v_1)u_2+(y_2u_1+x_2v_1)v_2]\\
&+ b_{1,2;20}[(u_1u_2-v_1v_2)x_2+(v_1u_2+u_1v_2)y_2]+b_{1,2;21}[(u_2^2-v_2^2)x_1+2u_2v_2y_1]\\
&+ b_{1,2;22}[(u_2^2-v_2^2)x_2+2u_2v_2y_2]\\
&+ a3_{2,3;1}(x_1^2+y_1^2)[x_2\cos(\gamma_1)-y_2\sin(\gamma_1)]+a3_{2,3;2}(x_2^2+y_2^2)[x_2\cos(\gamma_1)-y_2\sin(\gamma_1)]\\
&+ a3_{2,3;3}(u_1^2+v_1^2)[x_2\cos(\gamma_1)-y_2\sin(\gamma_1)]+a3_{2,3;4}(u_2^2+v_2^2)[x_2\cos(\gamma_1)-y_2\sin(\gamma_1)]\\
&+ a3_{2,3;5}(x_1^2+y_1^2)x_3+a3_{2,3;6}(x_2^2+y_2^2)x_3+a3_{2,3;7}(u_1^2+v_1^2)x_3+a3_{2,3;8}(u_2^2+v_2^2)x_3\\
&+ b_{2,3;1}[(x_2^3-3x_2y_2^2)\cos(3\gamma_1)-(3x_2^2y_2-y_2^3)\sin(3\gamma_1)]\\
&+ b_{2,3;2}[((x_2^2-y_2^2)x_3-2x_2y_2y_3)\cos(2\gamma_1)-(2x_2y_2x_3+(x_2^2-y_2^2)y_3)\sin(2\gamma_1)]\\
&+ b_{2,3;3}[((x_3^2-y_3^2)x_2-2x_3y_3y_2)\cos(\gamma_1)-(2x_3y_3x_2+(x_3^2-y_3^2)y_2)\sin(\gamma_1)]+b_{2,3;4}(x_3^3-3x_3y_3^2)\\
&+ b_{2,3;5}[((u_2^2-v_2^2)x_2-2u_2v_2y_2)\cos(3\gamma_1)-(2u_2v_2x_2+(u_2^2-v_2^2)y_2)\sin(3\gamma_1)]\\
&+ b_{2,3;6}[((u_2^2-v_2^2)x_3-2u_2v_2y_3)\cos(2\gamma_1)-(2u_2v_2x_3+(u_2^2-v_2^2)y_3)\sin(2\gamma_1)]\\
&+ b_{2,3;7}[((x_2u_2-y_2v_2)u_3-(y_2u_2+x_2v_2)v_3)\cos(2\gamma_1)-((y_2u_2+x_2v_2)u_3+(x_2u_2-y_2v_2)v_3)\sin(2\gamma_1)]\\
&+ b_{2,3;8}[((x_3u_2-y_3v_2)u_3-(y_3u_2+x_3v_2)v_3)\cos(2\gamma_1)-((y_3u_2+x_3v_2)u_3+(x_3u_2-y_3v_2)v_3)\sin(2\gamma_1)]\\
&+ b_{2,3;9}[((u_3^2-v_3^2)x_2-2u_3v_3y_2)\cos(\gamma_1)-(2u_3v_3x_2+(u_3^2-v_3^2)y_2)\sin(\gamma_1)]\\
&+ b_{2,3;10}[(u_3^2-v_3^2)x_3-2u_3v_3y_3]\\
&+ b_{2,3;11}[((x_2^2-y_2^2)x_3+2x_2y_2y_3)\cos(2\gamma_1)-(2x_2y_2x_3-(x_2^2-y_2^2)y_3)\sin(2\gamma_1)]
\end{aligned}
$$

$$
\begin{aligned}
&+ b_{2,3;12}[((x_3^2-y_3^2)x_2+2x_3y_3y_2)\cos(\gamma_1)-(2x_3y_3x_2-(x_3^2-y_3^2)y_2)\sin(\gamma_1)]\\
&+ b_{2,3;13}[((u_2^2-v_2^2)x_2+2u_2v_2y_2)\cos(\gamma_1)-(2u_2v_2x_2-(u_2^2-v_2^2)y_2)\sin(\gamma_1)]\\
&+ b_{2,3;14}[((u_2^2-v_2^2)x_3+2u_2v_2y_3)\cos(2\gamma_1)-(2u_2v_2x_3-(u_2^2-v_2^2)y_3)\sin(2\gamma_1)]\\
&+ b_{2,3;15}[(x_2u_3-y_2v_3)u_2+(y_2u_3+x_2v_3)v_2]\\
&+ b_{2,3;16}[((x_2u_2-y_2v_2)u_3+(y_2u_2+x_2v_2)v_3)\cos(2\gamma_1)-((y_2u_2+x_2v_2)u_3-(x_2u_2-y_2v_2)v_3)\sin(2\gamma_1)]\\
&+ b_{2,3;17}[(u_2u_3-v_2v_3)x_2-(v_2u_3+u_2v_3)y_2]\\
&+ b_{2,3;18}[((x_3u_3-y_3v_3)u_2+(y_3u_3+x_3v_3)v_2)\cos(\gamma_1)+((y_3u_3+x_3v_3)u_2-(x_3u_3-y_3v_3)v_2)\sin(\gamma_1)]\\
&+ b_{2,3;19}[((x_3u_2-y_3v_2)u_3+(y_3u_2+x_3v_2)v_3)\cos(\gamma_1)-((y_3u_2+x_3v_2)u_3-(x_3u_2-y_3v_2)v_3)\sin(\gamma_1)]\\
&+ b_{2,3;20}[((u_3u_2-v_3v_2)x_3+(v_3u_2+u_3v_2)y_3)\cos(\gamma_1)-((v_3u_2+u_3v_2)x_3-(u_3u_2-v_3v_2)y_3)\sin(\gamma_1)]\\
&+ b_{2,3;21}[((u_3^2-v_3^2)x_2+2u_3v_3y_2)\cos(\gamma_1)+(2u_3v_3x_2-(u_3^2-v_3^2)y_2)\sin(\gamma_1)]\\
&+ b_{2,3;22}[(u_3^2-v_3^2)x_3+2u_3v_3y_3]\\
&+ b_{1,3;1}[(x_1^3-3x_1y_1^2)\cos(2\gamma_1)-(3x_1^2y_1-y_1^3)\sin(2\gamma_1)]\\
&+ b_{1,3;2}[((x_1^2-y_1^2)x_3-2x_1y_1y_3)\cos(\gamma_1)-(2x_1y_1x_3+(x_1^2-y_1^2)y_3)\sin(\gamma_1)]\\
&+ b_{1,3;3}[(x_3^2-y_3^2)x_1-2x_3y_3y_1]+b_{1,3;4}[(x_3^3-3x_3y_3^2)\cos(\gamma_1)+(3x_3y_3^2-y_3^3)\sin(\gamma_1)]\\
&+ b_{1,3;5}[((u_1^2-v_1^2)x_1-2u_1v_1y_1)\cos(2\gamma_1)-(2u_1v_1x_1+(u_1^2-v_1^2)y_1)\sin(2\gamma_1)]\\
&+ b_{1,3;6}[((u_1^2-v_1^2)x_3-2u_1v_1y_3)\cos(\gamma_1)-(2u_1v_1x_3+(u_1^2-v_1^2)y_3)\sin(\gamma_1)]\\
&+ b_{1,3;7}[((x_1u_1-y_1v_1)u_3-(y_1u_1+x_1v_1)v_3)\cos(\gamma_1)-((y_1u_1+x_1v_1)u_3+(x_1u_1-y_1v_1)v_3)\sin(\gamma_1)]\\
&+ b_{1,3;8}[(x_3u_3-y_3v_3)u_1-(y_3u_3+x_3v_3)v_1]+b_{1,3;9}[(u_3^2-v_3^2)x_1-2u_3v_3y_1]\\
&+ b_{1,3;10}[((u_3^2-v_3^2)x_3-2u_3v_3y_3)\cos(\gamma_1)+(2u_3v_3x_3+(u_3^2-v_3^2)y_3)\sin(\gamma1)];
\end{aligned}
$$

In the coefficients $a3_{i,k;l}$ and $b_{i,k;l}$, i and k indicate the involved Galilean satellites and l is the number of the coefficient.

(5) Sun's perturbation

$$
\begin{aligned}
&\mathcal{H}_{sun}=s_{1;1}(L_1/L_s)\\
&+ s_{1;2}(x_1^2+y_1^2)+s_{1;3}[(x_1k_s-y_1h_s)\cos(\gamma_1+\gamma_2)-(k_sy_1+x_1h_s)\sin(\gamma_1+\gamma_2)]\\
&+ s_{1;4}(u_1^2+v_1^2)+s_{1;5}[(u_1q_s-v_1p_s)\cos(\gamma_1+\gamma_2)-(q_sv_1+u_1p_s)\sin(\gamma_1+\gamma_2)]\\
&+ s_{1;6}[\cos(\lambda_s+\gamma_1+\gamma_2)x_1-\sin(\lambda_s+\gamma_1+\gamma_2)y_1]\\
&+ s_{1;7}[\cos(2\lambda_s+2\gamma_1+2\gamma_2)(x_1^2-y_1^2)-\sin(2\lambda_s+2\gamma_1+2\gamma_2)(2x_1y_1)]\\
&+ s_{1;8}[\cos(2\lambda_s+\gamma_1+\gamma_2)(k_sx_1+h_sy_1)-\sin(2\lambda_s+\gamma_1+\gamma_2)(k_sy_1-x_1h_s)]\\
&+ s_{1;9}[\cos(2\lambda_s+2\gamma_1+2\gamma_2)(u_1^2-v_1^2)-\sin(2\lambda_s+2\gamma_1+2\gamma_2)(2u_1v_1)]\\
&+ s_{1;10}[\cos(2\lambda_s+\gamma_1+\gamma_2)(q_su_1+p_sv_1)-\sin(2\lambda_s+\gamma_1+\gamma_2)(q_sv_1-u_1p_s)]\\
&+ s_{2;1}(L_2/L_s)\\
&+ s_{2;2}(x_2^2+y_2^2)+s_{2;3}[(x_2k_s-y_2h_s)\cos(\gamma_1+\gamma_2)-(k_sy_2+x_2h_s)\sin(\gamma_1+\gamma_2)]\\
&+ s_{2;4}(u_2^2+v_2^2)+s_{2;5}[(u_2q_s-v_2p_s)\cos(\gamma_1+\gamma_2)-(q_sv_2+u_2p_s)\sin(\gamma_1+\gamma_2)]\\
&+ s_{2;6}[\cos(\lambda_s+\gamma_1+\gamma_2)x_2-\sin(\lambda_s+\gamma_1+\gamma_2)y_2]\\
&+ s_{2;7}[\cos(2\lambda_s+2\gamma_1+2\gamma_2)(x_2^2-y_2^2)-\sin(2\lambda_s+2\gamma_1+2\gamma_2)(2x_2y_2)]\\
&+ s_{2;8}[\cos(2\lambda_s+\gamma_1+\gamma_2)(k_sx_2+h_sy_2)-\sin(2\lambda_s+\gamma_1+\gamma_2)(k_sy_2-x_2h_s)]\\
&+ s_{2;9}[\cos(2\lambda_s+2\gamma_1+2\gamma_2)(u_2^2-v_2^2)-\sin(2\lambda_s+2\gamma_1+2\gamma_2)(2u_2v_2)]\\
&+ s_{2;10}[\cos(2\lambda_s+\gamma_1+\gamma_2)(q_su_2+p_sv_2)-\sin(2\lambda_s+\gamma_1+\gamma_2)(q_sv_2-u_2p_s)]\\
&+ s_{3;1}(L_3/L_s)\\
&+ s_{3;2}(x_3^2+y_3^2)+s_{3;3}[(x_3k_s-y_3h_s)\cos(\gamma_2)-(k_sy_3+x_3h_s)\sin(\gamma_2)]\\
&+ s_{3;4}(u_3^2+v_3^2)+s_{3;5}[(u_3q_s-v_3p_s)\cos(\gamma_2)-(q_sv_3+u_3p_s)\sin(\gamma_2)]\\
&+ s_{3;6}(\cos(\lambda_s+\gamma_2)x_3-\sin(\lambda_s+\gamma_2)y_3)\\
&+ s_{3;7}[\cos(2\lambda_s+2\gamma_2)(x_3^2-y_3^2)-\sin(2\lambda_s+2\gamma_2)(2x_3y_3)]\\
&+ s_{3;8}[\cos(2\lambda_s+\gamma_2)(k_sx_3+h_sy_3)-\sin(2\lambda_s+\gamma_2)(k_sy_3-x_3h_s)]\\
&+ s_{3;9}[\cos(2\lambda_s+2\gamma_2)(u_3^2-v_3^2)-\sin(2\lambda_s+2\gamma_2)(2u_3v_3)]\\
&+ s_{3;10}[\cos(2\lambda_s+\gamma_2)(q_su_3+p_sv_3)-\sin(2\lambda_s+\gamma_2)(q_sv_3-u_3p_s)]\\
&+ s_{4;2}(x_4^2+y_4^2)+s_{4;3}(x_4k_s-y_4h_s)\\
&+ s_{4;4}(u_4^2+v_4^2)+s_{4;5}(u_4q_s-v_4p_s)
\end{aligned}
$$

$$
\begin{aligned}
&+ s_{4;6}[\cos(\lambda_s)x_4 - \sin(\lambda_s)y_4] \\
&+ s_{4;7}[\cos(2\lambda_s)(x_4^2 - y_4^2) - \sin(2\lambda_s)(2x_4y_4)] \\
&+ s_{4;8}[\cos(2\lambda_s)(k_s x_4 + h_s y_4) - \sin(2\lambda_s)(k_s y_4 - x_4 h_s)] \\
&+ s_{4;9}[\cos(2\lambda_s)(u_4^2 - v_4^2) - \sin(2\lambda_s)(2u_4v_4)] \\
&+ s_{4;10}[\cos(2\lambda_s)(q_s u_4 + p_s v_4) - \sin(2\lambda_s)(q_s v_4 - u_4 p_s)]
\end{aligned}
$$

In the coefficients $s_{i;l}$, i indicates the involved Galilean satellite and l is the number of the coefficient. The other parameters are the mean longitude of the Sun λ_s and its equinoctial elements $h_s = e_s\cos(\varpi_s)$, $k_s = e_s\sin(\varpi_s)$, $q_s = s_s\cos(\Omega_s)$ and $p_s = s_s\sin(\Omega_s)$. The coefficients with $l = 1$ are not constant, but we consider their dependence on the variables L_i.

The list of the coefficients is

$$
\begin{aligned}
\mu_{ik} &= -Gm_i m_k/a_k \\
j_{i;1} &= -(1/2)\mu_i^4\beta_i^7 R_0^2 J_2 & j_{i;2} &= -(3/4)\mu_i^2\beta_i^3(R_0/a_i)^2 J_2/L_i^3 \\
j_{i;3} &= (3/8)\mu_i^7\beta_i^{11} R_0^4 J_4 & j_{i;4} &= (15/8)\mu_i^2\beta_i^3(R_0/a_i)^4 J_4/L_i^3 \\
a_{i,k;1} &= \mu_{ik} c_{(0,0,0,0,0,0)} & a_{i,k;2} &= \mu_{ik} c^1_{(0,0,0,0,0,0)}/L_i \\
a_{i,k;3} &= \mu_{ik} c^1_{(0,0,0,0,0,0)}/L_k & a_{i,k;4} &= \mu_{ik} c_{(0,0,-1,1,0,0)}/\sqrt{L_i L_k} \\
a_{i,k;5} &= \mu_{ik} c^2_{(0,0,0,0,0,0)}/(4L_i) & a_{i,k;6} &= \mu_{ik} c^2_{(0,0,0,0,0,0)}/(4L_k) \\
a_{i,k;7} &= \mu_{ik} c_{(0,0,0,0,-1,1)}/(4\sqrt{L_i L_k}) & a_{i,k;8} &= \mu_{ik} c_{(-1,2,-1,0,0,0)} \\
a_{i,k;9} &= \mu_{ik} c_{(-1,2,0,-1,0,0)} & a_{i,k;10} &= \mu_{ik} c_{(-2,4,-2,0,0,0)}/L_i \\
a_{i,k;11} &= \mu_{ik} c_{(-2,4,0,-2,0,0)}/L_k & a_{i,k;12} &= \mu_{ik} c_{(-2,4,-1,-1,0,0)}/\sqrt{L_i L_k} \\
a_{i,k;13} &= \mu_{ik} c_{(-2,4,0,0,-2,0)}/(4L_i) & a_{i,k;14} &= \mu_{ik} c_{(-2,4,0,0,0,-2)}/(4L_k) \\
a_{i,k;15} &= \mu_{ik} c_{(-2,4,0,0,-1,-1)}/(4\sqrt{L_i L_k}) \\
a3_{i,k;1} &= \mu_{ik} c^1_{(-1,2,-1,0,0,0)}/\sqrt{L_i^3} & a3_{i,k;2} &= \mu_{ik} c^2_{(-1,2,-1,0,0,0)}/(L_k\sqrt{L_i}) \\
a3_{i,k;3} &= \mu_{ik} c^3_{(-1,2,-1,0,0,0)}/(4\sqrt{L_i^3}) & a3_{i,k;4} &= \mu_{ik} c^3_{(-1,2,-1,0,0,0)}/(4L_k\sqrt{L_i}) \\
a3_{i,k;5} &= \mu_{ik} c^1_{(-1,2,0,-1,0,0)}/(L_i\sqrt{L_k}) & a3_{i,k;6} &= \mu_{ik} c^2_{(-1,2,0,-1,0,0)}/\sqrt{L_k^3} \\
a3_{i,k;7} &= \mu_{ik} c^3_{(-1,2,0,-1,0,0)}/(4L_i\sqrt{L_k}) & a3_{i,k;8} &= \mu_{ik} c^3_{(-1,2,0,-1,0,0)}/(4\sqrt{L_k^3}) \\
b_{i,k;1} &= \mu_{ik} c_{(3-j,j,-3,0,0,0)}/\sqrt{L_i^3} & b_{i,k;2} &= \mu_{ik} c_{(3-j,j,-2,-1,0,0)}/(L_i\sqrt{L_k}) \\
b_{i,k;3} &= \mu_{ik} c_{(3-j,j,-1,-2,0,0)}/(L_k\sqrt{L_i}) & b_{i,k;4} &= \mu_{ik} c_{(3-j,j,0,-3,0,0)}/\sqrt{L_k^3} \\
b_{i,k;5} &= \mu_{ik} c_{(3-j,j,-1,0,-2,0)}/(4\sqrt{L_i^3}) & b_{i,k;6} &= \mu_{ik} c_{(3-j,j,-1,0,0,-2)}/(4L_i\sqrt{L_k}) \\
b_{i,k;7} &= \mu_{ik} c_{(3-j,j,-1,0,-1,-1)}/(4L_i\sqrt{L_k}) & b_{i,k;8} &= \mu_{ik} c_{(3-j,j,0,-1,-1,-1)}/(4L_k\sqrt{L_i}) \\
b_{i,k;9} &= \mu_{ik} c_{(3-j,j,0,-1,-2,0)}/(4L_i\sqrt{L_k}) & b_{i,k;10} &= \mu_{ik} c_{(3-j,j,0,-1,0,-2)}/(4\sqrt{L_k^3}) \\
b_{i,k;11} &= \mu_{ik} c_{(-1,2,-2,1,0,0)}/(L_i\sqrt{L_k}) & b_{i,k;12} &= \mu_{ik} c_{(-1,2,1,-2,0,0)}(L_k\sqrt{L_i}) \\
b_{i,k;13} &= \mu_{ik} c_{(-1,2,1,0,-2,0)}/(4\sqrt{L_i^3}) & b_{i,k;14} &= \mu_{ik} c_{(-1,2,0,1,-2,0)}/(4L_i\sqrt{L_k}) \\
b_{i,k;15} &= \mu_{ik} c_{(-1,2,-1,0,1,-1)}/(4L_i\sqrt{L_k}) & b_{i,k;16} &= \mu_{ik} c_{(-1,2,-1,0,-1,1)}/(4L_i\sqrt{L_k}) \\
b_{i,k;17} &= \mu_{ik} c_{(-1,2,1,0,-1,-1)}/(4L_i\sqrt{L_k}) & b_{i,k;18} &= \mu_{ik} c_{(-1,2,0,-1,1,-1)}/(4L_k\sqrt{L_i}) \\
b_{i,k;19} &= \mu_{ik} c_{(-1,2,0,-1,-1,1)}/(4L_k\sqrt{L_i}) & b_{i,k;20} &= \mu_{ik} c_{(-1,2,0,1,-1,-1)}/(4L_k\sqrt{L_i}) \\
b_{i,k;21} &= \mu_{ik} c_{(-1,2,1,0,0,-2)}/(4L_k\sqrt{L_i}) & b_{i,k;22} &= \mu_{ik} c_{(-1,2,1,0,0,-2)}/(4\sqrt{L_k^3}) \\
s_{i;1} &= \mu_{is} c^1_{(0,0,0,0,0,0)}/L_i & s_{i;2} &= \mu_{is} c_{(0,0,-1,1,0,0)}/\sqrt{L_i} \\
s_{i;3} &= \mu_{is} c^2_{(0,0,0,0,0,0)}/(4L_i) & s_{i;4} &= \mu_{is} c_{(0,0,0,0,-1,1)}/(2\sqrt{L_i}) \\
s_{i;5} &= \mu_{is} c_{(0,1,-1,0,0,0)}/\sqrt{L_i} & s_{i;6} &= \mu_{is} c_{(0,2,-2,0,0,0)}/L_i \\
s_{i;7} &= \mu_{is} c_{(0,2,-1,-1,0,0)}/\sqrt{L_i} & s_{i;8} &= \mu_{is} c_{(0,2,0,0,-2,0)}/(4L_i) \\
s_{i;9} &= \mu_{is} c_{(0,2,0,0,-1,-1)}/(2\sqrt{L_i})
\end{aligned}
$$

In the case of the couples Io-Europa and Europa-Ganymede, in the coefficients $b_{i,k;l}$, with $l = 1, 10$, j is equal to 6, while for Io-Ganymede, j is equal to 4.

B ROTATION MODELS

As we introduced in Chapter 6, if we want to compute the acceleration due to the gravitational field's anomalies, we need a model for the rotation of the extended bodies. In fact, the harmonic expansion is defined in a body-fixed reference frame and we have to perform a change of coordinates that follows the rotation to use it.

The rotation of the bodies is assumed around an axis defined by two angles α_R and δ_R (see Figure B.1). In order to pass to a reference frame that rotates with the body, first we need to bring the z axis along the spin axis. This is performed through two rotations as shown in the figure: the first one of $90° + \alpha_R$ around z and the other one of $90° - \delta_R$ around the new axis x'.

At this point we just need to rotate the system in order to have the zero meridian on the x positive axis. This meridian is defined at a conventional time t_0 (for example J2000). If the angular velocity ω is constant, the angle of the zero meridian at a certain time t is simply

$$\phi = \phi_0 + \omega(t - t_0).$$

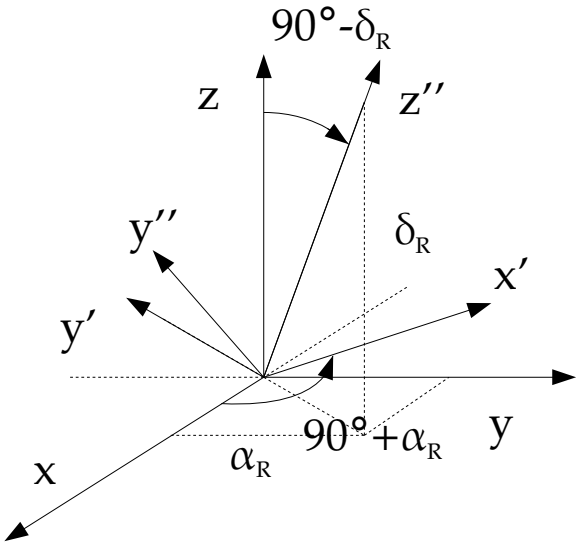

Figure B.1.: *The rotation axis z'' and the angles α_R and δ_R.*

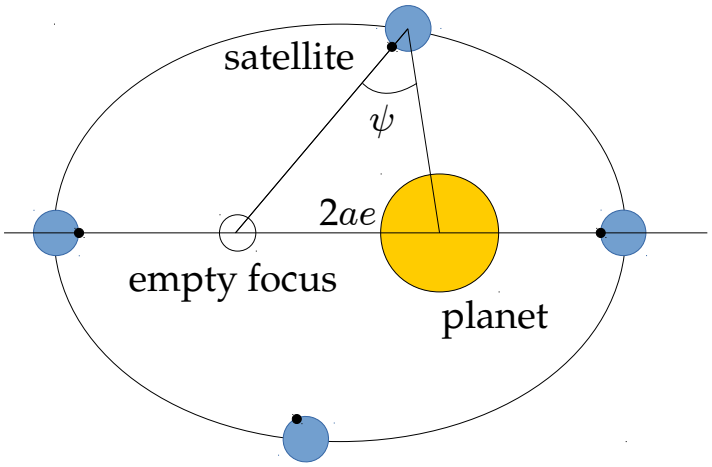

Figure B.2.: *Example of satellite in synchronous resonance; the body looks at the empty focus, defining an angle* ψ *with the conjunction satellite-planet.*

Therefore we have to perform a rotation of ϕ around the new z axis if we want the body-fixed reference frame at the time t.

We consider also secular precession and nutation effects on the axis. Actually, we do not develop a model of the rotation, but we implement directly the rotation models presented in [2].

They are defined by the formulas

$$\begin{aligned}
\alpha_R &= \alpha_0 + p_\alpha T + a_\alpha \sin(J_a) + b_\alpha \sin(J_b) + c_\alpha \sin(J_c) + d_\alpha \sin(J_d) + e_\alpha \sin(J_e), \\
\delta_R &= \delta_0 + p_\delta T + a_\delta \cos(J_a) + b_\delta \cos(J_b) + c_\delta \cos(J_c) + d_\delta \cos(J_d) + e_\delta \cos(J_e), \\
\phi &= \phi_0 + \omega d
\end{aligned} \tag{B.1}$$

where α_0 and δ_0 are the constant values of the angles, p_α and p_δ are the secular precession terms and T is the time after J2000 in centuries, ϕ_0 is the zero meridian at J2000, ω is the spin angular velocity and d the time after J2000 in days. All the other parameters describe librational movements.

In Table B.1 we reported the values of the various parameters involved in (B.1). The effect of precession and nutation are very small, but it is important to consider them in order to be aligned to the models implemented for the design of the JUICE mission.

B.1 SYNCHRONOUS RESONANCE

For the Galilean satellites we do not assume a constant angular velocity, but we model the rotation in order to have a perfect synchronous rotation of the moons. As described in Chapter 4 and shown in Figure B.2, a satellite in synchronous resonance looks, as a first approximation, at the empty focus of its orbit.

Parameter	Jupiter	Io	Europa	Ganymede	Callisto
α_0 (°)	268.056595	268.050	268.080	268.200	268.720
δ_0 (°)	64.495303	64.500	64.510	64.570	64.830
ϕ_0 (°)	284.950000	200.390	36.022	44.064	259.510
ω (°/day)	870.536000	202.489	101.375	50.318	21.571
p_a (°/day)	-0.006499	-0.009	-0.009	-0.009	-0.009
p_d (°/day)	0.002413	0.003	0.003	0.003	0.003

Table B.1.: Values for the rotational models of Jupiter and Galilean satellites. These numbers are taken from [2], which is the official report of the IAU Working Group on Cartographic Coordinates and Rotational Elements and it contains rotational parameters for planets and satellites.

We define the first meridian as the meridian aligned with the empty focus. If we denote with λ_J the longitude of Jupiter in the body-fixed reference frame of the satellite, we have that

$$\phi = \lambda_J + \psi, \tag{B.2}$$

where ψ is the offset angle from the focus occupied by Jupiter and the empty one. As it is clear from Figure B.2, ψ depends on the eccentricity of the orbit and on the position of the satellite. In particular,

$$\psi = -2e \sin(\ell),$$

where e is the eccentricity of the moon and ℓ its mean anomaly.

For a more sophisticated model we can add a libration to the right hand side of (B.2), as done in [7] considering a geometric libration angle. This is particularly important in the case we want to investigate the rotation properties of the moons.

BIBLIOGRAPHY

[1] Alessi E.M., Cicalò S., Milani A., Tommei G. (2012) *Desaturation manoeuvres and precise orbit determination for the BepiColombo mission*. MNRAS 423, 2270-2278.

[2] Archinal B.A. et al. (2011) *Report of the IAU Working Group on Cartographic Coordinates and Rotational Elements: 2009*. Celestial Mechanics and Dynamical Astronomy 109, 101-135.

[3] Carpino M., Milani A., Nobili A.M. (1987) *Long-term numerical integrations and synthetic theories for the motion of the outer planets*. Astronomy and Astrophysics 181, 182-194.

[4] Cassen P., Reynolds R.T., Peale S.J. (1979) *Is there liquid water on Europa?*. Geophysical Research Letters vol.6 n.9, 731-734.

[5] Celletti A., Paita F., Pucacco G. (2018) *The dynamics of the de Sitter resonance*. Celestial Mechanics and Dynamical Astronomy 130, 15.

[6] De Sitter W. (1909) *On the periodic solutions of a special case of the problem of four bodies*. Proceedings of Royal Netherlands Academy of Arts and Science 11, 682-698.

[7] Dirkx D., Lainey V., Gurvits L.I., Visser P.N.A.M. (2016) *Dynamical modelling of the Galilean moons for the JUICE mission*. Planetary and Space Science 134, 82-95

[8] Dirkx D., Gurvits L.I., Lainey V., Lari G., Milani A., Cimó G., Bocanegra-Bahamon T.M., Visser P.N.A.M. (2017) *On the contribution of PRIDE-JUICE to Jovian system ephemerides*. Planetary and Space Science 147, 14-27.

[9] Efroimsky M., Lainey V. (2007) *The physics of Bodily Tides in Terrestrial Planets and the Appropriate Scales of Dynamical Evolution*. Journal of Geophysical Research 120.

[10] Ferraz-Mello S., Micchtchenko T.A., Beauge C. (2006) *Regular motions in extrasolar planetary systems. in Chaotic Worlds: From Order to Disorder in Gravitational N-body Dynamical Systems*. Steves B.A., Maciejewski A.J., Hendry M. (eds), 255-288, Springer.

[11] Fuller J., Luan J., Quataert E. (2016) *Resonance locking as the source of rapid tidal migration in the Jupiter ans Saturn moon systems*. MNRAS 458, 3867-3879.

[12] Galilei G. (1610) *Sidereus Nuncius*.

[13] Guenel M., Mathis S., Remus F. (2014) *Unravelling tidal dissipation in gaseous giant planets*. Astronomy and Astrophysics 566, L9.

[14] Iess L. et al. (2018) *Measurement of Jupiter's asymmetric gravity field*. Nature 555, 220–222

[15] Jacobson R.A. (2002) *Pioneer and Voyager. Jupiter encounter orbit reconstruction in the ICRF System*. AAS/AIAA, Space Flight Mechanics Meeting, 02-157.

[16] Jacobson R.A. (2015) *Gravity and tide parameters determined from satellites and spacecraft orbits*. American Astronomical Society, DDA Meeting 46.

[17] JUICE Science Study Team (2014) *JUICE: exploring the emergence of habitable worlds around gas giants*. ESA/SRE(2014) 1.

[18] *JUICE Repository*: `ftp://spiftp.esac.esa.int/data/SPICE/JUICE/kernels`

[19] Kaula W.M. (1964) *Tidal dissipation by solid friction and the resulting orbital evolution*. Reviews of Geophysics 2, 661-685.

[20] Lainey V., Vienne A., Duriez L. (2001) *New estimation of usually neglected forces acting on Galilean system*. Celestial Mechanics and Dynamical Astronomy 81, 115–122

[21] Lainey V., Duriez L., Vienne A. (2004) *New accurate ephemerides for the Galilean satellites of Jupiter I: numerical integration of elaborated equations of motion*. Astronomy & Astrophysics 420, 1171-1183.

[22] Lainey V., Duriez L., Vienne A. (2004) *Synthetic representation of the Galilean satellites' orbital motions from L1 ephemerides*. Astronomy & Astrophysics 456, 783-788.

[23] Lainey V., Dehant V., Pätzold M. (2007) *First numerical ephemerides of the Martian moons*. Astronomy and Astrophysics 465, 1075-1084.

[24] Lainey V., Arlot J.E., Karatekin O., Van Hoolst T. (2009) *Strong tidal dissipation in Io and Jupiter from astrometric observations*. Nature 459, 957-959.

[25] Lainey V. et al. (2017) *New constraints on Saturn's interior from Cassini astrometric data*. Icarus 281, 286-296.

[26] Laplace L.P. (1798) *Traité de Mécanique Céleste, Livre II*.

[27] Lari G. (2018) *A semi-analytical model of the Galilean satellites' dynamics*. Celestial Mechanics and Dynamical Astronomy, 130:50.

[28] Malhotra R. (1991) *Tidal origin of the Laplace resonance and the resurfacing of Ganymede*. Icarus 94, 399–412.

[29] Mignard F. (1979) *The evolution of the lunar orbit revisited I*. Earth, Moon and Planets 20, 301-315.

[30] Milani A., Nobili A.M. (1987) *Integration error over very long time spans*. Celestial Mechanics 43, 1-34.

[31] Milani A., Knežević Z. (1990) *Secular perturbation theory and computation of asteroid proper elements*. Celestial Mechanics and Dynamical Astronomy 49, 347-411.

[32] Milani A., Gronchi G.F. (2010) *Theory of orbit determination*. Cambridge University Press.

[33] Morbidelli A. (2002) *Modern Celestial Mechanics: Aspects of Solar system Dynamics*. Taylor and Francis, London.

[34] Murray C.D., Dermott S.F. (1999) *Solar System Dynamics*. Cambridge University Press.

[35] Musotto S., Varadi F., Moore W., Schubert G. Numerical simulations of the orbits of the Galilean Satellites. Icarus 159, 500-504 (2002)

[36] Nesvorny D., Ferraz-Mello S., Holman M., Morbidelli A. (2002) *Regular and chaotic dynamics in the mean-motion resonances: implications for the structure and the evolution of the asteroid belt*. Asteroids III, Bottke Jr. W.F., Cellino A., Paolicchi P., Binzel R.P. eds., University of Arizona, Tucson.

[37] Parisi M., Iess L., Finocchiaro S. (2013) *Multi-arc and batch-sequential filters for the orbit determination of ESA's JUICE mission*. 23rd International Symposium on Space Flight Dynamics.

[38] Peale S.J., Cassen P., Reynolds R.T. (1979) *Melting of Io by tidal dissipation*. Science 203, 892-894.

[39] Saillenfest M., Fouchard M., Tommei G., Valsecchi G.B. (2016) *Long term dynamics beyond Neptune: secular models to study the regular motions*. Celestial Mechanics and Dynamical Astronomy 126, 369-403.

[40] Saillenfest M., Lari G. (2017) *The long-term evolution of known resonant trans-Neptunian objects*. Astronomy and Astrophysics 603, A79.

[41] Schubert G., Anderson J.D., Spohn T., McKinnon W.B. (2004) *Interior composition, structure and dynamics of the Galilean satellites*. Jupiter. The planet,

satellites and magnetosphere, Bagenal F., Dowling T.E., McKinnon W.B. eds., Cambridge University Press.

[42] Serra D., Spoto F., Milani A. (2018) *A multi-arc approach for chaotic orbit determination problems*. Celestial Mechanics and Dynamical Astronomy, 130:75.

[43] Showalter M.R., Hamilton D.P. (2015) *Resonant interactions and chaotic rotation of Pluto's small moons*. Nature 522, 45-49

[44] Showman A.P., Malhotra R. (1999) *The Galilean satellites*. Science 286, 77-84.

[45] Sinclair A.T. (1975) *The orbital resonance amongst the Galilean satellites of Jupiter*. Celestial Mechanics 12, 89-96.

[46] Spoto F., Milani A. (2016) *Shadowing Lemma and chaotic orbit determination*. Celestial Mechanics and Dynamical Astronomy 124, 295-309.

[47] Tajeddine R., Cooper N.J., Lainey V., Charnoz S., C.D. Murray (2013) *Astrometric reduction of Cassini ISS images of the Saturnian satellites Mimas and Enceladus*. Astronomy and Astrophysics 551, A129.

[48] Tommei G., Milani A., Vokrouhlicky D. (2009) *Light-time computations for the BepiColombo radioscience esperiment*. Celestial Mechanics & Dynamical Astronomy 107, 285-298

[49] Will C.M. (2006) *The Confrontation between General relativity and Experiment*. Living Reviews in Relativity 9, 3-100.

[50] Yoder C.F., Peale S.J. (1981) *The tides of Io*. Icarus 47, 1-35